2014

Transient Stability Enhancement of Wind Farms Using Power Electronics and FACTS Controllers

Hossein A. Mohammadpour
University of South Carolina - Columbia

TRANSIENT STABILITY ENHANCEMENT OF WIND FARMS USING POWER ELECTRONICS AND FACTS CONTROLLERS

by

Hossein Ali Mohammadpour

Bachelor of Science
Iran University of Science and Technology 2006

Master of Science
Iran University of Science and Technology 2009

Submitted in Partial Fulfillment of the Requirements

for the Degree of Doctor of Philosophy in

Electrical Engineering

College of Engineering and Computing

University of South Carolina

2014

Accepted by:

Enrico Santi, Major Professor

Roger Dougal, Committee Member

Charles Brice, Committee Member

Edward P. Gatzke, Committee Member

Lacy Ford, Vice Provost and Dean of Graduate Studies

DEDICATION

To my parents and my family.

ACKNOWLEDGMENTS

I would like to thank all of those who took time to help me. A special thanks goes to my advisor Dr. Enrico Santi who guided me along in my studies and research, supported me to attend a number of conferences and presentations, and helped me in the arduous process of completing this dissertation document. He has set an example of excellence as a researcher, mentor, instructor, and role model.

I also would like to thank Dr. Yong-June Shin who gave me the opportunity to study at the University of South Carolina and taught me how to research and present my research effectively. I would additionally like to thank Drs. Enrico Santi, Roger A. Dougal, Charles Brice, and Edward P. Gatzke for participating in my dissertation committee and mentoring me in the formative stages of my dissertation.

I would like to thank the members of the Power Electronics and Power IT groups in Department of Electrical Engineering at the University of South Carolina, including Amin Ghaderi, Soheila Eskandari, Qiu Deng, Cuong Nguyen, Paul Young, Ryan Lukens, Jonathan Siegres, Kang Peng, Ozan Gulbudak, Vinya Sri Pencnala, Silvia Arrua, and Drs. Philip Stone, Patrick Mitchell, Mohammed Hassan, Moinul Islam, and David Coats. Last, but not least, I would like to thank all of my family members and my friends in Columbia, who are like a family to me, especially Amin Ghaderi and Nima Mohammadi.

The projects that make up this dissertation document have been supported by the National Science Foundation Industry / University Cooperative Research Center on GRid-connected Advanced Power Electronics Systems (GRAPES).

ABSTRACT

Nowadays, it is well-understood that the burning of fossil fuels in electric power station has a significant influence on the global climate due to greenhouse gases. In many countries, the use of cost-effective and reliable low-carbon electricity energy sources is becoming an important energy policy. Among different kinds of clean energy resources- such as solar power, hydro-power, ocean wave power and so on, wind power is the fastest-growing form of renewable energy at the present time.

Moreover, adjustable speed generator wind turbines (ASGWT) has key advantages over the fixed-speed generator wind turbines (FSGWT) in terms of less mechanical stress, improved power quality, high system efficiency, and reduced acoustic noise. One important class of ASGWT is the doubly-fed induction generator (DFIG), which has gained a significant attention of the electric power industry due to their advantages over the other class of ASGWT, i.e. fully rated converter-based wind turbines. Because of increased integration of DFIG-based wind farms into electric power grids, it is necessary to transmit the generated power from wind farms to the existing grids via transmission networks without congestion.

Series capacitive compensation of DFIG-based wind farm is an economical way to increase the power transfer capability of the transmission line connecting wind farm to the grid. For example, a study performed by ABB reveals that increasing the power transfer capability of an existing transmission line from 1300 MW to 2000 MW using series compensation is 90% less than the cost of building a new transmission line.

However, a factor hindering the extensive use of series capacitive compensation is the potential risk of sub- synchronous resonance (SSR). The SSR is a condition where the wind

farm exchanges energy with the electric network, to which it is connected, at one or more natural frequencies of the electric or mechanical part of the combined system, comprising the wind farm and the network, and the frequency of the exchanged energy is below the fundamental frequency of the system. This phenomenon may cause severe damage in the wind farm, if not prevented.

Therefore, this dissertation deals with the SSR phenomena in a capacitive series compensated wind farm. A DFIG-based wind farm, which is connected to a series compensated transmission line, is considered as a case study. The small-signal stability analysis of the system is presented, and the eigenvalues of the system are obtained. Using both modal analysis and time-domain simulation, it is shown that the system is potentially unstable due to the SSR mode.

Then, three different possibilities for the addition of SSR damping controller (SSRDC) are investigated. The SSRDC can be added to (1) gate-controlled series capacitor (GCSC), (2) thyristor-controlled series capacitor (TCSC), or (3) DFIG rotor-side converter (RSC) and grid-side converter (GSC) controllers. The first and second cases are related to the series flexible AC transmission systems (FACTS) family, and the third case uses the DFIG back-to-back converters to damp the SSR. The SSRDC is designed using residue-based analysis and root locus diagrams. Using residue-based analysis, the optimal input control signal (ICS) to the SSRDC is identified that can damp the SSR mode without destabilizing other modes, and using root-locus analysis, the required gain for the SSRDC is determined. Moreover, two methods are discussed in order to estimate the optimum input signal to the SSRDC, without measuring it directly. In this dissertation, MATLAB/Simulink is used as a tool for modeling and design of the SSRDC, and PSCAD/EMTDC is used to perform time-domain simulation in order to verify the design process.

TABLE OF CONTENTS

LIST OF TABLES

LIST OF FIGURES

CHAPTER 1

INTRODUCTION

1.1 OVERVIEW AND LITERATURE REVIEW

Due to to the recent rapid penetration of wind power into the power systems [1] - [9], some countries in central Europe, e.g. Germany, have run out of suitable sites for onshore wind power projects, due to the high population density in these countries. Moreover, it has been found that the offshore wind power resources are much larger than onshore wind power sources [3]. Therefore, offshore wind farms have a great potential as large-scale sustainable electric energy resources [10], [11]. Recently, doubly-fed induction generator (DFIG) has gained significant attention of the electric power industry in offshore wind farms and renewable energy sources [1], [11] - [15].

However, in offshore wind farms, the distance between the wind turbines and the shore is much longer [15], [16] than that in onshore wind farms. Therefore, unlike the onshore wind farms - where the voltage level of the wind farm is usually the same as the voltage level of the distribution system - higher voltage levels with reliable and efficient transmission lines are required for the offshore wind farms to minimize the power losses [3], [10].

Currently, there are numerous large offshore wind farms operating throughout the world [3], [10], [17]. Future projects in offshore wind farms will be larger in size and further away from the shore [3]. This requires defining new concepts for the transmission system, including transmission lines from the offshore wind farm to the shore and network integration to the onshore power system. The transmission system options to transmit the wind power to the shore are high-voltage AC (HVAC) [3] or high-voltage DC (HVDC) [18] - [21]. The

comparison of these two options has already been studied in literature [22]. The HVAC solutions are viable for distances up to 250 km, and with series compensation, they may be viable for distances longer than 250 km. [3].

In the deregulated power market, it is necessary to increase the power transfer capability of existing transmission lines at the lowest cost [23]. Series compensation is considered to be a more economical solution to increase the power transfer capability of an existing transmission line compared to construction of new transmission lines [24] - [26] . Studies shows that in order to increase the transmittable power of an existing transmission line, the total cost of providing a capacitive series compensation to the transmission line is much less than the cost to build a new transmission line. As an example, a study performed by ABB reveals that increasing the power transfer capability of an existing transmission line from 1300 MW to 2000 MW using series compensation is 90% less than the cost of building a new transmission line [23].

However, a factor hindering the extensive use of series capacitive compensation is the potential risk of sub- synchronous resonance (SSR) [26] - [33], which may cause severe damage in the wind farm, if not prevented. The SSR in wind turbine generator systems is a condition where the wind farm exchanges energy with the electric network, to which it is connected, at one or more natural frequencies of the electric and mechanical part of the combined system, comprising the wind farm and the network. The frequency of the exchanged energy is below the fundamental frequency of the system. Three different types of SSR in DFIG wind farms have been identified in the literature [34] - [40]:

- Induction Generator Effect (SSIGE)
- Torsional Interactions (SSTI)
- Control Interactions (SSCI)

In case of the SSIGE, the magnitude of the equivalent rotor resistance at the sub-synchronous frequency can be negative, and if this negative resistance exceeds the sum of the resis-

tances of the armature and of the network, there will be an overall negative damping at the sub-synchronous frequency, and consequently the sub-synchronous current would increase with time [31], [34]. In SSTI, if the complement of the torsional natural frequency of the drive-train shaft system of the DFIG wind turbine happens to be close to the electric natural frequency of the electric network, the sub-synchronous torque components generated by the sub-synchronous induced armature voltage can be sustained [31], [34]. The nature of the SSCI is different from SSIGE and SSTI, since in this type of SSR, the DFIG wind turbine controllers play the main role in creating the SSCI; indeed, the SSCI may occur as a results of interaction between the series compensated electrical network and the DFIG wind turbine controllers [37] - [42].

Although the SSR analysis and damping in traditional power systems are well-known and have been extensively studied in the literature [26] - [29], [43] this problem in series-compensated wind farms requires more study and analysis. In particular, after the SSR event that occurred in the Electric Reliability Council of Texas (ERCOT) in 2009 [37] - [41], the wind power industry have become more interested in the SSR studies. In the ERCOT SSR event, a faulted line and subsequent outage in the network caused the radially connection of a large DFIG wind farm to the series compensation network, resulting in a fast generation of sub-synchronous frequency oscillation leaving some damages to both the series capacitor and the wind turbine [37] - [41].

Series FACTS devices have been studied in literature for SSR damping in fixed-speed wind turbine generator systems [44] - [47]. In [44] - [46], the authors have investigated the capability of the thyristor-controlled sereis capacitor (TCSC) in SSR damping in FSWTGS. In [47], the static synchronous series compensator (SSSC) has been used in a series compensated self-excited induction generator based wind farm for mitigating SSR and damping power system oscillations.

Moreover, the application of shunt FACTS devices in SSR damping has been studied in literature [46], [48] - [55]. In [48] - [52], a static synchronous compensator (STATCOM) is

presented to damp the SSR in a series compensated induction-generator (IG)-based wind farm. In [46], [53], [54], a static var compensator (SVC) has been employed in FSWTGS to mitigate the SSR. Moreover, reference [55] studies the SSR damping using co-ordination of super conducting magnetic energy storage (SMES) and STATCOM.

Some methods that have been employed in literature for SSRD controller design can be summarized as follows: Karaagac *et al.* [56] present a method for SSR damping in series compensated wind farm by introducing an auxiliary SSR damping controller (SSRDC) in the reactive power control loop of the DFIG controller and in the reactive power control loop of the high voltage DC (HVDC) onshore modular multi-level converter of offshore wind farms. In [56], both transmission line current and transmission line real power are used as input control signals (ICS) to the SSRDC block, and the SSRDC block is comprised of a multi-stage lead-lag compensator. Trial-and-error method using time-domain simulation is used to tune the multi-stage lead-lag compensator. Leon *et al.* [57] present a damping control method to mitigate sub-synchronous interactions (SSI) in DFIG wind farms. In that paper, the SSRDC is designed using a multi-input multi-output state-space method, and the ICSs to the SSRDC block are d-q axis currents of the DFIG stator and rotor windings.

Golshannavaz *et al.* [58] propose application of unified power flow controller (UPFC) for SSR damping in self-excited induction generator (SEIG) based wind farms. In that paper, two auxiliary SSRDCs are added to the UPFC controllers, one to the shunt inverter control system and the other to the series inverter control system. Only one signal, that is, rotor speed is used as ICS to the SSRDC. The SSRDCs are tuned using trial-and-error approach. El-Moursi *et al.* [50] and Golshannavaz *et al.* [49] present damping control algorithm for static synchronous compensator (STATCOM) to mitigate SSR in SEIG. In [50] and [49], the rotor speed is used as ICS to the SSRDC block.

Faried *et al.* [33] study SSR damping in nearby turbine generators by addition of a SSRDC to the controllers of the DFIG converters. For a steam turbine generator, located

close to a DFIG wind farm, with N multi-mass shaft sections, the SSRDC composed of N channels, and the ICS for the i^{th} channel is the rotor speed deviation of the i^{th} shaft section. In [33], the trial-and-error method is used to tune the SSRDC parameters in each channel. Leon *et al.* in [59] study SSR mitigation in nearby turbine generators by addition of a SSRDC to the converter controllers of a fully-rated fully rated converter wind turbines. In [59], a multi-input multi-output (MIMO) approach is used to design the SSR damping controller, and the inputs to the SSRDC block are the rotor speed deviations of different sections of the steam turbine.

1.2 Objectives and Outline

This dissertation aims to study SSR damping in DFIG wind farms using three different methods. The first method uses gate-controlled series capacitor (GCSC) for SSR damping. The GCSC, which consists of two anti-parallel GTOs connected in parallel with a fixed capacitor for each phase, is a FACTS device recently proposed for controlling the power flow in transmission lines [24], [60], [61]. In the GCSC, the gate-turn-off (GTO) or other gate commutated switches, e.g. gate commutated thyristor (GCT), are used to provide variable impedance for the transmission lines [24]. Unlike thyristors, which are not fully controllable switches, GTO's can be turned on and off, making them more controllable switches compared to thyristors [24]. In many situations where a controllable series compensator must be installed, the GCSC may be used instead of the TCSC, possibly with some advantages. A comparison of the sizing of the TCSC and the GCSC components, when both the GCSC and the TCSC have the same maximum capacitive impedance, shows that the power rating of the GCSC capacitor is smaller than that of the TCSC, especially for power-flow control applications. Moreover, the thyristor valve in the TCSC needs to have a higher current rating than the gate-commutated switch valve in the GCSC. Finally, the components of a GCSC designed for the same maximum compensation level of a TCSC may have switches with a smaller rating and, naturally, a reactor is not needed. For this

reason, unlike the TCSC, the GCSC is free of intrinsic internal resonance [60].

The second method uses thyristor controlled series capacitor (TCSC) for SSR damping. The TCSC, which consists of a thyristor-controlled reactor (TCR) in parallel with a fixed capacitor for each phase, is a later member of the first generation of FACTS devices [24]. This device enables the transmission companies to transfer more power on the existing transmission lines. For example, ABB manufactured the world's first TCSC, installed at Kayenta substation, Arizona in 1992. The TCSC increased the capacity of the transmission line by about 30%. By the end of year 2004, seven TCSCs have been installed worldwide [62]. TCSC introduces a number of important benefits in the application of series compensation like elimination of sub-synchronous resonance (SSR) risks, damping of active power oscillations, post-contingency stability improvement, and dynamic power flow control [63]. The TCSC may present the problem of an internal resonance, which must be avoided. This internal resonance also limits TCSC's operating area [24].

The third method uses DFIG back-to-back converters for SSR damping. Although the TCSC and GCSC are more flexible compared to a fixed-series capacitor (FSC) and can provide other benefits to the power network [24], they are a much more expensive solution than fixed series capacitor [24]. Moreover, the DFIG converters have a configuration that is similar to a STATCOM, a shunt FACTS device, whose SSR damping capability has been proven in wind farms [48], [52]. Therefore, in order to use the advantages of FSC without being concerned about the SSR, an auxiliary SSRDC is designed and implemented as part of the DFIG converter controllers.

The SSR damping capability of each method is examined using eigenvalue analysis, performed in MATLAB/Simulink, and time-domain simulations, performed in PSCAD / EMTDC. An auxiliary SSRDC, if necessary, is designed for each method using residue-based analysis and root-locus method. This dissertation is organized as follows.

Chapter 2 presents modal analysis of a DFIG-based series compensated wind farm using Matlab/Simulink. The model of the system includes a wind turbine aerodynamics,

a sixth-order induction generator, a second-order two-mass shaft system, a fourth-order series compensated transmission line, an eighth-order rotor-side converter (RSC) and grid-side converter (GSC) controllers, and a first-order DC-link model.

Chapter 3 focuses mainly on the identification and definition of the main types of the SSR that occur in DFIG wind farms, namely: (1) induction generator effect (SSIGE), (2) torsional interactions (SSTI), and (3) control interactions (SSCI).

Chapter 4 presents application and control of the gate-controlled series capacitor (GCSC) for series compensation and sub-synchronous resonance (SSR) damping in doubly-fed induction generator (DFIG)-based wind farms. A SSRDC is designed for this device using residue-based analysis and root locus diagrams. Using residue-based analysis, the optimal input control signal (ICS) to the SSRDC is identified that can damp the SSR mode without destabilizing other modes, and using root-locus analysis, the required gain for the SSRDC is determined.

Chapter 5 presents application and control of the thyristor-controlled series capacitor (TCSC) for series compensation and sub-synchronous resonance (SSR) damping in doubly-fed induction generator (DFIG)-based wind farms. This chapter includes modeling of the TCSC for SSR analysis, control of TCSC, eigenvalue analysis of a DFIG based wind farm interfaced with a TCSC, and time-domain simulations in PSCAD to support the eigenvalue analysis.

Chapter 6 studies the capability of the rotor-side converter (RSC) and grid-side converter (GSC) controllers of the DFIG in SSR damping. The objective is to design a simple proportional SSRDC by properly choosing an optimum input control signal (ICS) to the SSRDC block so that the SSR mode becomes stable without decreasing or destabilizing the other system modes. Moreover, an optimum point within the RSC and GSC controllers to insert the SSRDC is identified. Moreover, two methods are discussed, in this chapter, in order to estimate the optimum ICS, without measuring it directly.

Chapter 7 a gain-scheduling adaptive SSRDC is designed so that the change of the

system dynamics with system operating point has less influence on the effectiveness of the SSRDC.

Finally, **Chapter 8** concludes the work and presents the future work.

CHAPTER 2

MODELING OF DFIG-BASED WIND TURBINE

This chapter presents a step-by-step modal analysis of a DFIG-based series compensated wind farm using MATLAB/Simulink. The model of the system includes a wind turbine aerodynamics, a sixth-order induction generator, a second-order two-mass shaft system, a fourth-order series compensated transmission line, an eighth-order rotor-side converter (RSC) and grid-side converter (GSC) controllers, and a first-order DC-link model.

2.1 POWER SYSTEM DESCRIPTION

The studied power system, shown in Figure. 2.1, is adapted from the IEEE first benchmark model (FBM) for SSR studies [64]. In this system, a 100 MW DFIG-based offshore wind farm is connected to the infinite bus via a 161 kV series compensated transmission line [65]. The 100 MW wind farm is an aggregated model of 50 wind turbine units, where each unit has a power rating of 2 MW. In fact, a 2 MW wind turbine is scaled up to represent the 100 MW wind farm. This simplification is supported by several studies [66], [67]. The systems data are given in the Appendix.

2.2 FUNDAMENTAL CONCEPTS: SMALL-SIGNAL STABILITY AND *abc* TO *qd*-FRAME TRANSFORMATION

Small-Signal Stability

Small-signal stability is the ability of the power system to maintain stability when the system is subjected to small disturbances [68]. The small-signal stability analysis of a

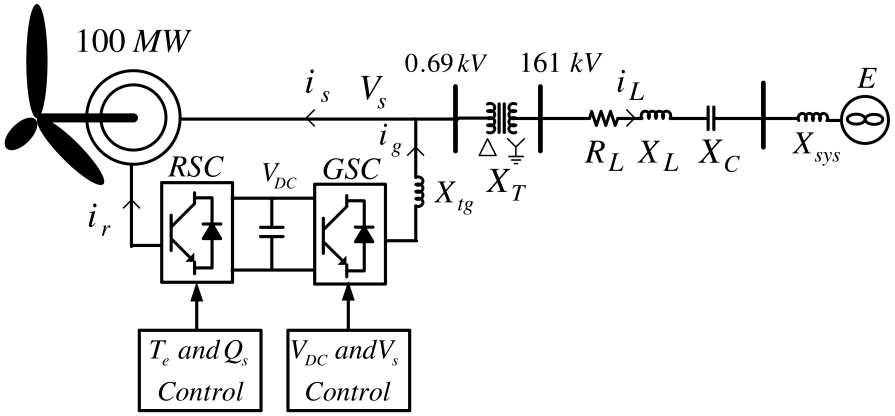

Figure 2.1: One line diagram of the studied power system. R_L = transmission line resistance, X_L = transmission line reactance, X_T = transformer reactance, X_{sys} = system impedance, X_C = fixed series capacitor, X_{tg} = transformer reactance in grid side converter (GSC), V_s = generator's terminal voltage, i_L = line current, i_g = GSC current, i_s = stator current, i_r = rotor current [64].

power system can provide power system designers with valuable information about the inherent small-signal dynamic characteristics of the power system, which will help them in the design process of the power system.

The behavior of any dynamic system, e.g., a power system, can be expressed by a set of n first order nonlinear ordinary differential equations as follows [68]:

$$\dot{x} = f(x,u) \tag{2.1}$$

where $x = [x_1\ x_2\ ...x_n]^T$ is called the state vector, and each elements, i.e. x_i, are called the state variable. Also, the column vector $u = [u_1\ u_2\ ...u_r]^T$ is the input to the dynamic system.

We might also be interested in the output variables, which can be expressed in terms of the state and the input variables as follows [68]:

$$y = g(x,u) \tag{2.2}$$

where $y = [y_1\ y_2\ ...y_m]^T$ is the vector of outputs, and $g(x,u)$ is a vector of nonlinear functions that relates the outputs to the inputs and the state variables.

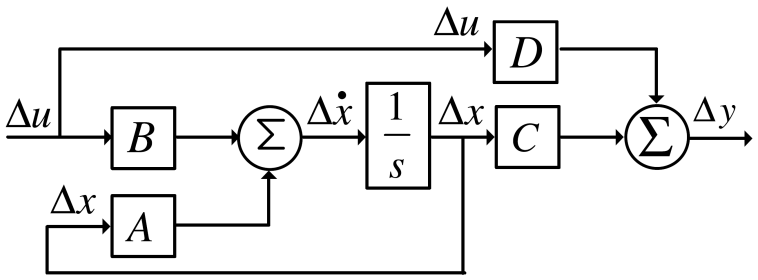

Figure 2.2: Block diagram of the state-space representation.

If the disturbances to the system are considered sufficiently small, one can linearize the differential equations 2.1 and 2.2 around the operating points and can express the system dynamics in state-space form as follows:

$$\Delta\dot{x} = A\,\Delta x + B\,\Delta u \tag{2.3}$$

$$\Delta y = C\,\Delta x + D\,\Delta u \tag{2.4}$$

where A is the state matrix of size $n \times n$, B is the input matrix of size $n \times r$, C is the output matrix of size $m \times n$ and D is the feed-forward matrix of size $m \times r$. The generic block diagram of the state variables used in this paper is shown in Figure 2.2.

Transformation from *abc* to *qd* Frame

In this work, in order to make the calculations easier, three-phase *abc* variables are transformed into *qd* variables using the following equation in matrix notation [69].

$$f^e_{qd0s} = K^e_{qd0s}\; f^e_{abcs} \tag{2.5}$$

where

$$f^e_{qd0s}{}^T = [f^e_{qs}\; f^e_{ds}\; f^e_{0s}] \tag{2.6}$$

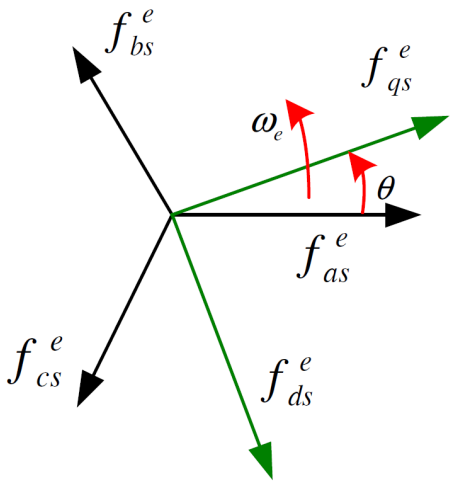

Figure 2.3: Synchronously rotating *qd* frame with respect to the stator *abc*-frame.

$$f^{e}_{abcs}{}^{T} = [f^{e}_{as}\ f^{e}_{bs}\ f^{e}_{cs}] \tag{2.7}$$

$$K^{e}_{qd0s} = \frac{2}{3}\begin{bmatrix} \cos\theta & \cos(\theta-\frac{2\pi}{3}) & \cos(\theta+\frac{2\pi}{3}) \\ \sin\theta & \sin(\theta-\frac{2\pi}{3}) & \sin(\theta+\frac{2\pi}{3}) \\ \frac{1}{2} & \frac{1}{2} & \frac{1}{2} \end{bmatrix} \tag{2.8}$$

where f^e denotes voltage, current, flux linkage, or electric charge, and $\theta = \frac{d\omega_e}{dt}$, where ω_e is the rotating synchronous frame frequency.

Figure 2.3 shows the *qd*-frame with respect to the stator *abc*-frame, where *q*-axis is leading the *d*-axis. Note that in this work, the synchronously rotating reference frame has been used, in which the reference frame rotates at the electrical angular velocity of the air-gap rotating magnetic field generated by stator currents at the fundamental frequency, i.e. ω_e.

2.3 Wind-Turbine Aerodynamics

The wind power can be calculated from the wind speed V_w as follows [70]:

$$T_\omega = \frac{0.5\rho\pi R^2 C_P V_w^2}{\omega_m} \tag{2.9}$$

where T_ω is the wind power $(N.m)$, V_ω is the wind speed (m/s), ρ is the air density (kgm^{-3}), R is the rotor radius of the wind turbine (m), and ω_m is the wind turbine shaft speed $(rad./s)$.

Also, C_P is the power coefficient of the blade given by:

$$C_P = 0.5(\frac{RC_f}{\lambda_w} - 0.022\theta - 2)e^{-0.225\frac{RC_f}{\lambda_\omega}} \tag{2.10}$$

where C_f is the wind turbine blade design constant, and θ is the wind speed pitch angle $(rad.)$

Also, λ_ω is the wind speed tip-speed ratio defined by:

$$\lambda_\omega = \frac{\omega_m R}{V_\omega} \tag{2.11}$$

2.4 A Brief Overview of DFIG Converter Control Methods

In this section, a short overview of rotor-side converter (RSC) and grid-side converter (GSC) controllers is presented.

RSC

Usually, the RSC is used to control the electric torque (or rotor speed) of the DFIG and the power factor at the stator terminals [71]. Different control strategies of the RSC, including vector control (VC) [72] - [74], direct torque control (DTC) [75] - [77], and direct power control (DPC) [78] - [80] have been studied in literature.

In the VC method, the rotor currents are usually controlled using a rotating frame aligned with the stator flux. The VC method controls the electric torque, which is proportional to the q-axis rotor current, through q-axis channel of the rotor current. Moreover,

the reactive power in the machine can be controlled by tracking d-axis component of the rotor current [72] - [74].

In the DTC method, the rotor flux linkage magnitude and the electric toque of the DFIG are directly controlled. This direct control becomes feasible by proper selection of the inverter switching in the rotor side. In order to implement this method, the flux and torque feedbacks are needed, where the former is estimated using the rotor and stator current vectors while the latter is estimated through the estimated rotor flux and the measured rotor currents.

The DPC method is similar to the DTC, but it considers the effect of both the stator and rotor fluxes upon the real and reactive power of the stator. Indeed, this method aims to control directly the real and reactive power of the stator by applying appropriate machine rotor vector voltage [77] - [80].

GSC

The main objective of the GSC is to regulate the DC-link voltage and to permit real power flow through the converter. For the GSC, the VC method is usually adopted [81], where the reference frame is aligned with the grid-voltage vector. Additionally, DPC method has been implemented in literature to control the GSC, resulting in independent real and reactive power flow in the converter [82].

Modeling of the DFIG Converter Controllers

Control loops for RSC and GSC presented in [83] - [85] are considered in this work. Both RSC and GSC controllers are modeled. In order to achieve high efficiency in the DFIG wind farm, the maximum power point tracking (MPPT) is used [83]. Figure 2.4 shows the wind power versus wind turbine shaft speed in per unit for various wind speeds with indication of MPPT curve. To enforce operation on the MPPT curve, for a given wind speed V_{ω}, the optimal reference power and optimal rotational speed are obtained. Note that

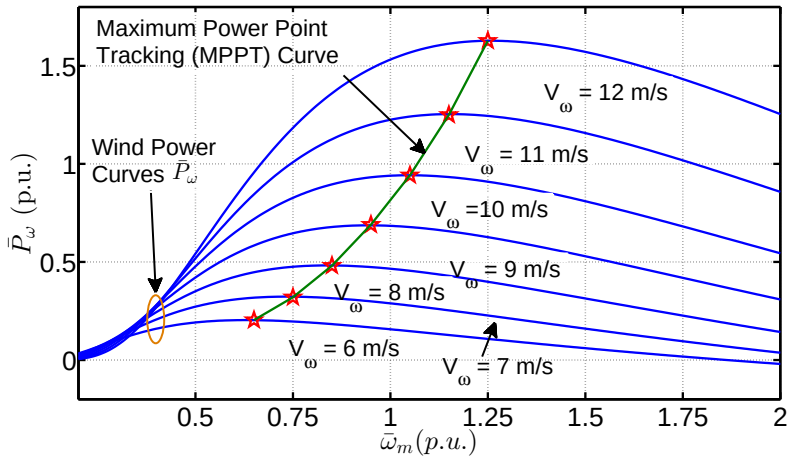

Figure 2.4: Wind power $\bar{P}_m$ $(p.u.)$, wind turbine shaft speed $\bar{\omega}_m$ $(p.u.)$, and wind speed V_ω (m/s) relationship.

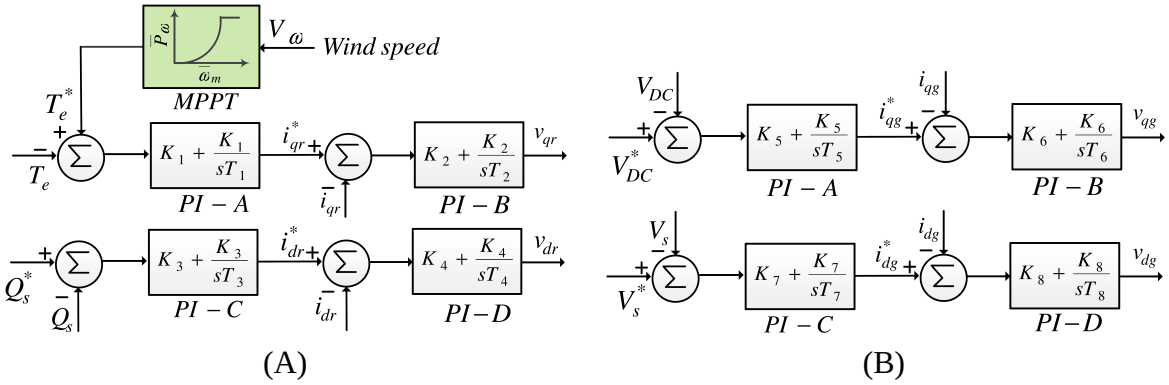

Figure 2.5: A. RSC controllers. B. GSC controllers.

due to power converters ratings, it may not be practical to always work on the MPPT cure. In this case for a very low wind speeds, the DFIG operates at almost constant rotational speed. On the other hand, when the wind speed increases so that it exceeds the turbine torque rating, the DFIG will work in maximum constant torque [86].

The aim of the GSC and RSC are to enable the DFIG to work on the MPPT curve. Note that the converters are assumed to store no energy so that their losses can be neglected, and operate fast enough so that their dynamics can be neglected. Figure 2.5 show the block diagrams of the two controllers. In this paper, the RSC controller is responsible for regulating the electric torque, T_e, and stator reactive power, Q_s. In steady state condition, neglecting

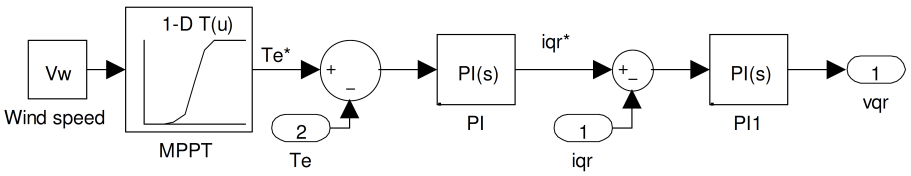

Figure 2.6: GSC regulators in Simulink.

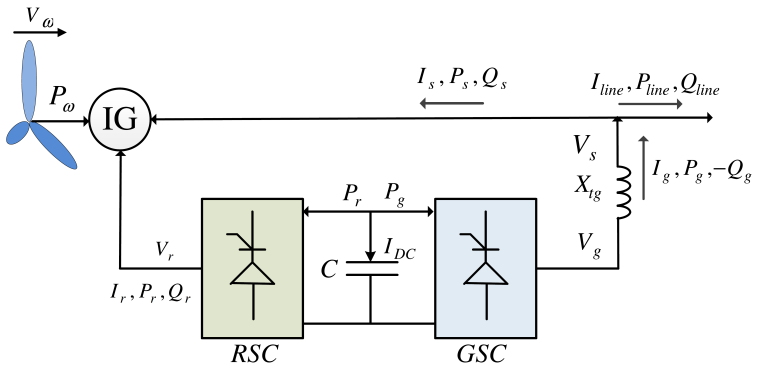

Figure 2.7: Back-to-back converter between the DFIG and grid.

power losses, the wind torque, $\bar{T_\omega} = \frac{\bar{P_\omega}}{\omega_m}$, is equal to electric torque, T_e. Therefore, the reference torque, T_e^*, can be calculated based on the value of $\bar{T^*}_\omega$ determined by the MPPT shown in Figure 2.4 [83] . The value of Q_s^* depends on the chosen reactive power control method which could be either fixed reactive power or unity power factor [83]. In this paper, the latter method is chosen.

Moreover, the GSC is responsible for controlling the DC-link voltage, V_{DC}, and the induction generator's terminal voltage, V_s [83]. The GSC and RSC controllers add eight state variables to the system, due to the eight PI controllers, and their state variables are defined as a vector X_{RG}. One loop of the RSC controllers implemented in Simulink is represented in Figure 2.6. The other controllers have similar structure.

Modeling of the DC-Link

In this work, the DC link capacitor dynamics is considered. Figure 2.7 shows the back-to-back converters between DFIG and grid which are separated by a DC-link. The dynamics

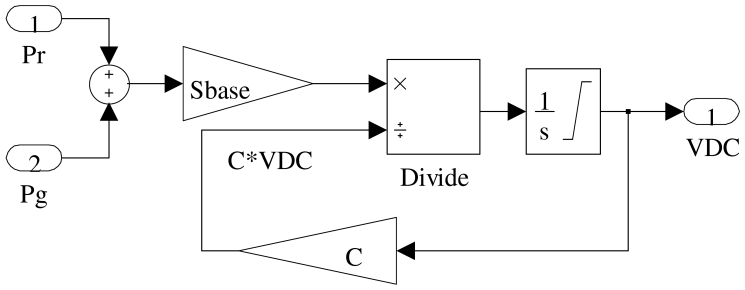

Figure 2.8: DC-link model in Matlab/Simulink.

of the DC-link can be expressed by a first order model as follows [87]:

$$-Cv_{DC}\frac{dv_{DC}}{dt} = P_r + P_g \tag{2.12}$$

where the rotor side converter's (RSC) active power P_r, and the grid-side converter's (GSC) active power, P_g, are given as follows [69]:

$$P_r = 0.5\,(v_{qr}\,i_{qr} + v_{dr}\,i_{dr}) \tag{2.13}$$

$$P_g = 0.5\,(v_{qg}\,i_{qg} + v_{dg}\,i_{dg}) \tag{2.14}$$

Modeling of the DC-link in Matlab/Simulink is shown in 2.8. Notice that after adding P_r and P_g, they are multiplied by the based power, S_{base}, in order to obtain the power in MW. This is necessary, as we have not considered per unit value for the DC-link, and all values in this block are in actual physical values.

2.5 Modeling of the Induction Machine

Using the information given in Section 2.2, the induction machine equations in *abc*-frame are transformed into the synchronously rotating *qd*-frame. If the DFIG currents are selected as the state variables, then the DFIG *qd* model in per unit will be as follows, where the input variables are the DFIG voltages [69]:

$$\dot{X}_{IG} = A_{IG}X_{IG} + B_{IG}U_{IG} \tag{2.15}$$

where

$$X_{IG} = [i_{qs}\ i_{ds}\ i_{0s}\ i_{qr}\ i_{dr}\ i_{0r}]^T \tag{2.16}$$

$$U_{IG} = [v_{qs}\ v_{ds}\ v_{0s}\ v_{qr}\ v_{dr}\ v_{0r}]^T \tag{2.17}$$

where i_{qs}, i_{ds}, i_{qr}, i_{dr} are the stator and rotor qd-axis currents $(p.u.)$, v_{qs}, v_{ds}, v_{qr}, v_{dr} are the stator and rotor qd-axis voltages $(p.u.)$, and i_{0s}, i_{0r}, v_{0s}, v_{0r} are the stator and rotor zero sequence current and voltage components $(p.u.)$, respectively.

The A_{DFIG} and B_{DFIG} matrices are defined as follows. We first define the matrices given in Eq. 2.18 and Eq. 2.19.

$$F = \begin{bmatrix} R_s & \frac{\omega_e}{\omega_b}X_{SS} & 0 & 0 & \frac{\omega_e}{\omega_b}X_M & 0 \\ -\frac{\omega_e}{\omega_b}X_{SS} & R_s & 0 & -\frac{\omega_e}{\omega_b}X_M & 0 & 0 \\ 0 & 0 & R_s & 0 & 0 & 0 \\ 0 & \frac{(\omega_e-\omega_r)}{\omega_b}X_M & 0 & R_r & 0 & \frac{(\omega_e-\omega_r)}{\omega_b}X_{rr} \\ -\frac{(\omega_e-\omega_r)}{\omega_b}X_M & 0 & 0 & -\frac{(\omega_e-\omega_r)}{\omega_b}X_{rr} & R_r & 0 \\ 0 & 0 & 0 & 0 & 0 & R_r \end{bmatrix} \tag{2.18}$$

$$G = \begin{bmatrix} X_{ss} & 0 & 0 & X_M & 0 & 0 \\ 0 & X_{ss} & 0 & 0 & X_M & 0 \\ 0 & 0 & X_{ls} & 0 & 0 & 0 \\ X_M & 0 & 0 & X_{rr} & 0 & 0 \\ 0 & X_M & 0 & 0 & X_{rr} & 0 \\ 0 & 0 & 0 & 0 & 0 & X_{lr} \end{bmatrix} \tag{2.19}$$

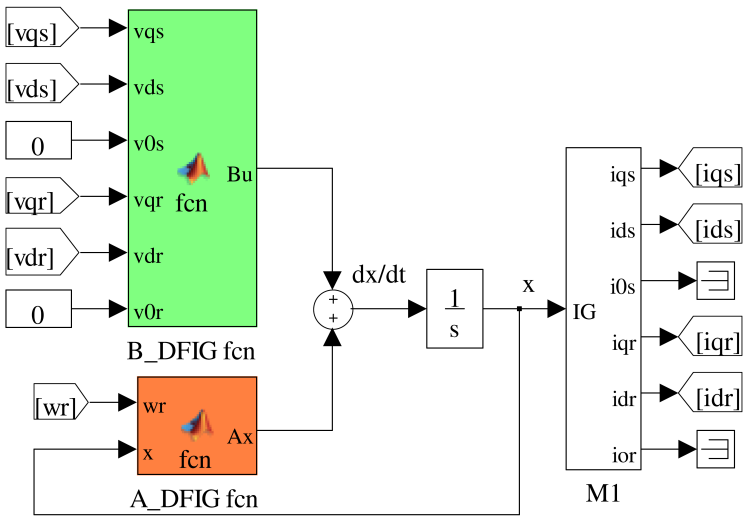

Figure 2.9: DFIG model in Matlab/Simulink.

Then:

$$A_{DFIG} = -\omega_b \cdot G^{-1} \cdot F \tag{2.20}$$

$$B_{DFIG} = \omega_b \cdot G^{-1} \tag{2.21}$$

In Eq. 2.18 and 2.19: X_{lr} is the rotor leakage reactance $(p.u.)$, X_{ls} is the stator leakage reactance $(p.u.)$, X_M is the magnetizing reactance $(p.u.)$, $X_{ss} = X_{ls}+X_M$ $(p.u.)$, X_{rr} equals to $X_{lr}+X_M$ $(p.u.)$, R_r is the rotor resistance $(p.u.)$, R_s is the stator resistance $(p.u.)$, ω_b is the base radian frequency $(rad./s)$, ω_r is the generator rotor speed $(rad./s)$, and ω_e is the rotating synchronous frame frequency $(rad./s)$.

Eq. 3.14 was implemented in Matlab/Simulink. The simulated system is given in Figure 2.9. As seen in this figure, the inputs to the system are the DFIG *qd*-frame stator and rotor voltages. Also, the state variables are the DFIG *qd*-frame stator and rotor currents, as shown in Figure 2.9. Note that because we are considering a balanced system, the stator and rotor zero-sequence voltage components, i.e. v_{0s} and v_{0r}, are set to zero. Also, note that the input ω_r to the system is the generator rotor speed in $(rad./s)$, which is provided by the shaft equations, which will be explained in the next subsection.

2.6 Modeling of Shaft System

The shaft of the wind turbine system can be represented by two-mass system. The first mass represents the low-speed turbine and the second mass represents the high-speed generator, and the two mass connections are modeled as spring and a damper. The motion equations then can be expressed as 3 first order differential equations in per unit as follows [87]:

$$\dot{X}_{shaft} = A_{shaft} X_{shaft} + B_{shaft} U_{shaft} \tag{2.22}$$

where

$$X_{shaft} = [\bar{\omega}_m \ \bar{\omega}_r \ T_{tg}]^T \tag{2.23}$$

$$U_{shaft} = [\bar{T}_\omega \ T_e \ 0]^T \tag{2.24}$$

The A_{shaft} and B_{shaft} matrices are defined as follows:

$$A_{shaft} = \begin{bmatrix} \frac{(-D_t - D_{tg})}{2H_t} & \frac{D_{tg}}{2H_t} & \frac{-1}{2H_t} \\ \frac{D_{tg}}{2H_g} & \frac{(-D_t - D_{tg})}{2H_g} & \frac{-1}{2H_g} \\ K_{tg}\omega_b & -K_{tg}\omega_b & 0 \end{bmatrix} \tag{2.25}$$

$$B_{shaft} = \begin{bmatrix} \frac{1}{2H_t} & 0 & 0 \\ 0 & \frac{1}{2H_g} & 0 \\ 0 & 0 & 1 \end{bmatrix} \tag{2.26}$$

In the shaft equations, $\bar{\omega}_m$ is the turbine shaft speed $(p.u.)$, $\bar{\omega}_r$ is the generator rotor speed $(p.u.)$, $\bar{T}_\omega$ is the wind torque $(p.u.)$, D_g and D_t are damping coefficient of generator and turbine $(p.u.)$, D_{tg} is the damping coefficient between the two masses $(p.u.)$, K_{tg} is the inertia constant of turbine and generator $(p.u/rad.)$, and H_g and H_t are the inertia constants of generator and turbine (s).

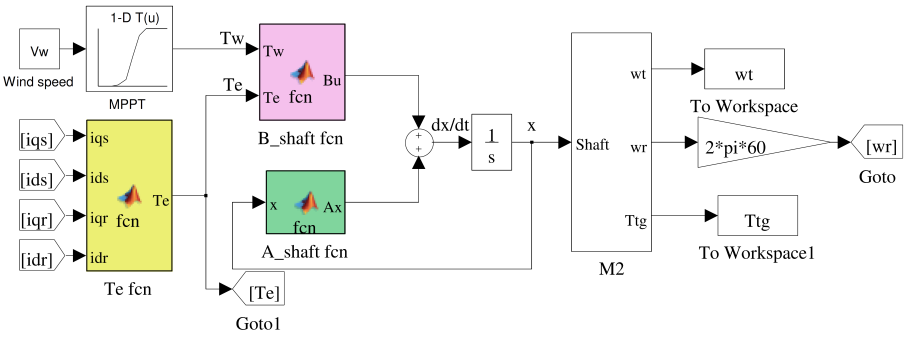

Figure 2.10: The shaft system model in Matlab/Simulink.

In shaft equations, the state variables are wind turbine speed ω_t, generator rotor speed ω_r, and internal torque of the two-mass system T_{tg}. Also, the inputs to the two-mass model are wind torque T_ω and electric torque T_e. The optimal value of the wind torque for any given wind speed can be obtained using the MPPT curve shown in 2.4. Also, the value of the electric torque can be calculated using the following equation [69]:

$$T_e = 0.5\, X_M \left(i_{qs}\, i_{dr} - i_{ds}\, i_{qr}\right) \tag{2.27}$$

Figure 2.10. represents the modeling of the shaft system in Matlab/Simulink. As seen in this figure, the DFIG stator currents, i.e. i_{qs}, i_{ds}, and rotor currents, i.e. i_{qr}, i_{dr}, are applied to the Matlab Function (fcn), T_e, to calculate electric torque using Eq. 2.27. Then Eq. 3.17 is implemented in fcn block A_{shaft} and B_{shaft} to create the shaft model. Also, using this system, the state variable ω_r is provided to the DFIG model, as seen in Figure 2.9 and 2.10.

2.7 Modeling of Transmission Line

The transformation explained in Section 2.2 is used to convert the transmission line equations from *abc*-frame to *qd*-frame. Considering the line current and voltage across the capacitor as the state variables, the transmission line equations in *qd*-frame can be expressed in the matrix form as follows [69]:

$$\dot{X}_{Tline} = A_{Tline}X_{Tline} + B_{Tline}U_{Tline} \tag{2.28}$$

where

$$X_{Tline} = [i_{ql}\ i_{dl}\ v_{qc}\ v_{dc}]^T \tag{2.29}$$

$$U_{Tline} = [\frac{(v_{qs} - E_{Bq})}{X_L}\ \ \frac{(v_{ds} - E_{Bd})}{X_L}\ \ 0\ \ 0]^T \tag{2.30}$$

The A_{Tline} and B_{Tline} matrices are defined as follows:

$$A_{Tline} = \begin{bmatrix} \frac{-R_L}{X_L} & -\bar{\omega}_e & \frac{-1}{X_L} & 0 \\ \bar{\omega}_e & \frac{-R_L}{X_L} & 0 & \frac{-1}{X_L} \\ X_C & 0 & -\bar{\omega}_e & 0 \\ 0 & X_C & \bar{\omega}_e & 0 \end{bmatrix} \tag{2.31}$$

$$B_{Tline} = \begin{bmatrix} \omega_b & 0 & 0 & 0 \\ 0 & \omega_b & 0 & 0 \\ 0 & 0 & 1 & 0 \\ 0 & 0 & 0 & 1 \end{bmatrix} \tag{2.32}$$

where i_{ql} and i_{dl} are the transmission line qd-axis currents $(p.u.)$, v_{qc} and v_{dc} are the series capacitor's qd-axis voltages $(p.u.)$, R_L is the transmission line resistance $(p.u.)$, X_L is the transmission line reactance $(p.u.)$, X_C is the fixed series capacitor $(p.u.)$, E_{Bq} and E_{Bd} are the infinite bus qd-axis voltages $(p.u.)$, and $\bar{\omega}_e$ is the rotating synchronous frame frequency $(p.u.)$

Since we are dealing with a three-phase balanced system, the zero sequence components can be neglected. Whereupon, it can be observed from these equations that the state

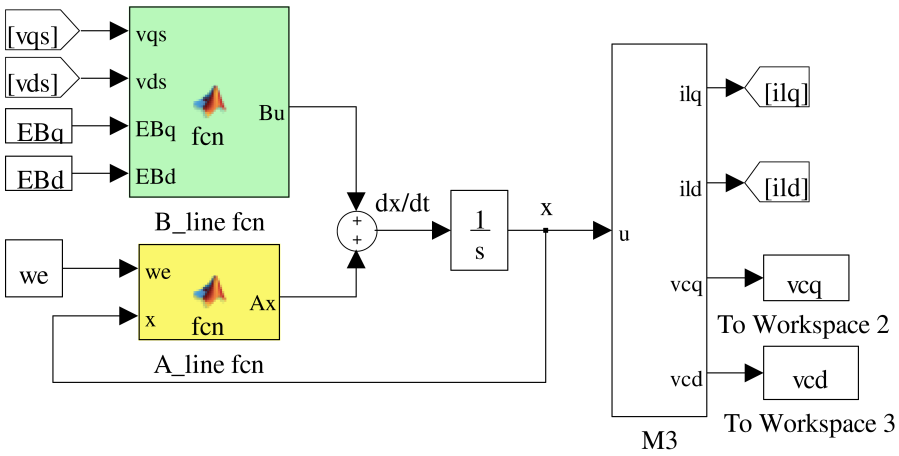

Figure 2.11: Transmission line model in Matlab/Simulink.

variables in the transmission line system are i_{lq}, i_{ld}, v_{cq}, and v_{cd}. The Simulink model of the transmission line in a synchronously rotating qd-frame is shown in Figure 2.11.

2.8 Integrating the Models

So far dynamic equations of the whole system shown in Figure 2.1 have been presented. However, more algebraic equations are needed for integration of each element, which will be explained in this section. By applying KCL at the common point of the stator, GSC, and transmission line (see Figure 2.7), the first equation can be obtained as follows:

$$I_g = I_s + I_{line} \tag{2.33}$$

This equation gives:

$$i_{qg} = i_{qs} + i_{ql} \; and \; i_{dg} = i_{ds} + i_{dl} \tag{2.34}$$

In this work, the transformer in GSC-side of the generator is considered lossless, and its dynamics is neglected. Considering this, the second equation can be derived by applying a KVL starting from GSC and ending to the common point of the stator, GSC, and transmission line (see Figure 2.7) as follows:

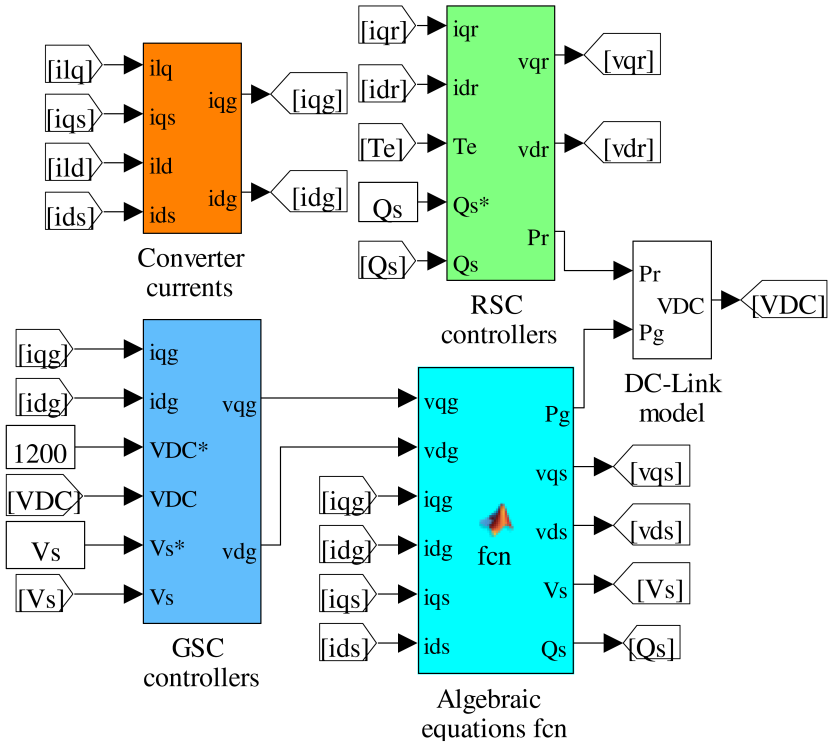

Figure 2.12: RSC and GSC controllers, DC-link, and algebraic equations in Matlab/Simulink.

$$V_g - V_s = jX_{tg}\, I_g \tag{2.35}$$

Performing some algebraic manipulations in this equation will result in:

$$v_{qs} = v_{qg} - X_{tg}\, i_{dg} \quad v_{ds} = v_{dg} + X_{tg}\, i_{qg} \tag{2.36}$$

Figure 2.12 shows the GSC and RSC controllers and DC-link model in Matlab/Simulink. Also, the mentioned algebraic equations are implemented in “Converter currents” block and “Algebraic equations” fcn , as it can be observed in Figure 2.12.

Considering the modeling of the system shown in Figure 2.1 given in this section, the entire DFIG system is a 22^{nd} order and can be expressed as:

$$\dot{X} = f(X, U, t) \tag{2.37}$$

where

$$X = [X_{IG}^T \; X_{shaft}^T \; X_{Tline}^T \; v_{dc} \; X_{RG}^T]^T \tag{2.38}$$

Here, the modeling of the entire system is completed, and the individual models explained above are integrated, and the entire system is named and saved in the computer as "DFIG" to compose a DFIG-based wind farm connected to a series compensated transmission line. Out of 22 state variables, 3 state variables are related to the shaft system, 6 state variables belong to the DFIG model, 4 state variables are related to the transmission line, 1 state variable is for the DC-link, and 8 state variables model the RSC and GSC controllers.

2.9 Calculation of the System Eigenvalues

Matlab/Simulink can estimate the state-space matrices A, B, C, and D in a linearized approximation using small perturbations in the states and inputs to numerically calculate the partial derivatives [88]. For the developed model in Matlab/Simulink, after providing the initial values of each state, the eigenvalues of the system are obtained using the following commands in Matlab:

$$<< \begin{bmatrix} A & B & C & D \end{bmatrix} = linmod\,('DFIG');\; Eigenvalues = eig(A); \tag{2.39}$$

2.10 Summary

This chapter has presented a step-by-step comprehensive approach on modal analysis of a series compensated DFIG-based wind farm in Matlab/Simulink. A $6th$ order model has been used for the DFIG including stator and rotor dynamics, and a $3rd$, $4th$, and $1st$ order models have been applied for the drive train two-mass model of the shaft system, series compensated transmission line, and the DC-link, respectively. Also, the dynamics of the both grid-side converter (GSC) and rotor-side converter (RSC) controllers have been considered, which adds 8 more orders to the system. The presented models have been sup-

ported by the corresponding Simulink blocks in order to help the readers to better understand the modeling process, which provides a useful understanding of the grid-connected series compensated DFIG wind farm's inherent dynamics.

CHAPTER 3

SERIES COMPENSATION AND SSR ANALYSIS IN DFIG-BASED WIND FARMS: DEFINITIONS AND PROBLEM IDENTIFICATION

This chapter focuses mainly on the identification and definition of the main types of the SSR that occur in DFIG wind farms, namely: (1) induction generator effect (SSIGE or simply SSR in this work), (2) torsional interactions (SSTI), and (3) control interactions (SSCI). Regarding the SSIGE, first a simple definition of the SSIGE is given; then, using eigenvalue analysis and time-domain simulations, it is shown that the DFIG wind farm can be highly unstable due to the SSIGE; finally, the impact of wind speed and compensation level variations on the SSIGE is explained. Regarding the SSTI, first a descriptive definition is given; then, the real world possibility of the SSTI in DFIG wind farm is studied; finally, the impact of the stiffness coefficient and compensation level variations on this type of SSR is investigated. Regarding the SSCI, since it may be confused with the SSIGE, a simple definition of the SSCI and its mechanism in DFIG wind farm are presented.

3.1 SERIES COMPENSATION BASICS

In order to briefly explain this phenomenon, a simple lossless two-machine system, where the sending point and receiving points voltages are assumed to have the same magnitude, is considered as shown in Figure 3.1. (A). In this figure, the effective transmission line impedance considering the series capacitor is obtained as follows:

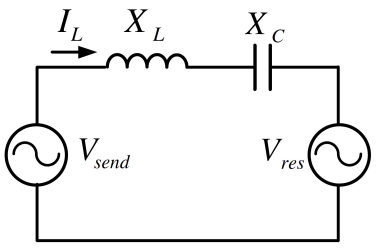

(A)

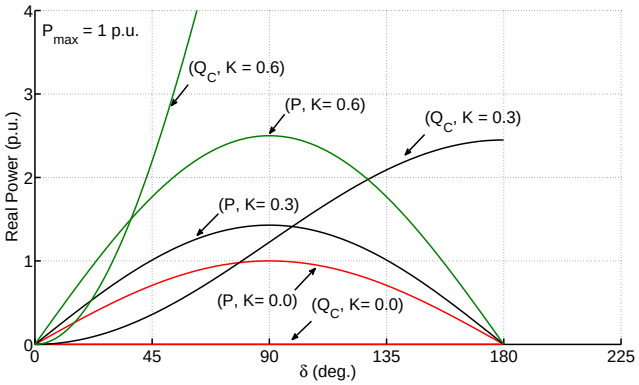

(B)

Figure 3.1: (A) A simple lossless series compensated two-machine system. (B) Variation of transmission real power of line and injected reactive power by series capacitor versus angle δ, for different values of compensation levels.

$$X_{Leff} = X_L - X_C \tag{3.1}$$

The series compensation level (or also called the degree of series compensation) K is defined as:

$$K = \frac{X_C}{X_L} \quad 0 \leq K < 1 \quad or \quad 0\% \leq K < 100\% \tag{3.2}$$

Substitution of Eq. 3.2 in Eq. 3.1 will result in:

$$X_{Leff} = (1-K)X_L \tag{3.3}$$

If we assume in Figure 3.1. (A) that $V_{send} = V_{res} = V$, then the line current and real power are derived as follows [24]:

$$I_L = \frac{2V}{(1-K)X_L} \sin\frac{\delta}{2} \tag{3.4}$$

$$P = \frac{P_{max}}{(1-K)} \sin\delta \tag{3.5}$$

where P_{max} is defined as:

$$P_{max} = \frac{V^2}{X_L} \tag{3.6}$$

Additionally, the injected reactive power to the line by the series capacitor can be derived as [24]:

$$Q_C = 2P_{max}\frac{K}{(1-K)^2}(1-\cos\delta) \tag{3.7}$$

Figure 3.1. (B) represents the real power P and the reactive power Q_C versus δ, for different values of series compensation levels. In this figure, it is assumed that P_{max} is equal to 1 $p.u.$. It can be observed that the transmissible real power of the line P increases, as it is expected from Eq. 3.5, when the series compensation level K increases. Likewise, the injected reactive power by the series capacitor Q_C increases, when K increases. Therefore, the basic idea about series compensation is to cancel out a portion of the inductive impedance of a transmission line using the capacitive impedance of the series capacitor. This reduces the total inductive reactance of the transmission line, as if the line has been physically shortened.

3.2 Induction Generator Effect (SSIGE)

The general expression of the stator current in a series compensated WTGS can be defined as [89]:

$$i_L(t) = A\sin(\omega_s t + \phi_1) + Be^{-\alpha t}\sin(\omega_n t + \phi_2) \tag{3.8}$$

where ω_s the electric fundamental frequency and ω_n is the natural frequency of the electric network, and it can be obtained as [89]:

$$\frac{\omega_n}{2\pi} = f_n = f_s\sqrt{\frac{KX_e}{\sum X}} \tag{3.9}$$

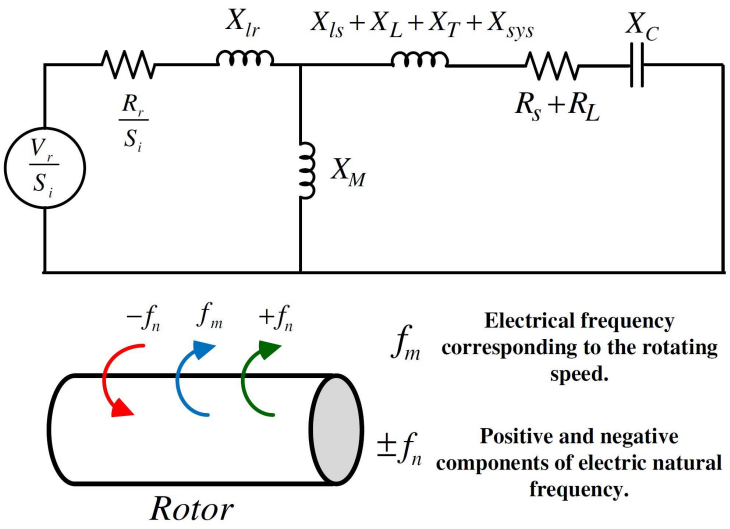

Figure 3.2: Equivalent circuit of the system under sub-synchronous and super-synchronous frequencies.

where $K = \frac{X_C}{X_e}$ is the compensation level, $X_e = X_L + X_T$ $(p.u.)$, $\sum X$ is the entire inductive reactance seen from the infinite bus $(p.u.)$, f_n is the natural frequency of the electric system (Hz), and f_s is the frequency of the system (Hz).

Figure 3.2 shows the equivalent circuit of the DFIG wind turbine under sub-and-super-synchronous frequencies. This figure also shows the status of the positive and negative components of the electric natural frequency with regard to the electrical frequency corresponding to the rotating speed. At sub-synchronous and super synchronous frequencies, the slip is given by S_1 and S_2, respectively, as follows:

$$S_1 = \frac{f_n - f_m}{f_n}, \quad S_2 = \frac{f_n + f_m}{f_n} \tag{3.10}$$

The super-synchronous slip, i.e. S_2 in Eq. 3.10, is always a positive value, and consequently, $\frac{R_r}{S_2}$ in Figure 3.2 is a positive value. Thus, the DFIG wind farm is stable at this frequency. On the other hand, the sub-synchronous slip, i.e. S_1 in Eq. 3.10, is a negative number since the electric natural frequency, f_n, is less than the electric frequency corresponding to the rotating speed, f_m. If the magnitude of the equivalent rotor resistance, i.e. $\frac{R_r}{S} < 0$, exceeds the sum of the resistances of the armature and the network, there will be a

negative resistance at the sub-synchronous frequency, and the sub-synchronous current will increase with time. This phenomenon is called Induction Generator Effect (IGE), which only involves rotor electrical dynamics [64], and is termed as SSIGE in this work.

SSIGE Modes and Participation Factors

Participation factor is a measure of the relative participation of j^{th} state variable in the i^{th} mode of the system. The magnitude of the normalized participation factors for an eigenvalue, λ_i, is defined as [68]:

$$P_{ji} = \frac{|\Psi_{ji}||\Phi_{ij}|}{\sum_{k=1}^{n} |\Psi_{jk}||\Phi_{kj}|} \tag{3.11}$$

where P_{ji} is the participation factor, n is the number of modes or state variables, and Ψ and Φ are right and left eigenvectors, respectively.

Table 3.1 and 3.2 show the eigenvalues and participation factors of the system when the wind speed is 7 m/s and the compensation level is 75%. In these tables, larger participation factors in each column are bolded. By looking at these tables, one can readily find the participation of each state variable in system modes. For example, based on Table 3.1 and using participation factors related to $\lambda_{9,10}$, one can see that this mode is associated primarily to the i_{qs}, i_{dr}, and DC link voltage, v_{DC}. Also, using Table 3.1 it can be observed that $\bar{\omega}_m$ and rotor-side converter PI-D have a high participation in mode $\lambda_{11,12}$. In 3.2, λ_{13} to λ_{22} are non-oscillatory and stable modes, and one can easily find the participation of each state variables on these modes by looking at this table. These modes will not be further discussed.

Identification of System Modes

In this section, the nature of modes $\lambda_{1,2}$, $\lambda_{3,4}$, $\lambda_{5,6}$, $\lambda_{7,8}$ is identified.

Table 3.1: The system modes and participation factors at 75% series compensation and 7 m/s wind speed (Part I)

	$\lambda_{1,2}$ 0.128 ± j131.913	$\lambda_{3,4}$ -5.506 ± j617.197	$\lambda_{5,6}$ -9.911 ± j99.969	$\lambda_{7,8}$ -0.922 ± j5.999	$\lambda_{9,10}$ -875.428 ± j4217.869	$\lambda_{11,12}$ -0.115 ± j0.524
q-axis stator current-i_{qs}	**0.2791**	**0.2210**	**0.2783**	0.0031	**0.3435**	0.0102
d-axis stator current-i_{ds}	**0.2081**	**0.1755**	**0.2057**	0.0971	0.09770	0.0280
zero-seq. stator current-i_{0s}	0.0000	0.0000	0.0000	0.0000	0.0000	0.0000
q-axis rotor current-i_{qr}	**0.2790**	**0.2027**	**0.2907**	0.0034	**0.1319**	0.0115
d-axis rotor current-i_{dr}	**0.2082**	**0.1610**	**0.2172**	**0.1117**	0.0830	0.0321
zero-seq. rotor current-i_{0r}	0.0000	0.0000	0.0000	0.0000	0.0000	0.0000
q-axis cap. voltage-v_{cq}	0.0069	0.0671	0.0016	0.0030	0.0003	0.0008
d-axis cap. voltage-v_{cd}	0.0066	0.0689	0.0015	0.0000	0.0000	0.0002
q-axis line current-i_{lq}	0.0050	0.0487	0.0014	0.0000	0.0717	0.0003
d-axis line current-i_{ld}	0.0056	0.0544	0.0017	0.0056	0.0051	0.0016
rotor speed-$\bar{\omega}_r$	0.0007	0.0000	0.0015	**0.3097**	0.0000	0.0594
turbine speed-$\bar{\omega}_m$	0.0000	0.0000	0.0000	0.0668	0.0000	**0.3131**
torque-T_{tg}	0.0000	0.0000	0.0000	**0.3849**	0.0000	0.0167
DC-link voltage-v_{DC}	0.0000	0.0002	0.0000	0.0000	**0.2613**	0.0000
RSC-PI-A	0.0000	0.0000	0.0000	0.0000	0.0000	0.0001
RSC-PI-B	0.0000	0.0000	0.0000	0.0002	0.0000	0.0783
RSC-PI-C	0.0000	0.0000	0.0000	0.0000	0.0000	0.0019
RSC-PI-D	0.0000	0.0000	0.0000	0.0145	0.0000	**0.4388**
GSC-PI-A	0.0000	0.0000	0.0000	0.0000	0.0000	0.0000
GSC-PI-B	0.0000	0.0000	0.0000	0.0000	0.0058	0.0000
GSC-PI-C	0.0000	0.0000	0.0000	0.0000	0.0000	0.0064
GSC-PI-D	0.0003	0.0000	0.0000	0.0000	0.0001	0.0001

Table 3.2: The system modes and participation factors at 75% series compensation and 7 m/s wind speed (Part II).

	λ_{13}	λ_{14}	λ_{15}	λ_{16}	λ_{17}	λ_{18}	λ_{19}	λ_{20}	λ_{21}	λ_{22}
	-2151.368	-114.749	-97.842	-0.500	-0.0143	-0.002	-19.929	-20.800	-0.000	-0.000
q-axis stator current-i_{qs}	**0.2381**	0.0344	0.0005	0.0000	0.0000	0.0000	0.0000	0.0000	0.0000	0.0000
d-axis stator current-i_{ds}	**0.1482**	**0.2785**	0.0689	0.0000	0.0000	0.0000	0.0000	0.0000	0.0000	0.0000
zero-seq. stator current-i_{0s}	0.0000	0.0000	0.0000	0.0000	0.0000	0.0000	**1.0000**	0.0000	0.0000	0.0000
q-axis rotor current-i_{qr}	**0.2223**	0.0334	0.0003	0.0000	0.0000	0.0000	0.0000	0.0000	0.0000	0.0000
d-axis rotor currenti_{dr}	**0.2214**	**0.2866**	0.0714	0.0000	0.0000	0.0000	0.0000	0.0000	0.0000	0.0000
zero-seq. rotor current-i_{0r}	0.0000	0.0000	0.0000	0.0000	0.0000	0.0000	0.0000	**1.0000**	0.0000	0.0000
q-axis cap. voltage-v_{cq}	0.0001	0.0035	0.0010	0.0000	0.0000	0.0000	0.0000	0.0000	0.0000	0.0000
d-axis cap. voltagev_{cd}	0.0015	0.0013	0.0009	0.0000	0.0000	0.0000	0.0000	0.0000	0.0000	0.0000
q-axis line current-i_{lq}	0.0002	0.0006	0.0009	0.0000	0.0000	0.0000	0.0000	0.0000	0.0000	0.0000
d-axis line current-i_{ld}	0.0980	0.0094	0.0029	0.0000	0.0000	0.0000	0.0000	0.0000	0.0000	0.0000
rotor speed-$\bar{\omega}_r$	0.0000	0.0000	0.0000	0.0000	0.0001	0.0001	0.0000	0.0000	0.0128	0.0461
turbine speed-$\bar{\omega}_m$	0.0000	0.0000	0.0000	0.0000	0.0008	0.0005	0.0000	0.0000	0.0612	**0.2198**
torque-T_{tg}	0.0000	0.0000	0.0000	0.0000	0.0000	0.0000	0.0000	0.0000	0.0000	0.0000
DC-link voltage-v_{DC}	0.0430	0.0082	0.0154	0.0000	0.0000	0.0000	0.0000	0.0000	0.0000	0.0000
RSC-PI-A	0.0000	0.0000	0.0000	0.0000	0.0003	0.0003	0.0000	0.0000	**0.2264**	**0.7340**
RSC-PI-B	0.0000	0.0000	0.0000	0.0000	0.0107	0.0047	0.0000	0.0000	**0.6949**	0.0000
RSC-PI-C	0.0000	0.0000	0.0000	0.0000	0.0193	**0.9804**	0.0000	0.0000	0.0025	0.0000
RSC-PI-D	0.0000	0.0001	0.0000	0.0000	0.0071	0.0006	0.0000	0.0000	0.0000	0.0000
GSC-PI-A	0.0000	0.0000	0.0000	**0.9999**	0.0000	0.0000	0.0000	0.0000	0.0000	0.0000
GSC-PI-B	0.0011	0.0525	**0.7099**	0.0001	0.0000	0.0000	0.0000	0.0000	0.0000	0.0000
GSC-PI-C	0.0000	0.0000	0.0000	0.0000	**0.9614**	0.0132	0.0000	0.0000	0.0019	0.0000
GSC-PI-D	0.0258	**0.2911**	**0.1275**	0.0000	0.0000	0.0000	0.0000	0.0000	0.0000	0.0000

Identification of SSR and SupSR Modes

Table 3.1 shows that modes $\lambda_{1,2}$ and $\lambda_{3,4}$ are primarily associated with i_{qs}, i_{ds}, i_{qr}, and i_{dr}. With the frequency of 20.9947 Hz (or 131.913 rad./s) and $\lambda_{3,4}$ with the frequency of 98.23 Hz (or 617.197 rad./s) are the SSR and super-synchronous (SupSR) modes (Mode 1 and Mode 2), respectively. This can be verified using Eq. 3.9, where f_n is calculated to be around 39 Hz. Given the synchronously rotating reference frame, the complementary the SSR and SupSR frequencies are $f_s - f_n = 21$ Hz and $f_s + f_n = 99$ Hz, which matches the frequency of $\lambda_{1,2}$ and $\lambda_{3,4}$. Table 3.1 also shows that the SSR mode at 75% compensation and 7 m/s wind speed is unstable as the real part of this mode is positive, while the SupSR mode is stable.

Identification of Electromechanical Mode

In order to identify the nature of this mode, Table 3.3 shows this mode for different wind speeds and series compensation levels. In this table, the optimum shaft turbine speed and corresponding frequency related to each wind speed is also given using MPPT plot shown in Figure 2.4. It is seen that the frequency of this mode is changed with the change of the wind speed, while changing the compensation level has slight impact on this mode. It can be observed that the frequency of this mode is the complimentary of the frequency of shaft turbine speed. For example, for the wind speed equal to 7 m/s and compensation level equal to 75 %, the frequency of this mode is 99.97 $rad./s$ or 15.9 Hz, and its complementary is calculated to be 44.1 Hz ($60 - 15.9 = 44.1$ Hz). This frequency coincides with the frequency of the shaft turbine, i.e. 45 Hz. This can also be applied to other wind speeds; thus, this mode is related to wind speed change, and therefore, mechanical dynamics. Also, using Table 3.1, it is observed that $\lambda_{5,6}$ is mostly associated with i_{qs} and i_{ds}, i_{qr}, and i_{dr}. Therefore, this mode is related to both mechanical and electrical dynamics and is called electromechanical mode (Mode 3).

Table 3.3: $\lambda_{5,6}$ at different wind speeds and compensation levels.

	7 m/s (0.75 p.u./45 Hz)	8 m/s (0.85 p.u./51 Hz)	9 m/s (0.95 p.u./57 Hz)
75%	-9.911 ± j99.969	-4.909 ± j62.445	-1.889 ± j28.791
80%	-12.767 ± j99.942	-5.498 ± j62.995	-2.123 ± j29.335
90%	-18.475 ± j95.501	-7.330 ± j64.531	-2.704 ± j30.553

Identification of Shaft Mode

From Table 3.1, it is observed that the generator rotor speed $\bar{\omega}_r$ and the mechanical torque between two masses, T_{tg}, have the highest participation in $\lambda_{7,8}$. Therefore, $\lambda_{7,8}$ is related to the shaft mode (Mode 4). The shaft mode has low-frequency, about 0.954 Hz (or 5.999 rad./s), and this mode at the present operating condition is stable. This mode might be unstable if the series compensation level becomes too high, which will cause SSTI.

Calculation of the SSIGE Mode for Different Operating Points of the DFIG

Table 3.4 shows the eigenvalues of the sub-synchronous resonance (SSR) and super - synchronous resonance (SupSR) modes of the system shown in Figure 2.1 for different series compensation levels and wind speeds. As seen in this table, the SSR and SupSR modes are a function of these two variables: (1) the wind speed V_ω and (2) the compensation level K. On the one hand, at a constant wind speed, when the compensation level increases, the stability of the SSR mode decreases while the stability of the SupSR mode slightly increases. Table 3.4 shows that the SSR mode is unstable for $V_\omega = 7\ m/s$ and K = 55%, K = 60%, and K = 65%.

On the other hand, at a constant series compensation level, when the wind speed increases, the stability of both the SSR and SupSR modes increases. Based on Table 3.4, for K = 65% and $V_\omega = 7\ m/s$ the SSR mode is highly unstable, but when V_ω increases, while K is kept constant, the stability of the SSR mode increases. For example, for K = 65% and

Table 3.4: The SSR and SupSR modes of the system at different wind speeds V_ω and compensation levels K.

V_ω (m/s)-K (%)	SSR Mode	SupSR Mode
7 - 50	-1.8784 ± j140.7799	-5.1561 ± j608.9960
7 - 55	**+1.2126** ± j128.5545	-5.2253 ± j620.39633
7 - 60	**+5.9289** ± j118.8507	-5.2812 ± j631.2477
7 - 65	**+9.6991** ± j112.3237	-5.3158 ± j641.5941
8 - 55	-3.7739 ± j128.5441	-5.9986 ± j622.5840
8 - 60	-2.3818 ± j116.5455	-6.1252 ± j633.4910
8 - 65	-0.4696 ± j104.8237	-6.1877 ± j643.7831
9 - 55	-6.8362 ± j122.7589	-6.8150 ± j623.2366
9 - 60	-5.5889 ± 115.9793	-7.0351 ± j637.6388
9 - 65	-3.7165 ± j105.3277	-7.1718 ± j646.5196

V_ω = 8 m/s & 9 m/s, the SSR mode is stable.

Impact of Compensation Level Variations on the Stability of the SSIGE

As mentioned in Section 3.2, the stability of SSIGE depends on both wind speed and compensation level. This section describes why increasing the compensation level decreases the stability of the SSR mode. In order to explain this fact, a specific example- where wind speed is kept constant at V_ω = 7 m/s, while the compensation level changes- is used. Using MPPT curve shown in Figure 2.4, the electrical frequency corresponding to V_ω = 7 m/s is 45 Hz. Note that, the value of the rotor resistance of the DFIG used in this work is $R_r = 0.00549\ p.u.$, as it can be found in the Appendix.

Table 3.5 shows the rotor resistances under sub-and-super-synchronous frequencies for the aforementioned case. Note that if Table 3.4 is used to calculate f_n, since the models are built in a $d-q$ synchronous reference frame, the computed frequencies of the SSR and SupSR modes, given in Table 3.4, are $f_s - f_n$ and $f_s + f_n$, respectively. From Table 3.5, it can be easily observed that by increasing the compensation level, larger negative resistances are provided to the network, which decreases the stability of the SSR mode.

Table 3.5: Rotor resistance under SSR and SupSR frequencies when the wind speed is kept constant at $V_\omega = 7\ m/s$ (45 Hz) and the compensation level changes.

K (%)	$f_n\ Hz$	$\frac{R_r}{S_1}$	$\frac{R_r}{S_2}$
50%	37.59	-0.0278	0.00249
55%	39.54	-0.0397	0.00256
60 %	41.08	-0.0576	0.00262
65%	42.12	-0.0803	0.00265

The reason is that at a constant wind speed, or constant f_m, increasing the compensation level increases the electric natural frequency of the system. Therefore, the absolute value of the DFIG slip S_1 under SSR frequency given in Eq. 3.10 decreases, providing more negative rotor resistance $\frac{R_r}{S_1}$ to the system. This decreases the stability of the SSR mode.

Impact of Wind Speed Variations on the Stability of SSIGE

In order to explain the impact of wind speed variations on the stability of the SSR and SupSR modes, a specific example - where the compensation level is kept constant at K = 65% while the wind speed changes - is used. Using the MPPT curve shown in Figure 2.4, the electrical frequencies corresponding to different wind speeds are obtained. Table 3.6 shows the rotor resistances under sub-and-super-synchronous frequencies for this example. As it can be observed from this table, by increasing the wind speed, the SSR mode becomes more stable. The reason is that by increasing the wind speed - which, in other words, is equivalent to increasing the electrical frequency corresponding to wind speed f_m - the absolute value of the DFIG slip S_1 increases, providing less negative rotor resistance $\frac{R_r}{S_1}$ to the system. This increases the stability of the SSR mode.

Time-Domain Simulation in PSCAD/EMTDC

In order to confirm the eigenvalue analysis provided in Table 3.4, time domain simulations in PSCAD/EMTDC are performed. Figures 3.3 through 3.5 show the IG terminal voltage

Table 3.6: Rotor resistance under SSR and SupSR frequencies when compensation level is kept constant at K = 65% ($f_n = 42.12\ Hz$) and wind speed changes.

$V_\omega\ (m/s)$	$f_m\ Hz$	$\frac{R_r}{S_1}$	$\frac{R_r}{S_2}$
7	45	-0.0803	0.0026
8	51	-0.0260	0.0024
9	57	-0.0155	0.0023

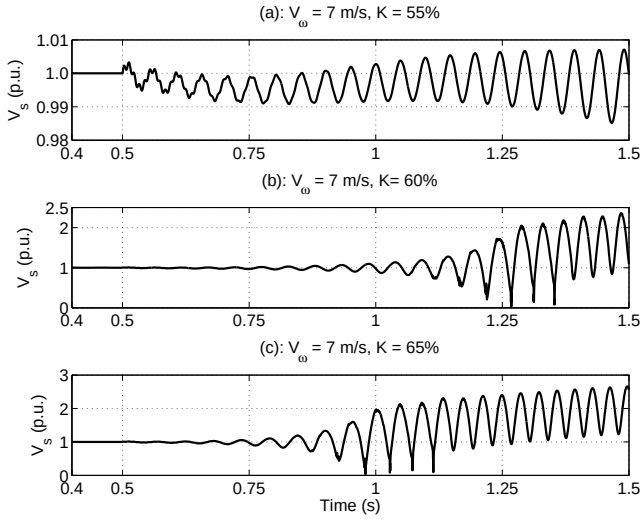

Figure 3.3: Terminal voltage when $V_\omega = 7\ m/s$ and (a) $K = 55\%$ (b) $K = 60\%$ (c) $K = 65\%$.

V_s for different wind speeds and compensation levels. Note that in the given simulation results, the system is first started with a lower series compensation level at which the wind farm is stable, i.e. $K = 50\%$, and then at $t = 0.5\ s$, the compensation level is increased. The following conclusions can be drawn from the simulation results:

1. At lower wind seed, e.g. $V_\omega = 7\ m/s$, when K increases, the stability of the SSR mode decreases, as seen in Figure 3.3.

2. The frequency of the oscillations using Figures 3.3 - (a) - through - (c) are obtained about 20 Hz, 18.18 Hz, and 17.85 Hz for $K = 55\%$, $K = 60\%$ and $K = 65\%$, respectively. These frequencies validate the frequencies obtained using eigenvalue analysis for these cases given in Table 3.4.

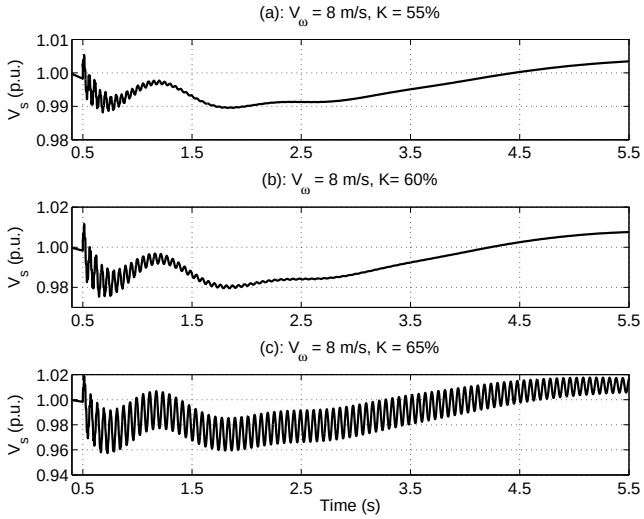

Figure 3.4: Terminal voltage when $V_\omega = 8\ m/s$ and (a) $K = 55\%$ (b) $K = 60\%$ (c) $K = 65\%$.

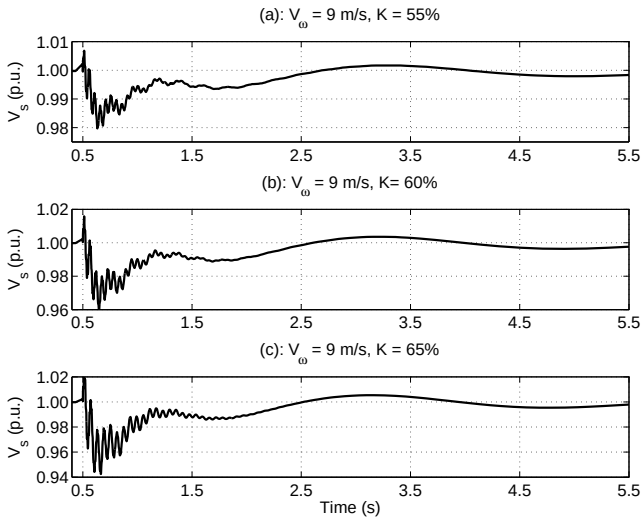

Figure 3.5: Terminal voltage when $V_\omega = 9\ m/s$ and (a) $K = 55\%$ (b) $K = 60\%$ (c) $K = 65\%$.

3. From Figures 3.4 and 3.5, it is observed that increasing the wind speed stabilizes the SSR mode, as expected from Table 3.6. Additionally, these figures show that at a constant wind speed, increasing the compensation level, decreases the stability of the SSIGE mode, as discussed in reference to Table 3.5.

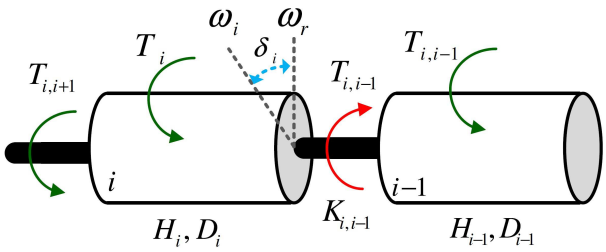

Figure 3.6: Structure of a typical drive-train model. $T_{i,i+1}$ = The torque applied to the i_{th} mass from $(i+1)_{th}$ mass, T_i = external torque applied to i_{th} mass, δ_i = torsional angle of the i_{th} mass, H_i inertia constant of the i_{th} mass, D_i = damping coefficient of the i_{th} mass, $K_{i,i-1}$ = stiffness coefficient between i_{th} and $(i-1)_{th}$ masses.

3.3 Torsional Interactions (SSTI)

In order to analyze the SSTI, it is better first to define the torsional frequencies of a DFIG wind turbine drive-train model. A common way is to represent the rotor as a number of discrete masses connected together by springs defined by damping and stiffness coefficient. Figure 3.6 shows the structure of a typical WTGS drive-train model. The equation of the i_{th} mass motion can be expressed as [90]:

$$2H_i\frac{d\Delta\omega_i}{dt} = T_i + T_{i,i+1} - T_{i,i-1} - D_i\frac{d\delta_i}{dt} \tag{3.12}$$

where

$$T_{i,j} = K_{i,j}\cdot(\delta_j - \delta_i) \tag{3.13}$$

$$\frac{d\delta_i}{dt} = \omega_i - \omega_r = \Delta\omega_i \tag{3.14}$$

If N discrete masses are considered, using Eqs. 3.12 through 3.14, a set of $2N$ differential equations can be obtained, which in a state-space description take the following form [90]:

$$\dot{X} = AX + BU \tag{3.15}$$

where X and U are the state variables vector and the input torque vector, respectively.

Using the state matrix A, the eigenvalues of the drive-train system are a set of complex-conjugate pairs of the form [90]:

$$\lambda_{i,i+1} = -\zeta_i \omega_{ni} \pm j\omega_{ni}\sqrt{1-\zeta_i^2} \tag{3.16}$$

where ζ_i and ω_{ni} are the damping ratio and undamped natural frequency of the i_{th} mass.

As a general case, a rotor with N masses has N modes, where $N-1$ modes represent the torsional modes of oscillation, and one remaining mode represents the oscillation of the entire rotor against the power system.

Using Eq. 3.16, the torsional natural frequency of the i_{th} mass can be obtained as [90]:

$$f_{mi} = \frac{\omega_{ni}\sqrt{1-\zeta_i^2}}{2\pi} \tag{3.17}$$

If generator rotor oscillates at a torsional natural frequency, f_{mi}, this phenomenon induces armature voltage component in the generator at frequencies given by [91]:

$$f_{em_i} = f_s \pm f_{mi} \tag{3.18}$$

If f_{em_i} is close to f_n, which is the electric natural frequency due to series compensation and is given by Eq. 3.9, the sub-synchronous torques generated by this sub-synchronous induced armature voltage can be sustained. This energy exchange between the electric part of the DFIG wind farm and its mechanical part is called ***Torsional Interaction***, and it is termed as SSTI in this work.

Does SSTI Occur in Wind Farms?

In this section, we answer to the question: "Does SSTI occur in wind farms?". The frequency of shaft torsional modes is a strong function of the shaft stiffness coefficient, i.e. $K_{i,j}$ in Figure 3.6. The values of $K_{i,j}$ in wind turbines are much smaller compared to

the values found in steam, hydro, and diesel turbines. The typical value of $K_{i,j}$ reported in the literature is much less than 10 $p.u.\ Torque/rad$. [90], while the values of $K_{i,j}$ for the different sections of a typical steam turbine reported in [64] are in the range 19 - 70 $p.u.\ Torque/rad$..

The low shaft stiffness coefficient in wind turbine drive-train leads to low torsional natural frequencies, which are in the range of 1-5 Hz. Therefore, based on the definition given for SSTI, in order to cause the SSTI in a wind farm, the electric natural frequency of the network should be in the range of 55-59 Hz. In order to obtain such a large electric natural frequency in the network, a very high series compensation level is needed, while in practice, the series compensation is normally not larger than 70% - 75% for reasons such as load balancing with parallel paths, high fault current, and the possible difficulties of power flow control [24]. Hence, the SSTI may not be a concern in WTGS. However, for the sake of completeness of the current work, the impact of shaft stiffness coefficients $K_{i,j}$ and series compensation level K on the SSTI mode is studied.

Impact of Shaft Stiffness Coefficients Variations on the Stability of SSTI

The studied WTGS shown in Figure 2.1 is composed of two masses, the generator and the turbine, and the stiffness coefficient between the turbine and the generator is called $K_{t,g}$. Also, the value of the stiffness coefficient in the studied system in this paper is $K_{t,g}$ = 0.15 $p.u.\ Torque/rad$.. With this $K_{t,g}$, for $V_\omega = 9\ m/s$ and $K = 55\%$, the shaft torsional mode is calculated as $\lambda_{Torsional} = -3.2396 \pm j4.6767$, and this mode is stable. Using $\lambda_{Torsional}$, the torsional natural frequency is calculated to be less than 1 Hz. Therefore, in order to cause the SSTI in the system with the current $K_{t,g}$, f_n has to be about 59 Hz, which requires a very large compensation level.

Figure 3.7 shows the SSR and torsional modes as a function of the stiffness coefficient, $K_{t,g}$, when $V_\omega = 9\ m/s$ and $K = 55\%$. As seen in this figure, by increasing $K_{t,g}$, as soon as

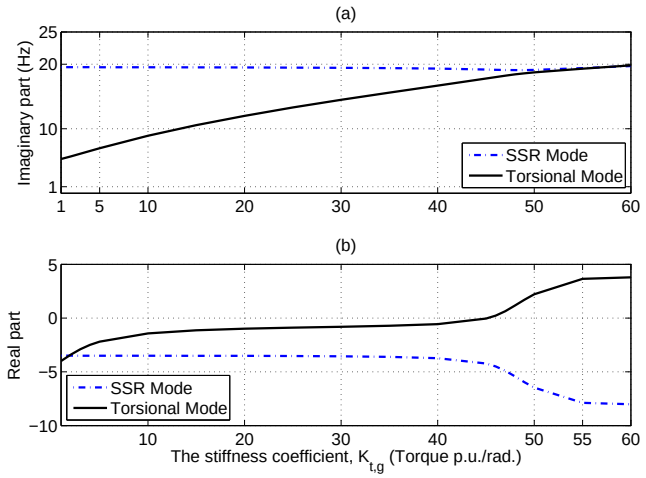

Figure 3.7: SSR and torsional modes versus the stiffness coefficient, $K_{t,g}$, when $V_\omega = 9$ m/s and $K = 55\%$: (a) Imaginary part (Hz) (b) Real part.

the frequency of the torsional mode becomes close to the frequency of the SSR mode, the torsional mode becomes unstable.

Impact of Series Compensation Level Variations on the Stability of SSTI

In order to cause the SSTI in the wind farm, the value of $K_{t,g}$ is increased from 0.15 to 50 $p.u.\ Torque/rad.$. Figure 3.8 shows the SSR and torsional modes as a function of compensation level when $V_\omega = 9\ m/s$. As seen in Figure 3.8 as long as the torsional natural frequency is not close to the SSR mode, the shaft mode is stable. Once the frequency of these modes become close to each other, the shaft mode becomes unstable

Time-Domain Simulation of SSTI in PSCAD/EMTDC

In order to show the SSTI in the WTGS, time-domain simulations in PSCAD/EMTDC are performed. Figure 3.9 shows the system response including the torsional torque between masses I&II $T_{t,g}$, wind turbine speed ω_t, the electric torque T_e, and IG terminal voltage V_s, when $V_\omega = 9\ m/s$ and K changes. Note that in the given simulation results, the system is

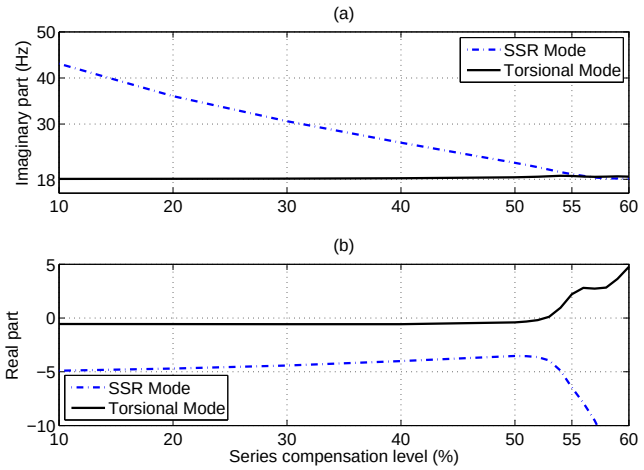

Figure 3.8: SSR and torsional modes versus series compensation level, K, when $V_\omega = 9$ m/s: (a) Imaginary part (Hz) (b) Real part.

first started with a lower series compensation level, $K = 20\%$, and then at $t = 2.5$ s and $t = 8$ s, the compensation level is increased to $K = 50\%$ and $K = 55\%$, respectively. In these simulations, $K_{t,g} = 50$ $p.u.$ $Torque/rad.$. The following conclusions can be drawn from the simulation results:

1. The wind farm is stable at lower compensation levels, i.e. when $K = 20\%$ and $K = 50\%$, as expected from Figure 3.8. However, when the compensation level increases to 55%, the SSTI occurs in the WTGS, and the wind farm goes unstable due to the unstable torsional mode.

2. Even when the torsional mode is stable at lower compensation levels, i.e. when $K = 20\%$ and $K = 50\%$, the SST-TI is very lightly damped. This is due to the fact that the damping ratio of the torsional mode is very small even at these compensation levels, i.e. 0.5% and 0.14% for $K = 20\%$ and $K = 50\%$, respectively.

3. Therefore, in some cases, depending on system parameters, the torsional interaction mode may have a low damping ratio and an SSR damping controller may be desirable.

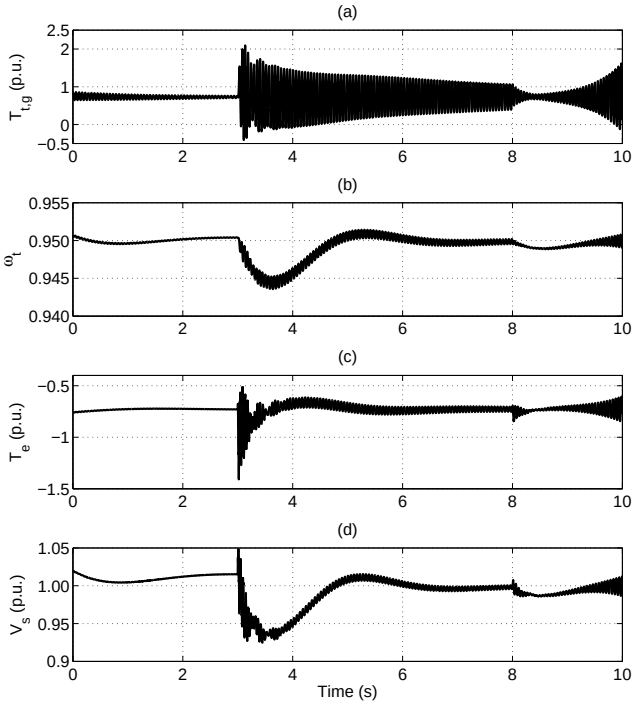

Figure 3.9: The SSTI when $V_\omega = 9\ m/s$ and compensation level changes at different times: (a) $T_{tg}\ (p.u.)$ (b) $\omega_t\ (p.u.)$ (c) $T_e\ (p.u.)$ (d) $V_s\ (p.u.)$.

3.4 Control Interactions (SSCI)

Sub-synchronous control interactions (SSCI) are mainly due to the interactions between DFIG wind turbine controllers and the series compensated transmission line, to which the wind farm is connected. Unlike the beforementioned SSR types, the SSCI does not have well-defined frequencies of concern due to the fact that the frequency of oscillations in SSCI depends not only on the configuration of the series compensated transmission line and induction generator parameters, but also on the wind turbine controller configuration and parameters [37] - [41]. Moreover, the oscillations caused by the SSCI may grow faster compared to previously mentioned SSR type, since the undamped oscillation in SSCI completely depends on the electrical and controller interactions, which have a smaller time constant.

The SSCI has come into prominence since the ERCOT event of 2009 [37] - [41]. A faulted line and subsequent outage in the network caused a large DFIG wind farm to be-

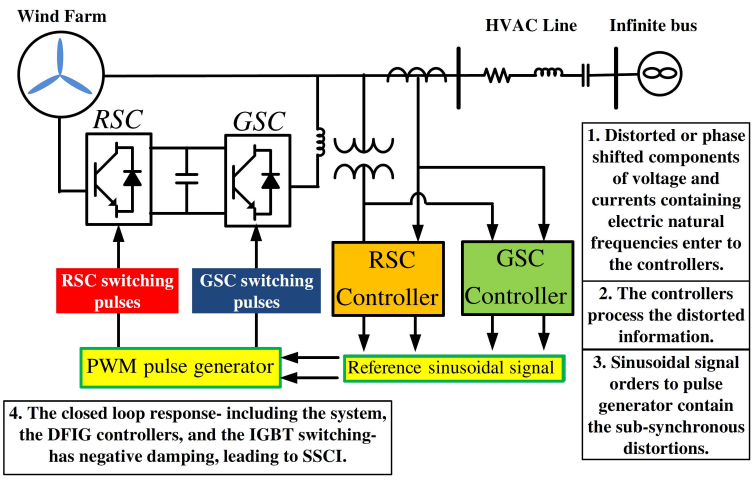

Figure 3.10: The mechanism of the SSCI in WTGS.

come radially connected to the series compensation network, resulting in rapidly increasing of sub-synchronous frequency oscillations leading to damage to both the series capacitor and the wind turbine [37] - [41]. The SSCI system can be simplified as shown in Figure 3.10. According to this figure, as mentioned earlier, the reason for the SSCI is the interaction between the DFIG controllers and the network electric natural frequency.

3.5 Existing and Planned Series Compensated Wind Farms

In 2005 [92], [93], the public utility commission of Texas (PUCT) developed a plan to build 2300 miles of new 345 kV transmission lines to accommodate an increase of 11553 MW of wind energy in West Texas. Some of the transmission lines in the plan were designed to have 50% series compensation. In Figure 3.11, a section of the electric reliability council of Texas (ERCOT) grid is shown, where a 200 MW DFIG wind farm is connected to Bus 2. The nominal voltage in all buses is 138 kV, except for buses 12-16, where the transformers increase the voltage level from 138 kV to 345 kV. The series compensation capacitors are located on the Bus 13-Bus 16 transmission line and on the Bus 15-Bus 16 transmission line, with compensation levels from 50% to 80%. The thick green line in Figure 3.11 is the worst case scenario in terms of susceptibility to SSR, where all other lines in the network

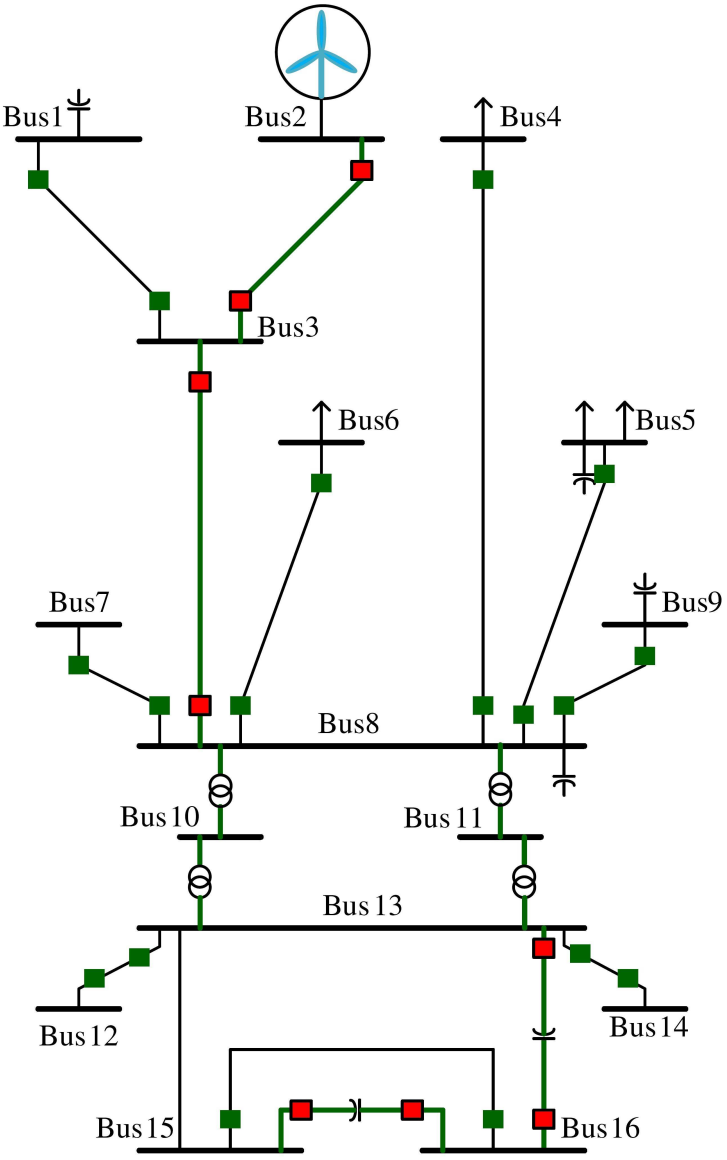

Figure 3.11: Single line diagram of a part of ERCOT grid, where a 200 MW DFIG wind farm is connected to the Bus 2 [37],[40].

are open, and thereby, the wind farm is radially connected to the series compensated lines via Bus 2, Bus 3, Bus 8, Bus 13, Bus 16 and Bus 15. In the ERCOT event of 2009 [37] - [41], a faulted line and subsequent outage in the network caused a large DFIG wind farm to become radially connected to the series compensation network. In this case, the power network shown in Figure 3.11 is reduced to a radial single-machine-infinite bus network. This event resulted in rapidly increasing of sub-synchronous frequency oscillations leading

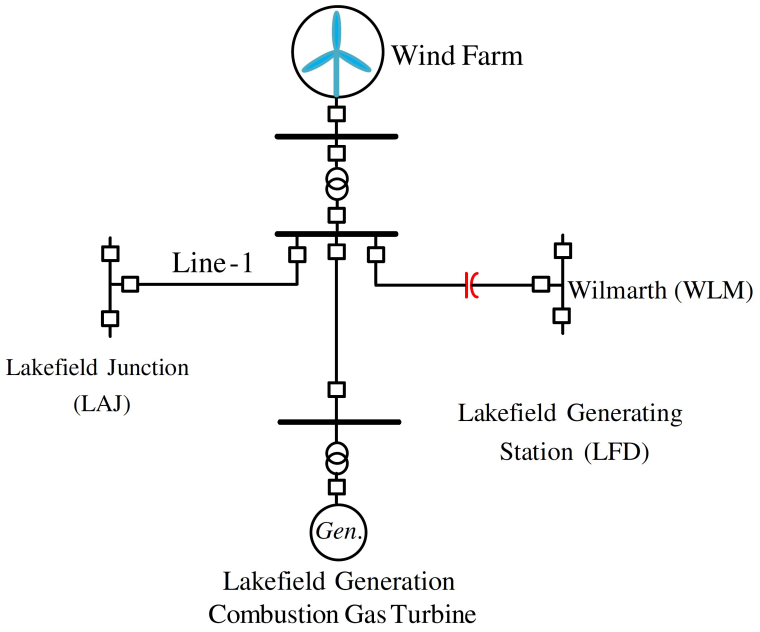

Figure 3.12: Single line diagram of the 54 mile 345 KV Wilmarth (WLM)- Lakefield Generating station (LFD) transmission line connected to the wind farm [57], [94].

to damage to both the series capacitor and the wind turbine [37] - [41]. Note that this case of a wind farm radially connected to series-compensated transmission lines is similar to the system studied in this paper shown in Figure 2.1. This shows the practical relevance of the research presented in this work.

Additionally, with rapid increase of wind power energy in Southern Minnesota and South Dakota, the Xcel Energy Inc. has planned (or already implemented) series compensation in several transmission lines, including a 150-MW DFIG wind farm connected to a 60% series compensation of 54 miles 345 kV Wilmarth (WLM) - Lakefield Generating station (LFD) transmission line, as seen in Figure 3.12 [57], [94]. A switching event around the series compensated transmission line connected to wind farm and combustion turbine generation resulted in growing unstable sub-synchronous oscillations [57].

Moreover, in [95], ABB Inc. has performed a “Dakotas Wind Transmission Study” to investigate the transmission line capacity for up to 500 MW of new wind generation planned to be located at seven different sites. The results revealed that the peak wind gen-

erated power cannot be delivered because the uncompensated transmission line exhibited congestion. The report suggests that providing 35% and 50% series compensation for the existing transmission lines can increase the level of wind generation that can be exported. The ABB Inc. report also states that special studies must be performed in order to avoid the SSR in the system.

In addition, [96] discusses technical requirements for the interconnection to Bonneville Power Administration (BPA), in Pacific Northwest, transmission grid, including series compensation to transmit wind power energy. Also, [97] gives a report regarding reinforcement of transmission lines of Alberta Electric System Operator (AESO) using series compensation. Some of these lines are connected directly or indirectly to wind farms.

3.6 SUMMARY

In this chapter, three possible SSRs in DFIG wind farms including induction generator effect (SSIGE), torsional interactions (SSTI), and control interactions (SSCI) are briefly explained, and impact of some wind farms parameters on these SSRs are investigated using eigenvalue analysis and time-domain simulations in PSCAD/EMTDC.

Regarding the SSIGE, the following conclusions can be drawn:

1. The SSIGE may happen when the equivalent rotor resistance under sub-synchronous frequency, which can be a negative value, exceeds the sum of the positive resistances of the armature and the network.

2. At lower wind speeds and higher compensation levels, the possibility of the SSIGE in DFIG becomes higher.

3. The SSIGE is not related to the mechanical part of the system and is a purely electrical phenomenon.

Regarding the SSTI, the following conclusions can be drawn:

1. The SSTI may happen if the complement of one of the torsional natural frequencies of the drive-train turbine system is close to the electric natural frequency.
2. Because of the low-shaft stiffness coefficient in WTGS, the SSTI may not be a concern.

Regarding the SSCI, the following conclusions can be drawn:

1. The SSCI is an interaction between the DFIG wind turbine controllers and the series compensated transmission line, to which the wind farm is radially connected.
2. The SSCI does not have well-defined frequencies of concern.
3. The oscillations caused by the SSCI may grow faster compared to SSIGE and SSTI.

CHAPTER 4

SSR DAMPING USING GATE - CONTROLLED SERIES CAPACITOR (GCSC)

This chapter presents application and control of the gate-controlled series capacitor (GCSC) for series compensation and sub-synchronous resonance (SSR) damping in doubly-fed induction generator (DFIG)-based wind farms. The GCSC is a new series FACTS device composed of a fixed-capacitor in parallel with a pair of anti-parallel gate-commuted switches. The wind farm is equipped with a GCSC to solve the instability of the wind farm resulting from the SSR mode, and a SSR damping controller (SSRDC) is designed for this device using residue-based analysis and root locus diagrams. Using residue-based analysis, the optimal input control signal (ICS) to the SSRDC is identified that can damp the SSR mode without destabilizing other modes, and using root-locus analysis, the required gain for the SSRDC is determined. Matlab/Simulink is used as a tool for modeling and design, and PSCAD/EMTDC is used for time-domain simulations.

4.1 GCSC: STRUCTURE AND CONTROL

Flexible AC transmission systems (FACTS) are defined as a high-power electronic based system and other static equipment controlling one or several transmission systems to improve their controllability and power transfer capability [24]. Generally, high-power electronic devices include a variety of diodes, transistors, silicon controlled rectifier (SCR), and gate-turn-off thyristors (GTO) [98]. Unlike the conventional thyristors or SCRs, GTOs are fully controllable, and they can be turned on and off by their gate. Nowadays, SCRs and

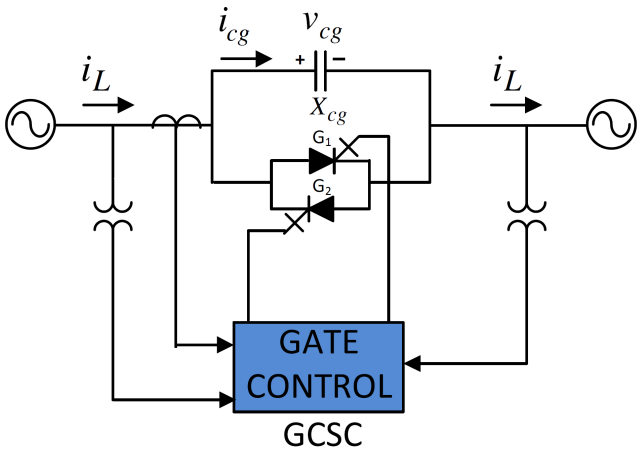

Figure 4.1: Single line configuration of the GCSC. v_{cg} = voltage across the GCSC, i_L = transmission line's current, i_{cg} = GCSC capacitor current, X_{cg} = fixed capacitance of the GCSC.

high power GTOs are widely used for FACTS controllers. Gate-controlled series capacitor (GCSC) is a family of series FACTS devices that uses GTO switches that can be turned on and off by its gate [24].

This section describes the GCSC principles of operation, generated harmonics, and its application for series compensation and SSR damping in DFIG-based wind farms, including power scheduling and SSR damping controller design.

Principle of Operation and Generated Harmonics

A GCSC (one per phase), as shown in Figure 4.1, is composed of a fixed-capacitor in parallel with a pair of GTOs. The switch in the GCSC is turned-off at the angle β, measured from the peak value of the line current. Figure 4.2 shows the line current, capacitor voltage and the GTOs pulses waveform. As seen in this figure, the GTO switch is closed, when $v_{cg}(t)$ is equal to zero. The effective capacitance of the GCSC is given by [24]:

$$X_G = \frac{X_{cg}}{\pi}(2\gamma - \sin 2\gamma) = \frac{X_{cg}}{\pi}(\delta - \sin\delta) \tag{4.1}$$

where γ is the the angle of the advance, δ is the hold off angle, and X_{Cfg} is the fixed

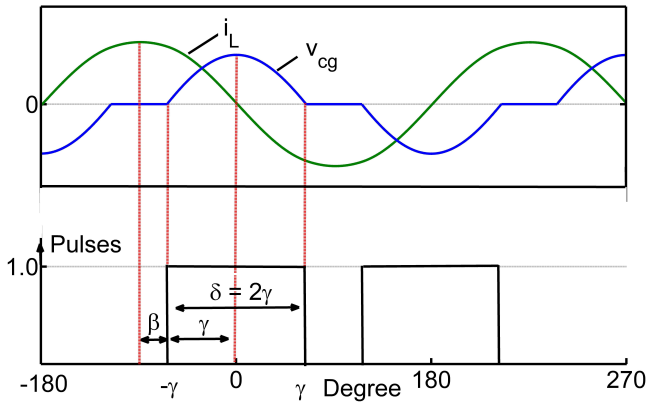

Figure 4.2: Line current $i_L(t)$, capacitor voltage $v_{cg}(t)$, and switching function of the GCSC. β = GCSC's turn-off angle γ = the angle of the advance $(\pi/2 - \beta)$, δ = hold off angle $(\pi - 2\beta = 2\gamma)$

capacitance of the GCSC. As δ changes from 0^o to 180^o, X_G varies from 0 to X_{cg}.

The voltage across the GCSC contains odd harmonics, in addition to the fundamental components. The harmonic analysis of the GCSC and some methods to reduce the harmonic levels have already been studied in literature [37], [99], [100]. In [99], it has been shown that the maximum total harmonic distortion (THD) of the GCSC voltage, when a single GCSC module is used, is about 4.5%. However, in practice, multi-module GCSCs (MGCSC), which use smaller GCSC modules in series so that each module compensates part of the total required series compensation level, are used in order to obtain the required power rating for the GCSC. Using this configuration, the THD generated by the GCSC can be reduced down to 1.5% [99]. In this method, the voltage of each GCSC module still contains all the harmonic components of the single GCSC module, but with lower magnitude [37], [99], [100].

Another method for reducing harmonic levels in the GCSC voltage is using multi-pulse arrangements [99]. In this method, transformers are used to inject the GCSC voltage into the transmission line, and the transformers windings are connected in such a way that some lower order harmonics (LOH) of the GCSC voltage are canceled out. Using this method, the THD of the GCSC voltage could be reduced to less than 0.34%, which is an acceptable

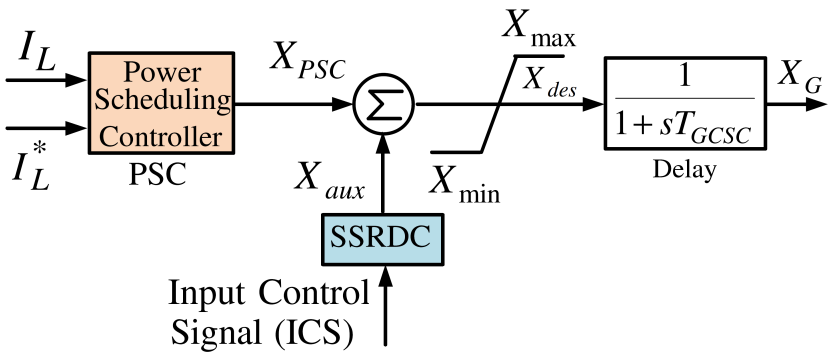

Figure 4.3: Block diagram of the GCSC controller.

level of THD level in high-voltage power systems and FACTS applications [99]. More details of the harmonic analysis of the GCSC can be found in [37], [99], [100].

GCSC Modeling and Control

The operation of the GCSC is modeled as a variable capacitor. It is assumed that the desired value of the GCSC reactance is implemented within a well defined time frame, i.e. a delay. The delay can be modeled by a first order lag as shown in Figure 4.3, which will add one more order to the system. In Figure 4.3, X_{PSC} is determined by the power scheduling controller (PSC). In [28], [30] a power controller has been used for the GCSC to damp SSR and power oscillation; however, as shown later, this power controller may not be adequate to damp the SSR. Therefore, an auxiliary SSRDC, as shown in Figure 4.3 should be added to the GCSC controller to enable it to damp the SSR.

Power Scheduling Controller (PSC)

The block diagram of the GCSC's PSC control is shown in Figure 4.4. In this figure, T_m is the time constant of first order low pass filter associated with the measurement of the line current. In this controller, the measured line current I_m is compared to a reference current I_L^*, and the error ΔI is passed through a lead controller and a proportional-integral (PI) regulator.

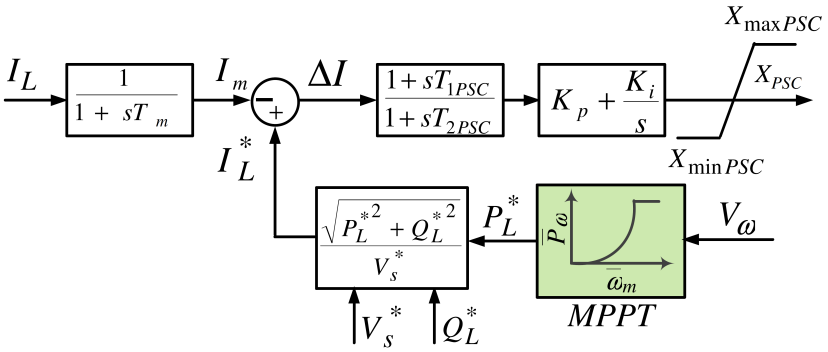

Figure 4.4: Block diagram of the GCSC power scheduling controller (PSC).

The MPPT curve and the chosen reactive power control strategy for the transmission line, i.e., fixed Var flow or fixed power factor, are used to obtain the I_L^*. If the power losses are ignored, the optimum input wind power $\bar{P_\omega}$, which can be obtained using MPPT curve for different wind speeds, is equal to the desired delivered real power to the transmission line, P_L^* in $(p.u.)$. Also, depending on the chosen reactive power control strategy for the transmission line, i.e. fixed Var flow or fixed power factor, the desired reactive power of the transmission line, i.e. Q_L^* $(p.u.)$, can be determined. Then, the transmission line reference line current can be calculated as follows:

$$I_L^* = \frac{\sqrt{P_L^{*2} + Q_L^{*2}}}{V_s^*} \tag{4.2}$$

A modal analysis at different operating points of the wind farm is performed when the GCSC model with PSC is added to the system. Figure 4.5 compares the real part of the Mode 1 and 2 at different compensation levels and different wind speeds for two cases: a) when the DFIG wind farm is compensated only with a series fixed capacitor b) when the DFIG wind farm is compensated with a GCSC without SSRDC and only with a PSC. As seen in this figure, using only the PSC in GCSC not only does not enable this device to stabilize the Mode 1, but also it decreases the damping of Mode 1. This shows that an auxiliary SSRDC is needed to enable the GCSC to damp the SSR.

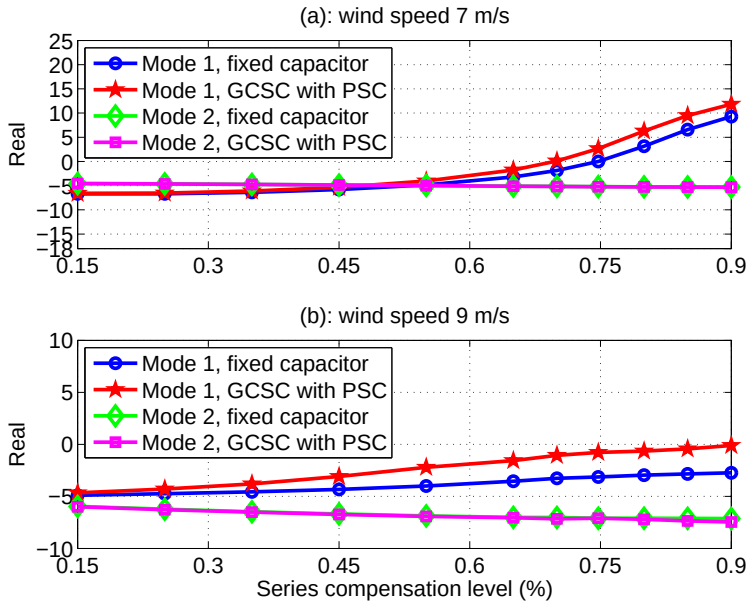

Figure 4.5: Real part of Mode 1 and 2 when wind speed is (a) 7 m/s (b) 9 m/s with GCSC and fixed capacitor in line.

Sub-Synchronous Resonance Damping Controller (SSRDC)

In order to enhance the SSR damping, an auxiliary controller is added to the GCSC control system with an appropriate input control signal (ICS), as shown in Figure 4.3. The question is how an appropriate ICS should be selected. This question is answered in the following sections.

4.2 ICS Selection and SSRDC Design

ICS Selection Using Residues

The residues corresponding to SSR and SupSR modes for different ICSs are computed. If the state-space model and transfer function of the single-input single-output are defined as [68]:

$$\dot{X} = AX + BU \tag{4.3}$$

$$Y = CX \tag{4.4}$$

$$G(s) = C(SI - A)^{-1}B = \frac{Y(s)}{U(s)} = \sum_{i=1}^{n} \frac{R_i}{s - \lambda_i} \tag{4.5}$$

Then for a complex root λ_i, the residue R_i is a complex number, which can be considered as a vector having a certain direction, and can be expressed as [68]:

$$R_i = C\Psi_i\Phi_i B \tag{4.6}$$

In a root locus diagram, R_i is representation of the direction and speed of the closed loop eigenvalue λ_{ci} which leaves the pole λ_i. The effect of the residues in selecting ICS can be described as follows. Suppose that dynamics of all eigenvalues are ignored, except one specific eigenvalue λ_a. This means that the open-loop transfer function of the system has only one pole, which can be represented as:

$$G_a(s) = \frac{R_a}{s - \lambda_a} \tag{4.7}$$

Using Eq. 4.7, the closed-loop system with a gain controller, K_{gc}, is represented as follows:

$$G_{ca}(s) = \frac{G_a(s)}{1 + K_{gc}G_a(s))} = \frac{R_a}{s - \lambda_a + K_{gc}R_a} \tag{4.8}$$

Finally, using Eq. 4.8 the root of the closed-loop and the shift in the eigenvalues, i.e. $\Delta\lambda_{sh}$, can be represented using Eqs. 4.9 and 4.10, as follows:

$$\lambda_{ca} = \lambda_a - K_{gc}R_a \tag{4.9}$$

$$\Delta\lambda_{sh} = -K_{gc}R_a \tag{4.10}$$

Eq. 4.10 shows that the residue influences the closed-loop system root, by determining the direction and speed of it. If the magnitude of the residue is large enough, then a smaller gain is needed for the feedback control system.

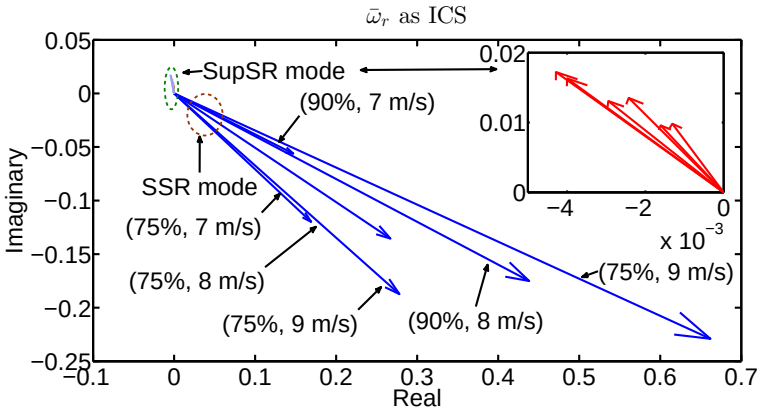

Figure 4.6: Residues of the SSR mode with $\bar{\omega}_r$ as ICS.

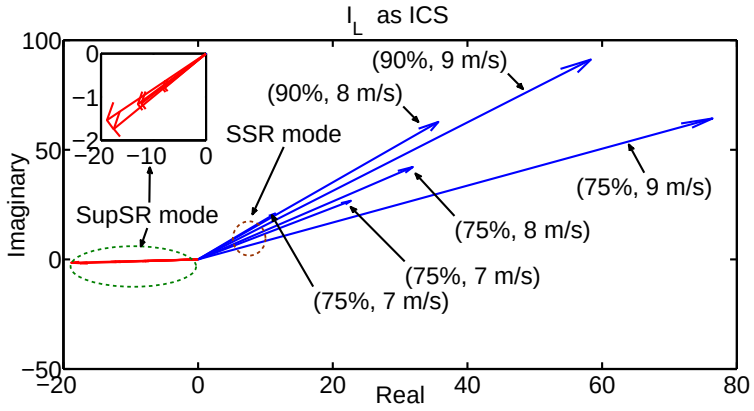

Figure 4.7: Residues of the SSR mode with I_L as ICS.

Figure 4.6 through Figure 4.8 show the residues of the SSR and SupSR modes at different operating conditions of the wind farm, when $\bar{\omega}_r$, I_L, and V_{cg} are used as ICS. Figure 4.6 shows that when $\bar{\omega}_r$ is selected as ICS, the residue magnitude of the SSR mode is small. Therefore, if this signal is being used as ICS, a larger gain will be needed for the feedback control. In addition, as Figure 4.6 shows, the residues of the SSR and SupSR modes are in an opposite direction, which will increase the difficulty of the controller design. The reason is that a simple proportional controller chosen to increase damping of the SSR mode will decrease the damping of the SupSR mode, verifying that $\bar{\omega}_r$ is not an optimum choice for ICS. Therefore, this signal will not be further considered.

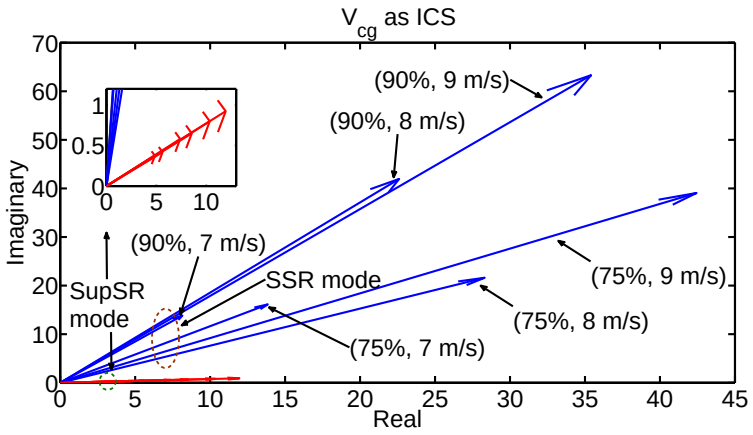

Figure 4.8: Residues of the SSR mode with V_{cg} as ICS.

Figure 4.7 shows that when I_L is selected as ICS, the residue magnitude of the SSR mode is rather large, and therefore, a smaller feedback gain is needed to stabilize the SSR mode. However, since the residues of the SSR and SupSR modes in this case point in opposite directions, stabilizing the SSR mode via a feedback gain will decrease the SupSR mode damping. This shows that the line current may not be an optimum parameter as ICS. This signal as ICS will be further analyzed in the next section

Finally, Figure 4.8 shows the residue of the SSR and SupSR modes, when V_{cg} is selected as a ICS. This figure exhibits two facts: first, it shows that the SSR and SupSR modes are in the same direction; second, the magnitude of the residues are large enough. These properties will make the design of the feedback control simple so that a small gain will be enough to force both the SSR and SupSR modes to move to the left and make the system stable. In the next sections, both I_L and V_{cg} are studied in more detail as two potential ICSs.

Root Locus Analysis

The analysis presented by residue-based method is verified using root locus analysis. As represented in Figure 4.9 for I_L as ICS, when the gain increases, the SSR and SupSR modes will move in opposite direction, as we expected from residues analysis. In addition, the maximum damping ratio for SSR mode is obtained 3%, and the corresponding gain in

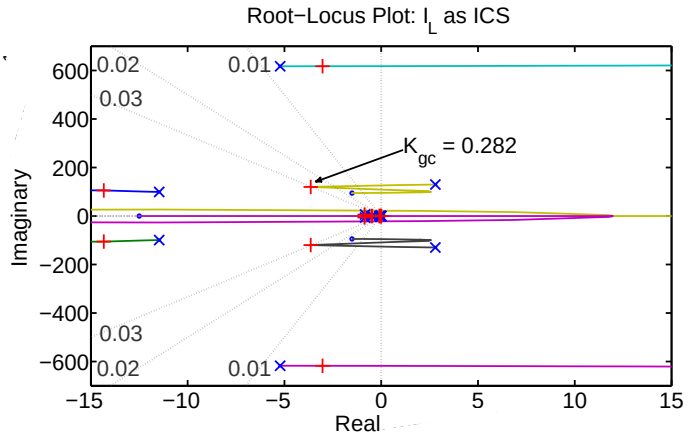

Figure 4.9: Root locus diagram of the SSR mode with I_L as ICS. The + sign indicates the locations of the roots corresponding to the indicated gain, K_{gc}.

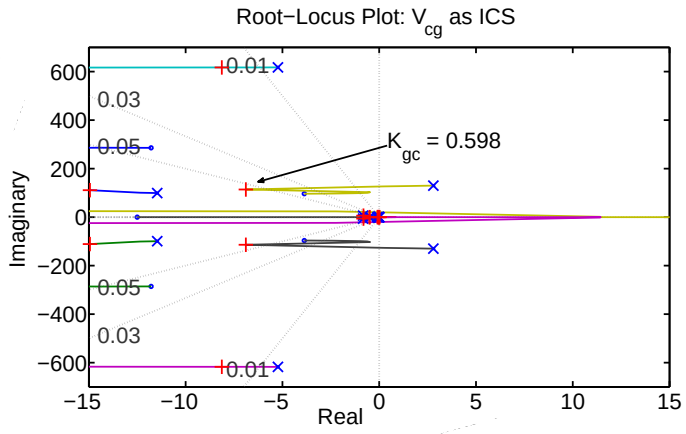

Figure 4.10: Root locus diagram of the SSR mode with V_{cg} as ICS. The + sign indicates the locations of the roots corresponding to the indicated gain, K_{gc}.

this case is about 0.282, as indicated in Figure 4.9. For this gain, the corresponding SupSR mode will move toward the right hand side of the root locus diagram, but will not pass the imaginary axis, and the system is still stable.

Figure 4.10 represent the root locus diagram of the system when V_{cg} is as ICS. This figure shows that when the gain increases, both the SSR and SupSR modes move to the left hand side of the root locus plane. In this case, in order to have 5% damping ratio for SSR mode, the gain is computed 0.598, as indicated in Figure 4.10. For this gain, the corresponding SupSR mode will move toward the left hand side of the root locus diagram and become more stable.

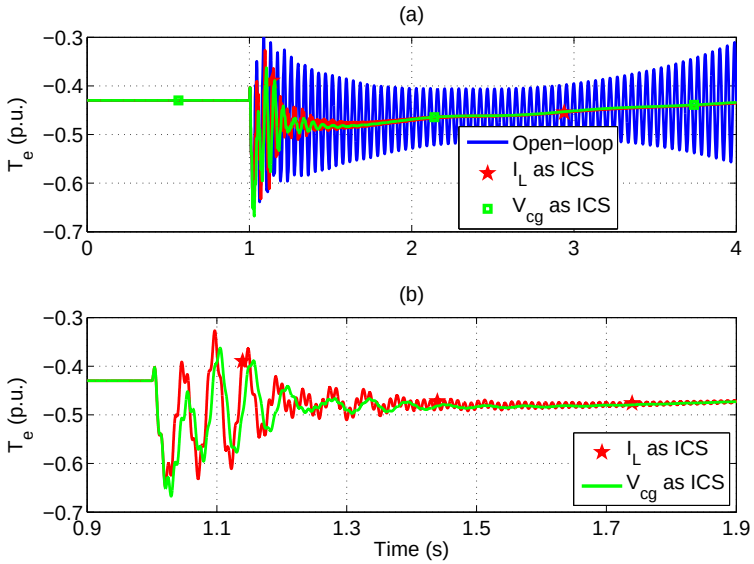

Figure 4.11: Comparing dynamic response of the electric torque without SSRDC and with SSRDC (I_L and V_{cg} as ICS) (a) simulation time from $t = 0$ s to $t = 4$ s (b) simulation time from $t = 0.9$ s to $t = 1.9$ s.

In conclusion, root locus diagram and residues analysis results presented in Section 4.2 show that both I_L and V_{cg} could be used as ICS; however, using the latter, a larger damping ratio can be obtained, and also, both the SSR and SupSR modes can be stabilized simultaneously by use of the proposed procedure.

4.3 Time Domain Simulation of GCSC Compensated DFIG

In this section, the time domain simulation of the DFIG wind farm is presented to verify the analysis presented in Section 4.2. The system is simulated for different scenarios, namely, the wind farm compensated by the GCSC with no SSRDC (open-loop), the wind farm compensated by the GCSC and I_L as ICS to the SSRDC (I_L as ICS), and the wind farm compensated by the GCSC and V_{cg} as ICS to the SSRDC (V_{cg} as ICS). In the simulation study, initially, the compensation level is regulated at 50% and then at $t = 1$ s, the compensation level is changed to 75%. The dynamic responses of the wind farm including electric torque T_e, terminal voltage V_s, and DC link voltage V_{DC} are plotted in Figure 4.11

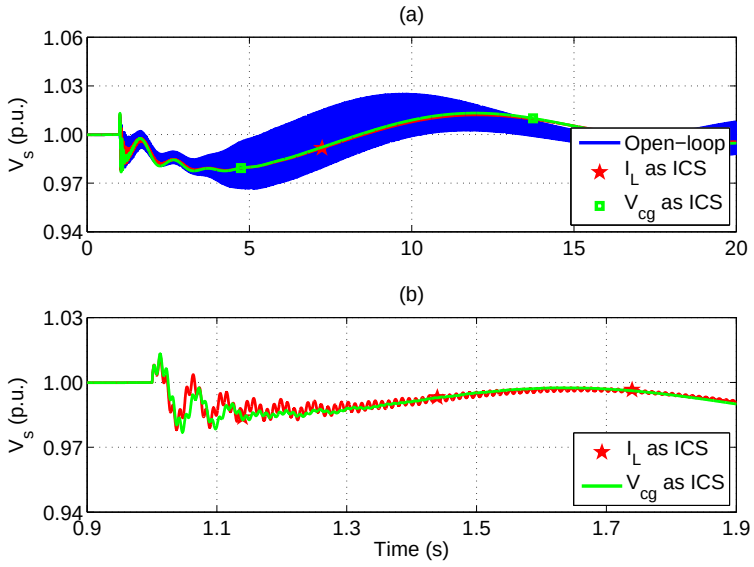

Figure 4.12: Comparing dynamic response of the terminal voltage without SSRDC and with (I_L and V_{cg} as ICS) (a) simulation time from $t = 0$ s to $t = 20$ s (b) simulation time from $t = 0.9$ s to $t = 1.9$ s.

through Figure 4.13, respectively.

Figure 4.11 shows the electric torque T_e of the system for three cases. As Figure 4.11. (a) shows, the wind farm is unstable due to the SSR mode when the GCSC is not equipped with SSRDC. The wind farm equipped by the GCSC and SSRDC with either I_L or V_{cg} as ICSs can effectively damp out the SSR mode and stabilize the system. Figure 4.11. (b) shows that when V_{cg} is used as ICS, both SSR and SupSR modes are mitigated faster compared to the case when I_L is used as ICS. This confirms the analysis presented in Section 4.2 that using I_L as ICS decreases the damping of the SupSR mode, and that the maximum damping ratio for the SSR mode is limited to less than 3%. A similar behavior can be observed using Figure 4.12 Figure 4.13, where the terminal voltage V_s and DC link voltage V_{DC} are plotted, respectively.

Finally, in order to show that the control system guarantees the unity power factor, Figure 4.14 compares the power factor of the system when I_L or V_{cg} are used as ICS. As seen in this figure, the control system is able to maintain the unity power factor for the wind farm using both ISCs. Once again, using V_{cg} as ICS provides better SSR and SupSR

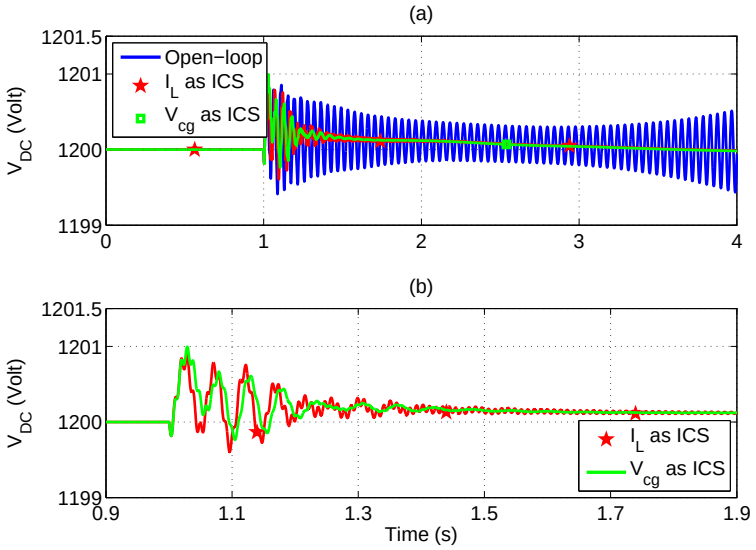

Figure 4.13: Comparing dynamic response of the DC link voltage without SSRDC and with SSRDC (I_L and V_{cg} as ICS) (a) simulation time from $t = 0$ *s* to $t = 20$ *s* (b) simulation time from $t = 0.9$ *s* to $t = 1.9$ *s*

damping for the system compared to when I_L is used as ICS.

4.4 SUMMARY

This chapter has proposed application, modeling, and control of the gate-controlled series capacitor, a series FACTS device, for transmission line compensation and SSR mitigation in DFIG-based wind farms using modal analysis. In order to stabilize the SSR mode, a series FACTS device, i.e. GCSC, replaces with the fixed series capacitor. Using residue-based analysis, three different signals namely, generator rotor speed $\bar{\omega}_r$, line current I_L, and voltage across the GCSC V_{cg} are examined in order to find the optimal input control signal (ICS) to the GCSC's SSR damping controller (SSRDC).

The residue-based analysis shows that the rotor speed is not an optimum ICS for the SSRDC for two reasons: first, a very large gain is needed in this case, and second, it is not possible to simultaneously increase the damping of both SSR and SupSR modes. Also, even though the residue-based analysis for the line current as ICS predicts that a smaller gain is needed to damp the SSR mode, the SupSR mode's stability is decreased in this case,

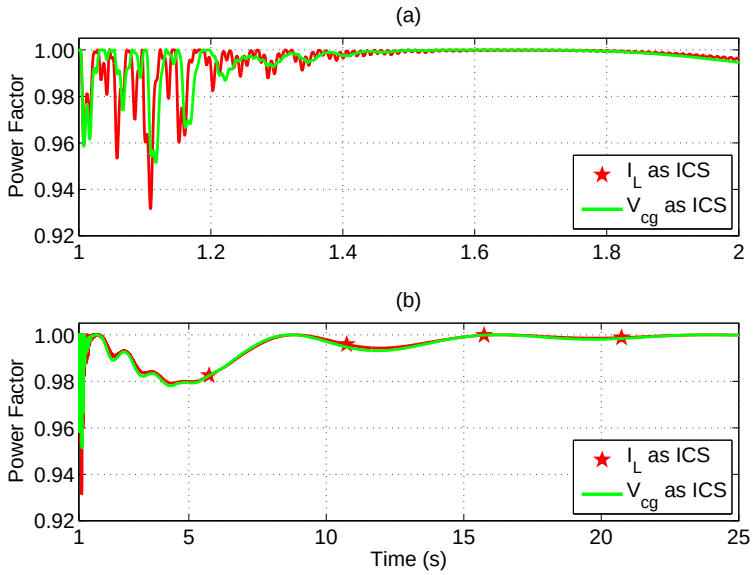

Figure 4.14: Power factor of the DFIG wind farm (a) simulation time from $t = 1$ *s* to $t = 2$ *s* (b) simulation time from $t = 1$ *s* to $t = 25$ *s*

indicating that this signal may not be an optimum ICS. The residue-based analysis for the voltage across the GCSC, however, predicts that this signal can increase the stability of both the SSR ans SupSR modes, simultaneously.

In addition, using root-locus diagrams, the required gain to damp the SSR mode is computed for both line current and voltage across the GCSC as ICSs. The results show that, unlike the line current as ICS, using voltage across the series capacitor as ICS can guarantee the damping of the SSR mode- without sacrificing the SupSR mode's stability- verifying what was expected from the residue-based analysis. Also, the maximum SSR damping ratio, when the voltage across the GCSC is used as ICS, is 67% more compared to that of the line current. Finally, time-domain simulation is used to verify the design process using residue-based analysis and root-locus diagrams.

CHAPTER 5

SSR DAMPING USING THYRISTOR - CONTROLLED SERIES CAPACITOR (TCSC)

In this chapter, the thyristor-controlled series capacitor (TCSC) is used for series compensation and sub-synchronous resonance (SSR) damping in doubly-fed induction generator (DFIG)-based wind farms. The SSR damping capability of this device is examined using eigenvalue analysis, performed in MATLAB/SIMULINK, and time-domain simulations, performed in PSCAD/EMTDC.

5.1 THYRISTOR-CONTROLLED SERIES CAPACITOR

In the TCSC, by controlling the firing angle α of the thyristors, the parallel LC filter can be tuned, making the impedance of the TCSC controllable. Figure 5.1 shows the single line configuration of a TCSC which can be applied to each of the three phases. Figure 5.2 shows typical waveforms of the TCSC including line, capacitor and thyristor currents ($i_L(t)$, $i_{CT}(t)$ and $i_{LT}(t)$), capacitor voltage (v_{CT}), and corresponding firing pulses (T_1 and T_2).

In the TCSC, if the value of the reactor, X_{LT}, is sufficiently smaller than that of capacitor, X_{CT}, the TCSC can operate in on-off manner so that by changing its firing angle, α, the inductance of the thyristor-controlled reactor (TCR) can be changed. This enables the TCSC to provide a continuously variable capacitor by canceling part of the X_{CT} impedance using the variable inductor, i.e. TCR [24]. Typically, the value of X_L is chosen to be 10% to 30% of the value of the X_{CT} [24].

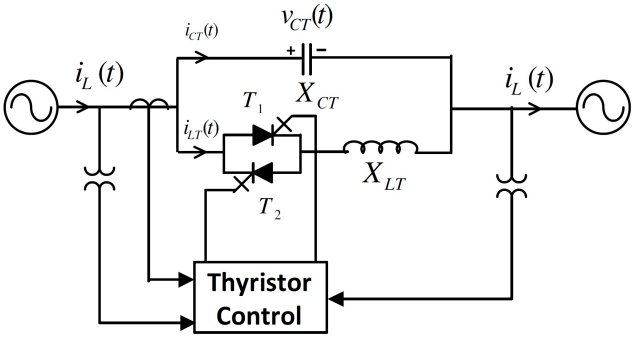

Figure 5.1: Typical single line configuration of a TCSC.

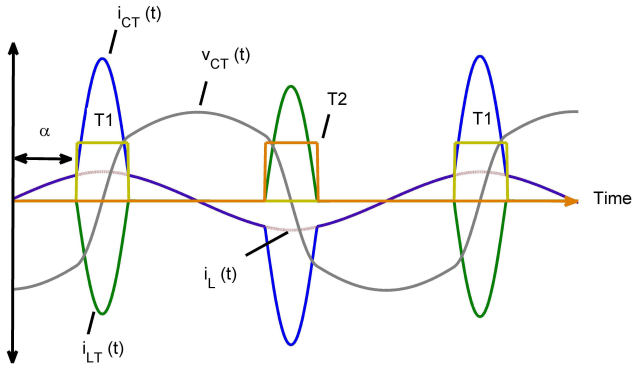

Figure 5.2: TCSC capacitor voltage ($v_{CT}(t)$), line current ($i_L(t)$), capacitor and inductor currents ($i_{CT}(t)$ and $i_{LT}(t)$), and TCSC switching pulses (T_1 and T_2).

Figure 5.3 shows typical impedance of the TCSC in terms of firing angle (α). As seen in this figure, since the TCSC actually represents a tunable parallel LC circuit, in a normal TCSC structure, in which the value of X_{LT} is smaller than that of the capacitor X_{CT}, the TCSC has two operating ranges around its parallel resonance area namely inductive and capacitive, as shown in Figure 5.3. Care must be taken, in order to avoid the resonance area.

Modeling of TCSC for SSR Analysis

For the SSR studies, the TCSC is modeled as a variable inductive reactance in parallel with a fixed capacitor, as shown in Figure 5.4. From this figure, the inductive reactance of the TCSC can be obtained as follows:

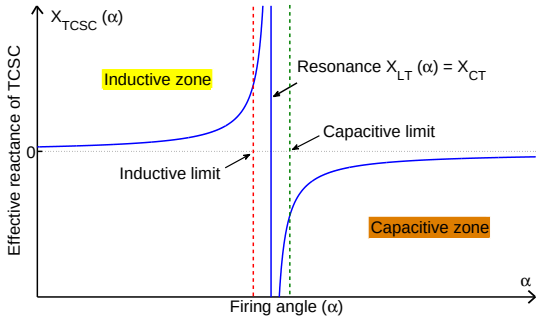

Figure 5.3: TCSC reactance versus firing angle.

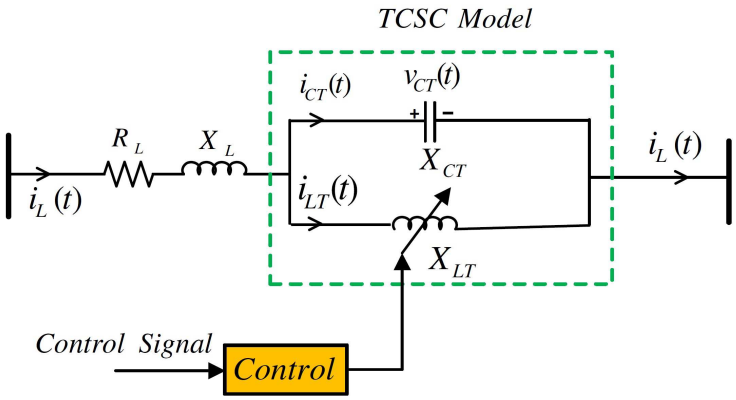

Figure 5.4: Single line diagram of the transmission line and TCSC model.

$$\frac{1}{X_{LT}(\alpha)} = \frac{1}{X_{CT}} - \frac{1}{X_{TCSC}(\alpha)} \tag{5.1}$$

where $X_{TCSC}(\alpha)$ is th desired value of the series compensation provided by the TCSC.

In Chapter 2, we provided the modeling of the DFIG in qd-frame. In this chapter, the DFIG modeling is updated by adding the modeling of the TCSC to the system. The qd-frame circuit of the TCSC including the transmission line is given in Figure 5.5 and Figure 5.6. Performing KVL and KCL in Figure 5.5 and Figure 5.6, one can get the state-space representation of the transmission line compensated by the TCSC as follows:

$$\dot{X}_{Tline} = A_{Tline}X_{Tline} + B_{Tline}U_{Tline} \tag{5.2}$$

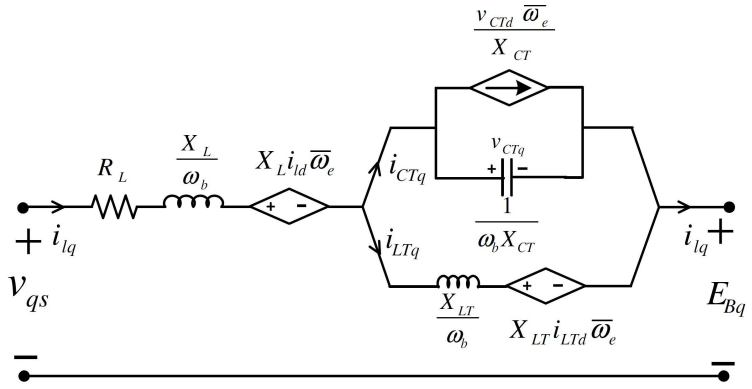

Figure 5.5: Transmission line and the TCSC model in q-axis.

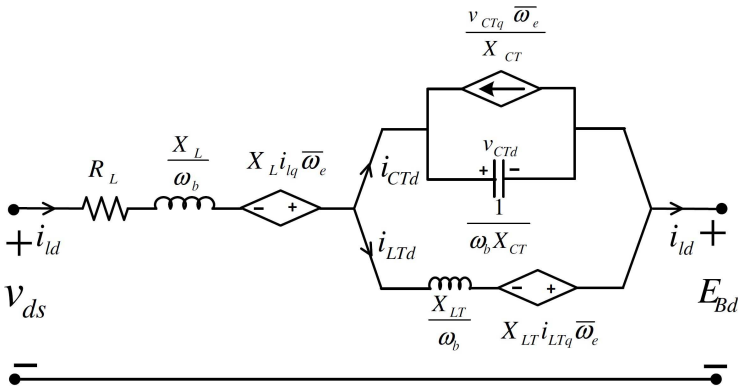

Figure 5.6: Transmission line and the TCSC model in d-axis.

$$X_{Tline} = [i_{lq}\ i_{ld}\ v_{CTq}\ v_{CTd}\ i_{LTq}\ i_{LTd}]^T \tag{5.3}$$

$$U_{Tline} = [\frac{(v_{qs} - E_{Bq})}{X_L}\ \ \frac{(v_{ds} - E_{Bd})}{X_L}\ \ 0\ \ 0\ \ 0\ \ 0]^T \tag{5.4}$$

where i_{lq} and i_{ld} are the transmission line qd-axis currents $(p.u.)$, v_{CTq} and v_{CTd} are the TCSC qd-axis voltages $(p.u.)$, and i_{LTq} and i_{LTd} are the TCSC inductor qd-axis currents $(p.u.)$.

The A_{Tline} and B_{Tline} matrices are defined as follows:

$$A_{Tline} = \begin{bmatrix} \frac{-R_L}{X_L} & -\bar{\omega}_e & \frac{-1}{X_L} & 0 & 0 & 0 \\ \bar{\omega}_e & \frac{-R_L}{X_L} & 0 & \frac{-1}{X_L} & 0 & 0 \\ X_{CT} & 0 & 0 & -\bar{\omega}_e & -X_{CT} & 0 \\ 0 & X_{CT} & \bar{\omega}_e & 0 & 0 & -X_{CT} \\ 0 & 0 & \frac{1}{X_{LT}} & 0 & 0 & -\bar{\omega}_e \\ 0 & 0 & 0 & \frac{1}{X_{LT}} & \bar{\omega}_e & 0 \end{bmatrix} \tag{5.5}$$

$$B_{Tline} = \begin{bmatrix} \omega_b & 0 & 0 & 0 & 0 & 0 \\ 0 & \omega_b & 0 & 0 & 0 & 0 \\ 0 & 0 & 1 & 0 & 0 & 0 \\ 0 & 0 & 0 & 1 & 0 & 0 \\ 0 & 0 & 0 & 0 & 1 & 0 \\ 0 & 0 & 0 & 0 & 0 & 1 \end{bmatrix} \tag{5.6}$$

where R_L is the transmission line resistance $(p.u.)$, X_L is the transmission line reactance $(p.u.)$, X_{CT} is the fixed series capacitor reactance of the TCSC $(p.u.)$, X_{LT} is the variable inductive reactance of the TCSC $(p.u.)$ that is controlled by the TCSC control loop, E_{Bq} and E_{Bd} are the infinite bus qd-axis voltages $(p.u.)$, and $\bar{\omega}_e$ is the rotating synchronous frame frequency $(p.u.)$.

Control of TCSC

The basic control structure of the TCSC is shown in Figure 5.7. The main part of the TCSC control includes power scheduling control (PSC) and SSR damping controller (SSRDC). Moreover, for the SSR studies, modeling of the gate unit is not required, and it is adequate

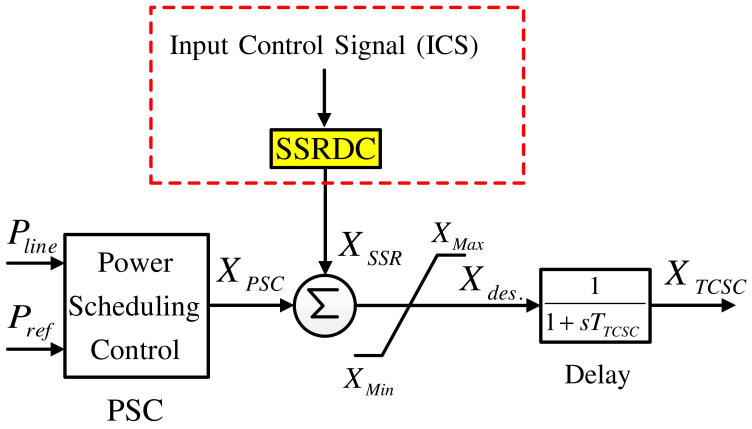

Figure 5.7: Block diagram of TCSC control.

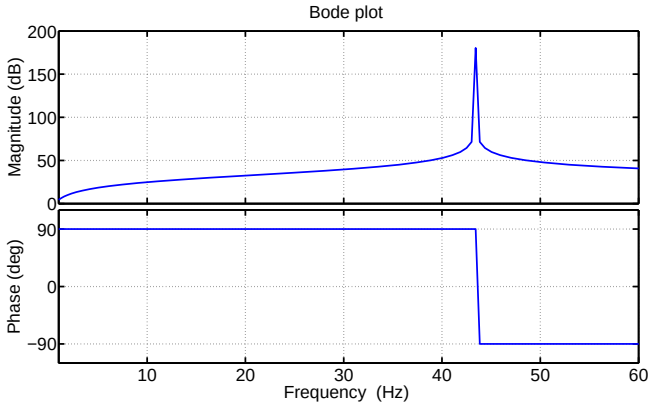

Figure 5.8: Bode plot of the TCSC reactance when $X_{TCSC} = = 2.2 \cdot X_{CT}$.

to assume that the desired value of the TCSC reactance is provided to the line within a well-defined time frame, which can be modeled by a first order lag, as seen in Figure 5.7. The value of T_{TCSC} is chosen to be 10 *ms*. The PSC block diagram is based on a constant power control, in which the measured line power is compared to a reference real power, which can be derived from the load flow information. The PSC control is of PI type with dynamic compensation for improving the system response.

The control of the TCSC shown in Figure 5.7 also includes a SSRDC. However, the TCSC can damp the SSR even without a SSRDC. The reason is that as seen in Figure 5.8, where the Bode plot of the TCSC reactance is shown for $X_{TCSC} = 2.2 \cdot X_{CT}$ and compen-

Table 5.1: Comparing the SSR mode of the system with FSC and TCSC when V_ω = 7 m/s and compensation level changes.

K (%)	FSC	TCSC
50	-1.8784 ± j140.7799	-1.5404 ± j58.2021
55	**+1.2126** ± j128.5545	-1.2710 ± j54.5403
60	**+5.9289** ± j118.8507	-0.9751 ± j50.9856
65	**+9.6991** ± j112.3237	-0.6533 ± j47.5521

Table 5.2: Comparing the SupSR mode of the system with FSC and TCSC when V_ω = 7 m/s and compensation level changes.

K (%)	FSC	TCSC
50	-5.1561 ± j608.9960	-1.3487 ± j696.3008
55	-5.2253 ± j620.39633	-1.4604 ± j700.1166
60	-5.2812 ± j631.2477	-1.5634 ± j703.8734
65	-5.3158 ± j641.5941	-1.6542 ± j707.5644

sation level is 60%, the TCSC is capacitive at 60 Hz, but exhibits inductive behavior at the lower SSR frequencies. This means that for the same compensation level, the FSC may exhibit a resonance at SSR frequencies, when the FSC capacitive impedance cancels the transmission line inductive impedance, but the TCSC may not, because the TCSC impedance is inductive at SSR frequencies. In the next section, using eigenvalue analysis, it is investigated whether or not the TCSC needs a SSRDC to damp the SSR.

Eigenvalue Analysis of the System with TCSC

In this paper, the TCSC operates at $X_{TCSC} = 2.2 \cdot X_{CT}$. Table 5.1 and 5.2 compare the SSR and SupSR modes of the system with FSC and TCSC, when V_ω = 7 m/s and compensation level changes from 50% to 65%. As seen in Table 5.1, for the same compensation level, the SSR frequencies are lower with the TCSC compared to FSC, meaning that the resonance frequency decreases for the same compensation level. Additionally, Table 5.1 shows that the TCSC is able to damp the SSR mode, even without the SSRDC, whereas the FSC has an unstable SSR mode with positive real part for compensation levels of 55% or larger. However, as seen in this table, the damping ratio of the SSR mode with TCSC is not

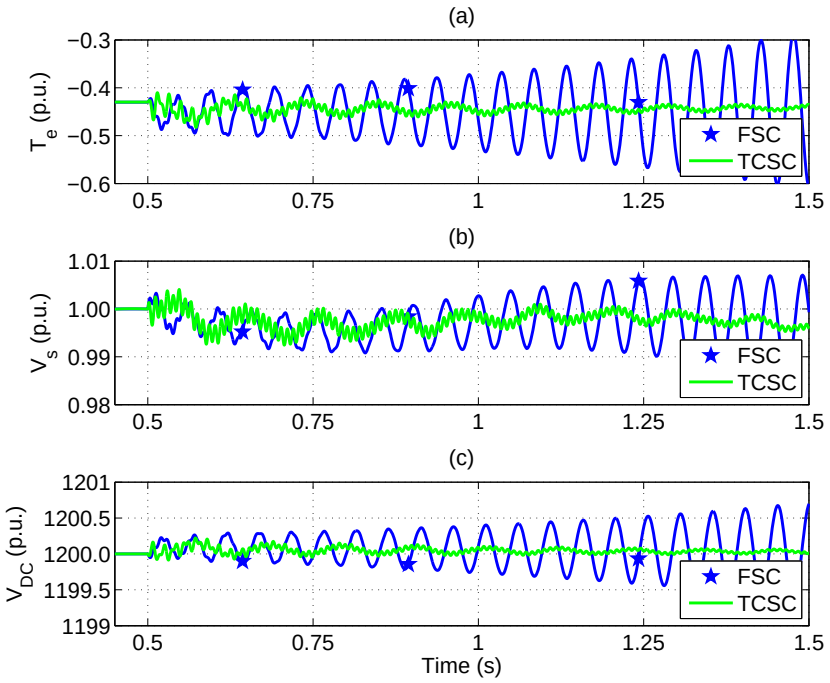

Figure 5.9: Dynamic response of the system with FSC and TCSC: (a) electric torque (b) terminal voltage (c) DC-link voltage.

large. Therefore, if larger damping ratio for the SSR mode is required, a SSRDC should be designed for the TCSC. On the contrary, Table 5.2 shows that, compared to the FSC, using TCSC decreases the stability of the SupSR mode.

Time-Domain Simulation

Time-domain simulation of the TCSC - compensated DFIG is presented in this section. In the simulations, initially the compensation level is regulated at 50%, at which the system is stable, and then at $t = 0.5\ s$, the compensation level is increased to 55%, which causes instability because of the SSR mode in FSC. Figure 5.9 shows the dynamic performance of the system including electric torque T_e, terminal voltage V_s, and DC link voltage V_{DC}. As seen in this figure, the TCSC has successfully damped the SSR mode and has stabilized the wind farm. However, as seen in Figure 5.9, damping time of the super-synchronous mode is much longer with the TCSC compared to FSC. The reason is that using the TCSC, the

damping ratio of the SupSR mode decreases compared to the FSC, as observed in Table 5.2.

5.2 SUMMARY

In this chapter the application of the TCSC for SSR damping in DFIG based winf farms has been studied. Based on the discussions presented in the paper, the following conclusions can be drawn:

1. The TCSC is able to damp the SSIGE, even without a SSRDC. However, when using TCSC, the damping ratio of the SupSR mode decreases compared to FSC.

2. If relatively large values of SSR and SupSR damping ratio are required, a SSRDC must be added to the TCSC controller.

CHAPTER 6

SSR DAMPING USING DFIG CONVERTERS

This chapter deals with sub-synchronous resonance (SSR) damping using the rotor-side converter (RSC) and grid-side converter (GSC) controllers of the DFIG. The objective is to design a simple proportional SSR damping controller (SSRDC) by properly choosing an optimum input control signal (ICS) to the SSRDC block so that the SSR mode becomes stable without decreasing or destabilizing the other system modes. Moreover, an optimum point within the RSC and GSC controllers to insert the SSRDC is identified. Three different signals are tested as potential ICSs including rotor speed, line real power, and voltage across the series capacitor, and an optimum ICS is identified using residue-based analysis and root-locus method. Moreover, two methods are discussed in order to estimate the optimum ICS, without measuring it directly. Matlab/Simulink is used as a tool for modeling and design of the SSRDC, and PSCAD/EMTDC is used to perform time-domain simulation for design process validation.

6.1 DFIG CONVERTER CONTROLLERS

The SSR damping is achieved using an additional SSR damping controller (SSRDC) on either the GSC or RSC, operating on a single input control signal (ICS) as illustrated in Figure 6.1 and Figure 6.2. The SSRDC block is represented in Figure 6.3, which is based on proportional gain K_{SSR} and washout filter. The value of the K_{SSR} for each ICS is obtained using root-locus method such that 6% damping ratio is obtained for the SSR mode. The 6% damping ratio is chosen arbitrarily, but the procedure can be used for any desired value of damping ratio. Moreover, a washout filter, which is a high pass filter, is included in the

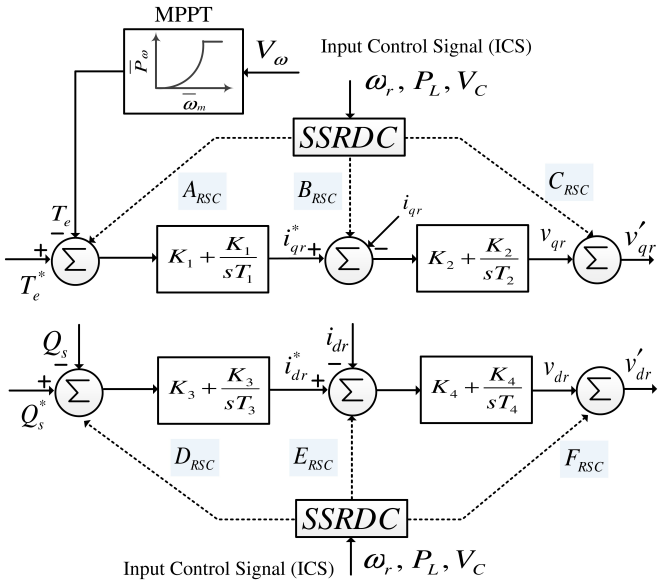

Figure 6.1: RSC controllers

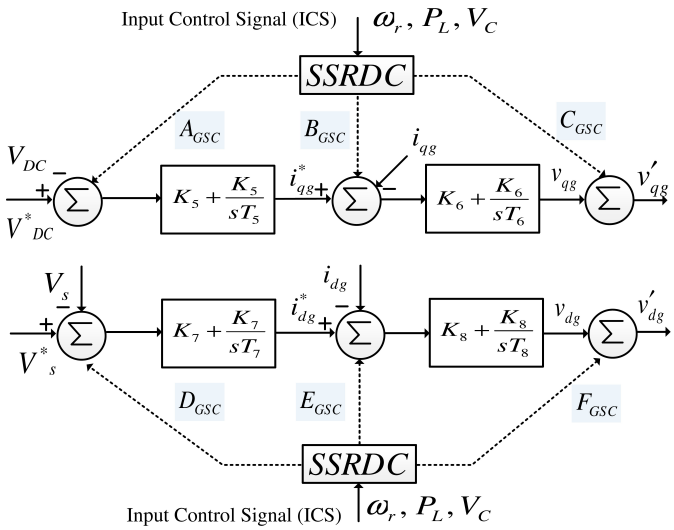

Figure 6.2: GSC controllers

SSRDC block to eliminate the effect of the SSRDC on the steady-state operating condition. Usually the value of the washout filter time constant T_w is chosen to be between 5 to 10 sec. In this work, $T_w = 5\ sec$. [68].

There are a variety of options for the ICS, as shown in Figure 6.1 and Figure 6.2. In this work, rotor speed ω_r, transmission line real power P_L, and voltage across the series

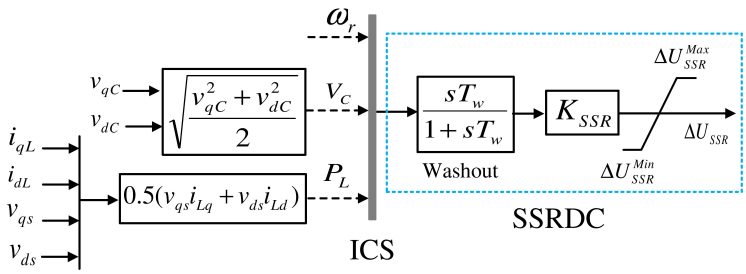

Figure 6.3: SSR damping controller block diagram.

compensation V_C are examined, and the optimum ICS is identified with the help of residue-based analysis and root-locus diagrams, as explained in the next section.

6.2 ICS AND CONVERTER SELECTION FOR SSRDC DESIGN

In this section, using residue-based analysis and root-locus method, an optimum input control signal (ICS) to the SSRDC is introduced. The optimum ICS should enable the SSRDC to damp the SSR without decreasing or destabilizing the other system modes. The SSRDC can be inserted at different points of the RSC and GSC controllers, identified as A_{RSC}-F_{RSC} and A_{GSC}-F_{GSC} in Figure 6.1 and Figure 6.2. These insertion points are examined to find out where the SSRDC could be introduced.

Controllability

The concept of controllability play an important role in the design of control systems in state-space. In a controllable system, it is possible to transfer the system at time t_0 from any initial state X_{t0} to any other state using an unconstrained control vector in a finite interval of time.

Consider the state-space equations for a n^{th}-order linearized system, as follows:

$$\dot{X} = AX + BU \tag{6.1}$$

This system is completely state controllable, if the matrix given in Eq. 6.2 is of rank n [101].

$$Co = [B \ AB \ \ldots \ A^{n-1}B] \tag{6.2}$$

where Co is called the controllability matrix.

The controllability condition of the studied system in this work is tested, and the system is completely controllable.

The importance of system controllability in this work is explained as follows. The designed SSRDC is a simple proportional gain. Therefore, if the system is completely controllable, then the variations of the designed SSRDC gain, K_{SSR}, will affect all modes of the system. This means that while trying to make the SSR mode stable using the proportional SSRDC, this gain will influence other system modes by making them to move either to the right or to the left in the root-locus diagram.

Analysis of Rotor Speed (ω_r) as Input Control Signal

Table 6.1 (at the end of the current chapter) shows the residues of the SSR, SupSR, electro-mechanical, and shaft modes when ω_r is used as ICS and SSRDC is implemented at different points of the RSC and GSC controllers, identified in Figure 6.1 and Figure 6.2 as A_{RSC} - F_{RSC}, and A_{GSC} - F_{GSC}. From this Table, it is observed that with the SSRDC implemented at points A_{RSC}, B_{RSC}, D_{RSC} or A_{GSC}, a very large gain is needed to move the SSR mode from the right-half-plane (RHP) to the left-half-plane (LHP), since the magnitude of the SSR residues for these points is very small. Moreover, due to the opposing directions of these modes, at high gain the stability of other system modes may decrease or even destabilize the system.

These shortcomings are visualized using root-locus diagram shown in Figure 6.4, where SSRDC with ω_r as ICS is implemented at point A_{GSC}. Note that $\times$ and $+$ signs in the root-locus diagrams shown in this work indicate the open-loop and closed-loop system poles,

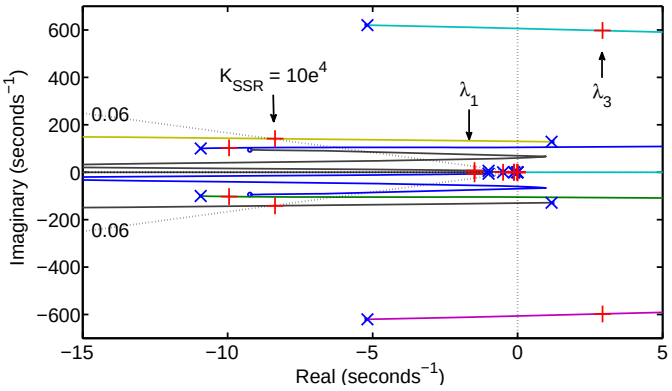

Figure 6.4: Root locus diagram with ω_r as ICS with SSRDC implemented in GSC controller at point A_{GSC}

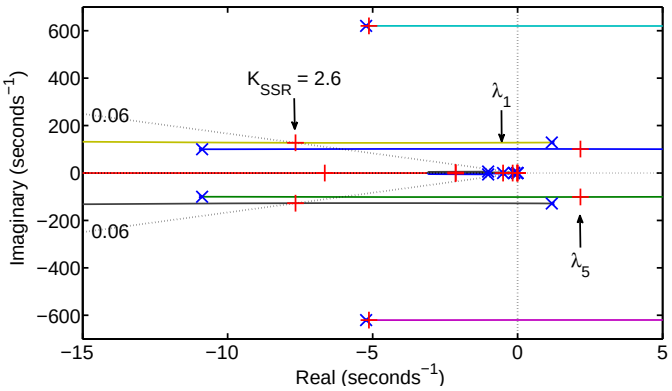

Figure 6.5: Root locus diagram with ω_r as ICS with SSRDC implemented in RSC controller at point F_{RSC}.

respectively. As seen in Figure 6.4, a very large SSR gain, i.e. $K_{SSR} = 10e^4$, can yield the desired 6% damping ratio for the SSR mode; however, the SupSR mode becomes unstable for this gain. Therefore, this signal cannot be used as ICS at points A_{RSC}, B_{RSC}, D_{RSC} or A_{GSC}.

Using ω_r as the ICS and placing the controller at the remaining points, the smaller gain necessary to stabilize the SSR mode still causes destabilization of the non-SSR modes. This occurs because the residues of the SSR mode do not have the same polarity as the residues of the other modes, as should be clear from Table 6.1. For example, at point C_{RSC},

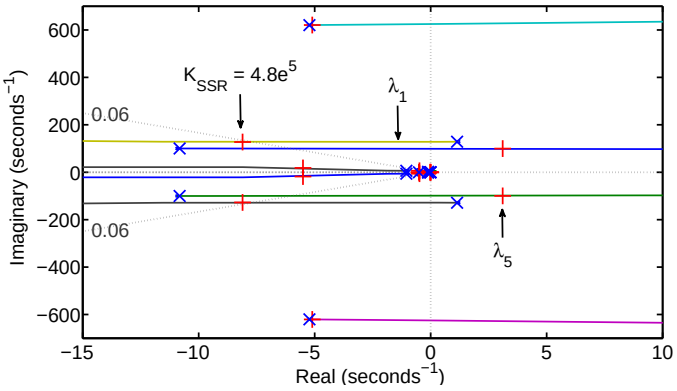

Figure 6.6: Root locus diagram with P_L as ICS with SSRDC implemented in RSC controller at point D_{RSC}.

the residue of the SSR mode has opposite polarity compared to all residues of the other modes given in Table 6.1. Conversely, when taking F_{RSC} as the control point, stabilizing the SSR mode will result in decreasing the stability of the SupSR mode and the electro-mechanical mode. The root locus for this control point, shown in Figure 6.5, shows that, as the SSR mode moves to the left and becomes stable, the SupSR and the electro-mechanical modes move to the right. In particular the electro-mechanical mode becomes unstable first, whereas the SupSR mode moves only by a small amount. This was to be expected given the larger amplitude of the electro-mechanical mode residue (4.5029) compared to the SupSR mode residue (0.0381).

Analysis of Transmission Line Real Power (P_L) as Input Control Signal

Table 6.2 ((at the end of the current chapter)) shows the residues of the SSR, SupSR, electro-mechanical, and shaft modes when P_L is used as ICS and the SSRDC is implemented at different points of RSC and GSC controllers. As seen in this Table, implementation of the SSRDC at points A_{RSC}, B_{RSC}, and D_{RSC} will require a very large gain to move the SSR mode from RHP to LHP since the magnitude of the SSR residues is very small. Moreover, even if this large gain is provided, the residues of the SSR mode are in opposite

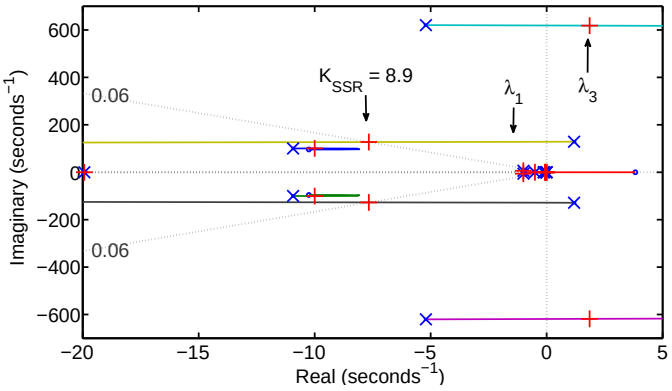

Figure 6.7: Root locus diagram with P_L as ICS with SSRDC implemented in GSC controller at point D_{GSC}.

direction with the residues of the SupSR, electro-mechanical, and shaft modes, and therefore, it is expected that with an increasing SSR gain, the other modes will move in opposite directions.

This is evident from the root locus diagram shown in Figure 6.6, where SSRDC with P_L as ICS is implemented at point D_{RSC}. As seen in this figure, although the SSR mode becomes stable with a very large gain, i.e. $K_{SSR} = 4.8e^5$, this makes the electro-mechanical mode unstable. Moreover, the SupSR mode has a tendency to move to the RHP with increasing the SSR gain. Therefore, this signal cannot be implemented as ICS at points A_{RSC}, B_{RSC}, and D_{RSC}.

For the other points of RSC and GSC controllers, i.e. C_{RSC} through F_{RSC} and A_{GSC} through F_{GSC}, if P_L is used as ICS, a smaller SSR gain will be needed to move the SSR mode from RHP to LHP, since the magnitude of the SSR residues are larger compared to the previous case. However, stabilizing the SSR mode in these cases will result in decreasing the stability, or even destabilizing, the other system modes. This is because, the residues of the SSR mode does not have the same polarity as the other modes, as shown in Table 6.2. For example, at point F_{RSC}, the residue of the SSR mode has opposite polarity compared to SupSR and electro-mechanical modes, as seen in Table 6.2.

As another example, with SSRDC implemented at point D_{GSC}, stabilizing the SSR mode deteriorates the stability of SupSR and electro-mechanical modes. Figure 6.7 represents the root-locus diagram of the system for this case. As shown in this figure, to have a 6% damping ratio for the SSR mode, a small SSR feedback gain, i.e. K_{SSR} = 8.9, is needed; however, this can result in destabilizing the SupSR mode. Therefore, regardless of the chosen insertion point for the SSRDC, the line real power P_L is not a good choice for ICS and should not be used.

Analysis of Capacitor Voltage (V_C) as Input Control Signal

Table 6.3 (at the end of the current chapter) shows the residues of the SSR, SupSR, electro-mechanical, and shaft modes when V_C is used as ICS and the SSRDC is implemented at different points of RSC and GSC controllers. As seen in this Table, implementation of the SSRDC at points A_{RSC}, B_{RSC}, and D_{RSC} will require a very large gain to move the SSR mode from RHP to LHP since the magnitude of the SSR residues is very small. Moreover, even if this large gain is provided to move the SSR mode to the LHP- since according to Table 6.3, the residues of the SSR mode at these points are in opposite direction with the residues of the electro-mechanical mode- it is expected that with an increasing SSR gain, the electro-mechanical mode will be destabilized.

For the other points of the RSC , i.e. C_{RSC}, E_{RSC}, and F_{RSC}, even if the magnitude of the SSR residues corresponding to these points is large, stabilizing the SSR mode in these cases will also result in decreasing the stability, or even destabilizing, the electro-mechanical mode, as the residues of the SSR mode and electro-mechanical mode point in opposite directions. This should be readily apparent upon examination of the root-locus diagram, shown in Figure 6.8, where the SSRDC with V_C as ICS is implemented at point E_{RSC}. As seen in this figure, although the damping ratio of the SSR mode becomes 6% with K_{SSR} = 80.1, this makes the electro-mechanical mode unstable. In conclusion, all controller insertion points on the RSC are not viable.

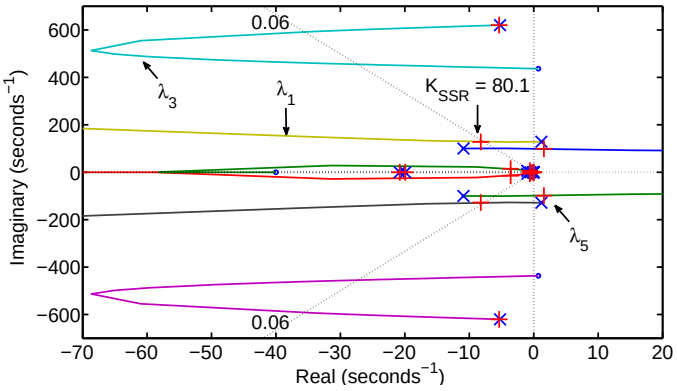

Figure 6.8: Root locus diagram with V_C as ICS with SSRDC implemented in RSC controller at point E_{RSC}.

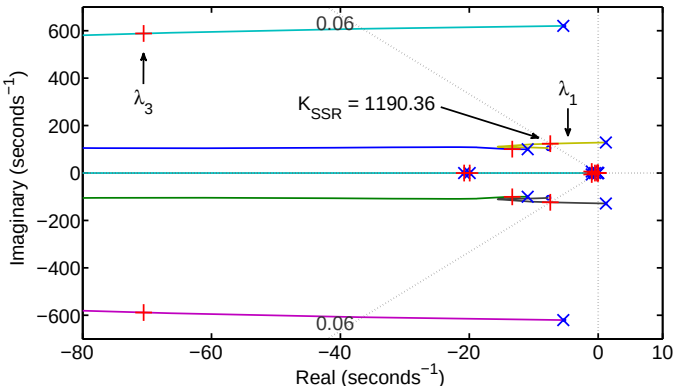

Figure 6.9: Root locus diagram with V_C as ICS with SSRDC implemented in GSC controller at point A_{GSC}

However, when implementing the SSRDC at GSC controller points, i.e. A_{GSC} through C_{GSC}, except the residues of the shaft mode, all other residues point at the same direction with the residues of the SSR mode, as seen in Table 6.3. This shows that stabilizing the SSR mode by increasing the SSR gain can also increase the stability of the SupSR mode and electro-mechanical mode. This operation may destabilize the shaft mode, though this destabilization will not happen due to the much smaller magnitude of the residues of this mode. Figure 6.9 and Figure 6.11 confirm this prediction; stabilizing the SSR mode by increasing the SSR gain has also increased the stability of the SupSR and electro-mechanical

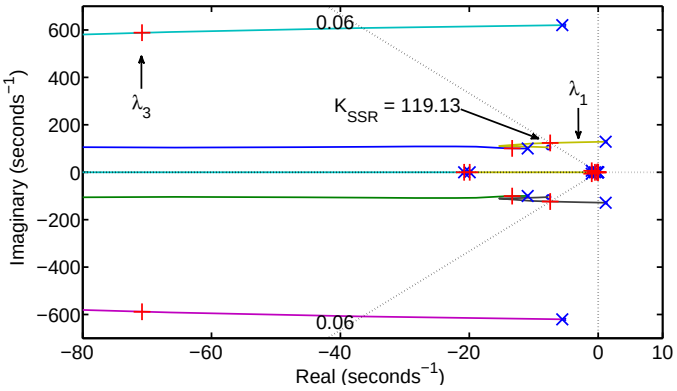

Figure 6.10: Root locus diagram with V_C as ICS with SSRDC implemented in GSC controller at point B_{GSC}.

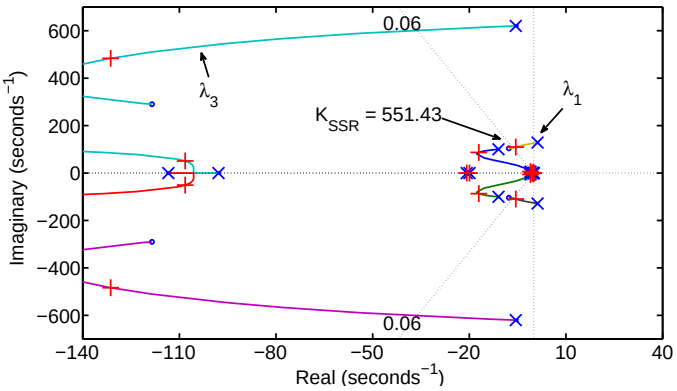

Figure 6.11: Root locus diagram with V_C as ICS with SSRDC implemented in GSC controller at point C_{GSC}.

modes. Moreover, no unstable shaft mode was observed by increasing the SSR gain.

For implementation of the SSRDC at points D_{GSC} through F_{GSC}, the residues of all modes point at the same direction with that of the SSR mode, as seen in Table 6.3. This shows that by increasing the SSR gain, not only the SSR mode will be stabilized, but also this will increase the stability of all other three modes. Moreover, since the residue magnitude of the SSR mode at these points are much larger compared to that of the SSR mode at points A_{GSC} through C_{GSC}, a much smaller SSR gain will be required to stabilize the system. Figure 6.12 - Figure 6.14 represent the root-locus diagrams of the system

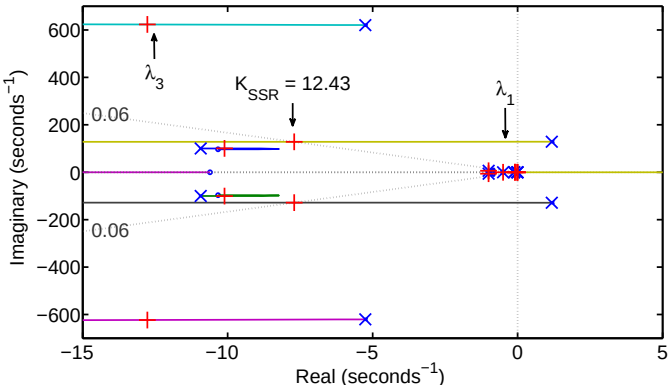

Figure 6.12: Root locus diagram with V_C as ICS with SSRDC implemented in GSC controller at point D_{GSC}.

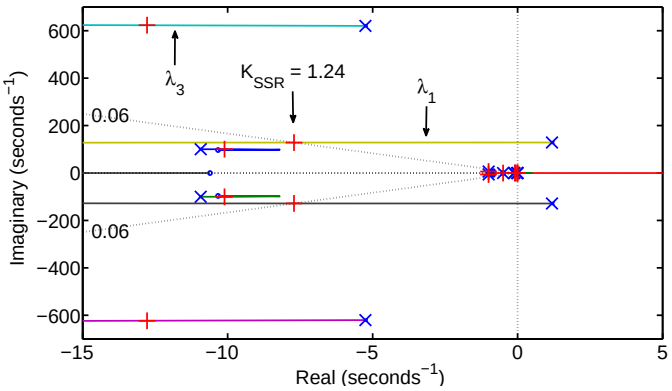

Figure 6.13: Root locus diagram with V_C as ICS with SSRDC implemented in GSC controller at point E_{GSC}.

for the points D_{GSC} through F_{GSC}, respectively, where the required SSR feedback gains to have 6% damping ratio for the SSR mode are indicated in these figures. In conclusion the optimal ICS is the capacitor voltage VC and the optimal controller insertion points are D_{GSC}, E_{GSC} and F_{GSC}.

6.3 Time-Domain Simulation of the Wind Farm with SSRDC

To validate the results of Section 6.2, the time-domain simulation of system shown in Figure 2.1 with the SSRDC is presented. PSCAD/EMTDC is used to perform the simulations.

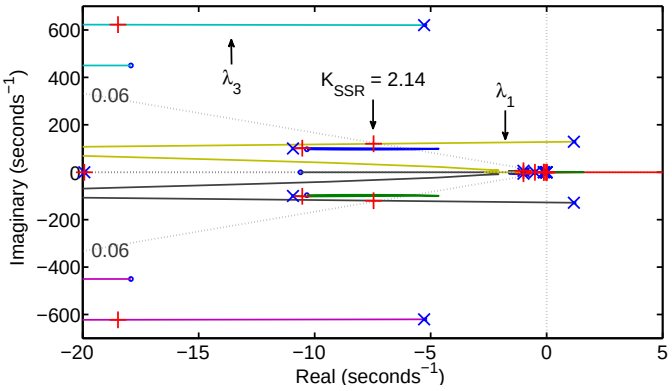

Figure 6.14: Root locus diagram with V_C as ICS with SSRDC implemented in GSC controller at point F_{GSC}.

In the entire simulation results given in this work:

- Initially, the compensation level is regulated at 50%, where the system is stable, and then at $t = 0.5$ s, the compensation level is changed to 55%, where the system is unstable without SSRDC, due to the SSR mode.
- The SSRDC gain K_{SSR} in the simulation is obtained using root-locus diagrams, as mentioned before.

SSRDC Implemented in RSC Controllers

Figure 6.15 show the dynamic performance of the transmission line real power P_L when the SSRDC is implemented at RSC. Figures 6.15- a through -c show that as soon as the compensation level increases from 50% to 55% at $t = 0.5$ s, regardless of which ICS is used, the sub-synchronous and super-synchronous oscillations appear in the transmission line real power, and these oscillations damp out in less than 0.25 s, but another oscillations start to appear in the system dynamics making the wind farm unstable. The frequency of these oscillations are in range of electro-mechanical mode ($\lambda_{5,6}$).

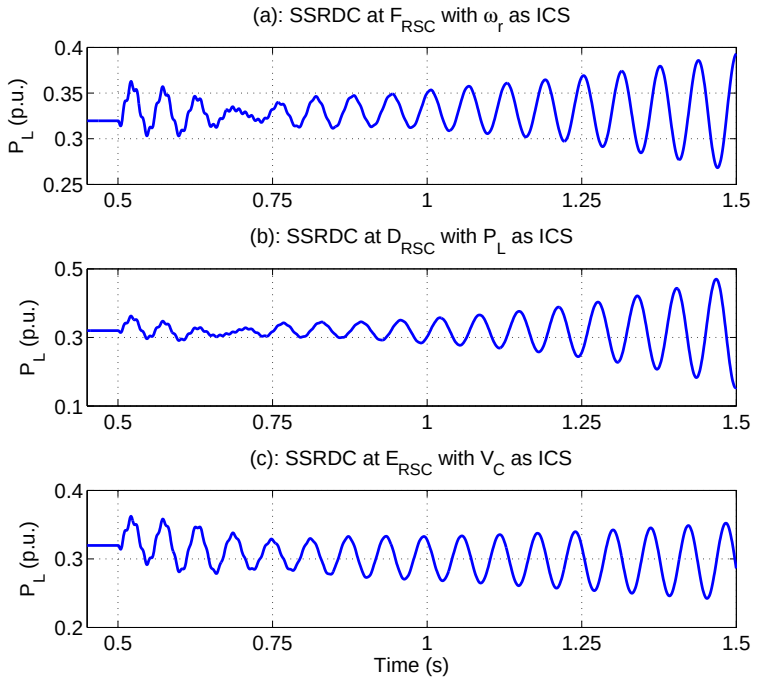

Figure 6.15: Dynamic response of the transmission line real power P_L when the SSRDC is implemented at RSC

Indeed, the reason for the instability of the wind farm in this case is not the SSR mode, but it is the unstable electro-mechanical mode. This was expected from root-locus diagrams shown in Figure 6.5, Figure 6.6, and Figure 6.8. These root-locus figures clearly show that increasing the SSR gain, to make the SSR mode stable, causes the electro-mechanical mode to go unstable. Therefore, in spite of what kind of ICS is used, the SSRDC cannot be implemented at RSC controllers.

SSRDC Implemented in GSC Controllers

Figures 6.16. -a and -b show the dynamic performance of the transmission line real power P_L when the SSRDC is implemented at GSC with ω_r and P_L as ICSs. Figure 6.16. -a and -b show that as soon as the compensation level increases from 50% to 55% at $t = 0.5\ s$, the sub-synchronous and super-synchronous oscillations appear in the transmission line real power, but only the former damps out in less than $0.25\ s$, while the latter is sustained in the

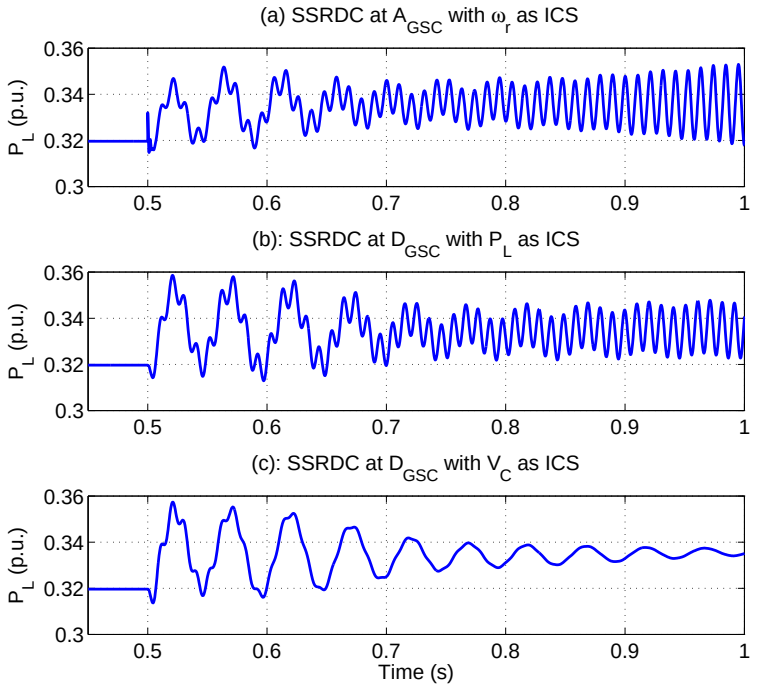

Figure 6.16: Dynamic response of the transmission line real power P_L when the SSRDC is implemented at GSC

system and makes the wind farm unstable.

In fact, the reason for the instability of the wind farm, when variables ω_r and P_L are used as ICS, is not the SSR mode, but it is the SupSR mode. This was expected from root-locus diagrams shown in Figure 6.4 and Figure 6.7. These root-locus figures clearly show that by increasing the SSR gain to make the SSR mode stable, the SupSR mode goes unstable. Therefore, ω_r and P_L cannot be used as ICSs, even when the SSRDC is installed at GSC controllers.

Using V_C as ICS with SSRDC implemented at GSC controllers, on the other hand, can stabilize the wind farm, as illustrated in Figure 6.16.-c. This was expected from the root-locus diagrams shown in Figure 6.9 through Figure 6.14.

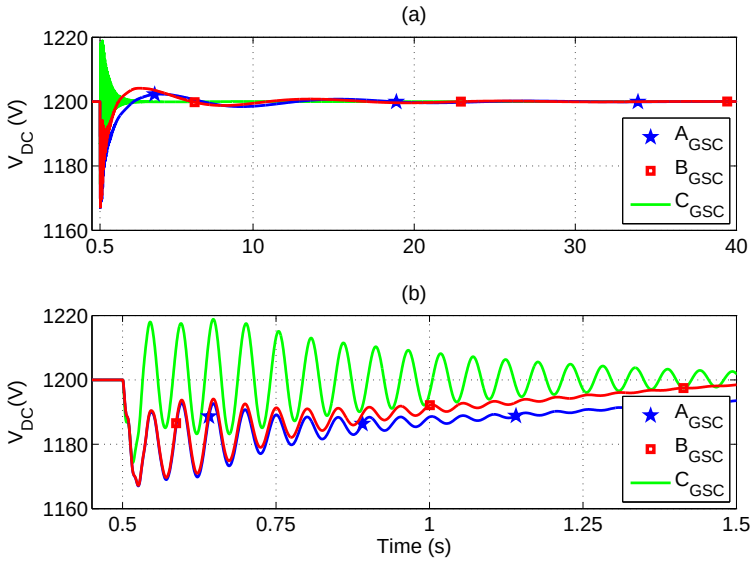

Figure 6.17: Dynamic response of the DC link voltage when SSRDC is implemented A_{GSC}, B_{GSC}, and C_{GSC}. (a). Simulation time from $t = 0.5$ s to $t = 40$ s. (b). Simulation time from $t = 0.45$ s to $t = 1.5$ s.

Optimum Point for SSRDC Implementation in GSC Controllers with V_C as ICS

Figure 6.17 shows the DC link voltage V_{DC}, when the SSRDC is implemented at points A_{GSC}, B_{GSC}, and C_{GSC}. As seen in this figure, the SSRDC has successfully damped the SSR mode, and has made the wind farm stable, as expected from root-locus diagrams given in Figure 6.9 through Figure 6.11. Figure 6.17 shows that implementing the SSRDC at points A_{GSC} and B_{GSC} gives superior performance compared to implementing the SSRDC at C_{GSC} in terms of settling time.

Moreover, Figure 6.18 represents the DC link voltage V_{DC}, when the SSRDC is implemented at points D_{GSC}, E_{GSC}, and F_{GSC} in GSC controllers. As seen in this figure, as expected from root-locus diagrams shown in Figures 6.12 - Figure 6.14, the SSRDC has successfully attenuated the SSR mode and achieved wind farms stability. Figure 6.18 shows that implementing the SSRDC at points D_{GSC} and E_{GSC} brings slightly better performance compared to implementing the SSRDC at points F_{GSC} in terms of settling time.

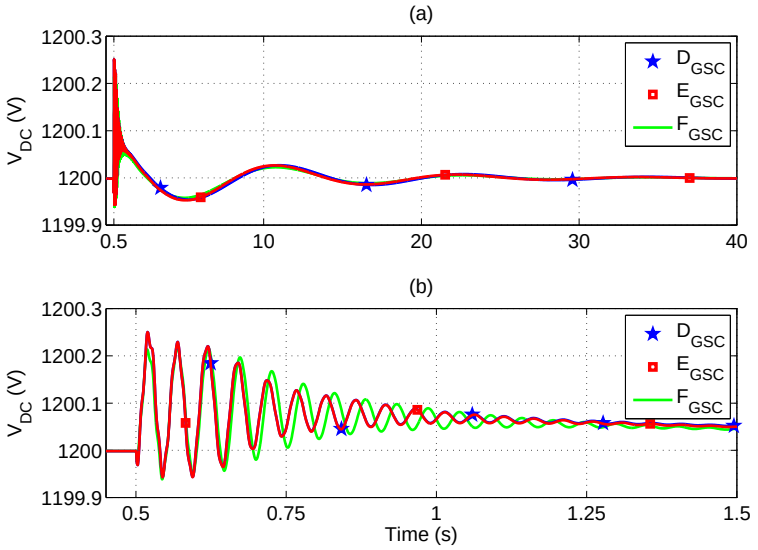

Figure 6.18: Dynamic response of the DC link voltage when SSRDC is implemented at D_{GSC}, E_{GSC}, and F_{GSC}. (a). Simulation time from $t = 0.5\ s$ to $t = 40\ s$. (b). Simulation time from $t = 0.45\ s$ to $t = 1.5\ s$.

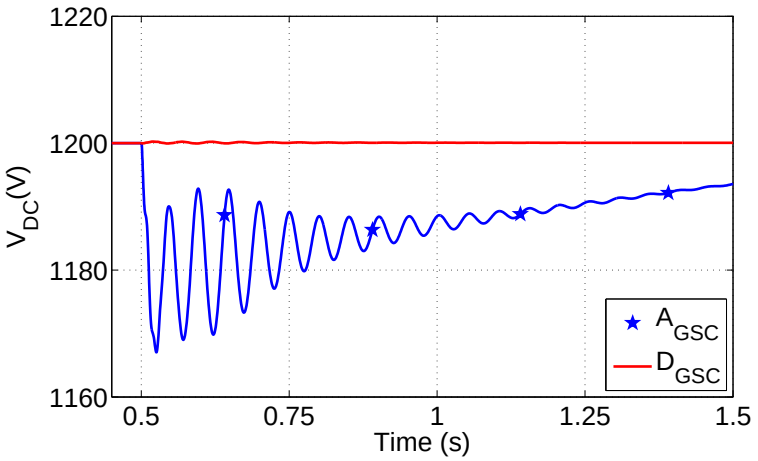

Figure 6.19: Dynamic response comparison when SSRDC is implemented at A_{GSC} and D_{GSC}.

This shows that the SSRDC can interchangeably be implemented at points D_{GSC}, E_{GSC}, and F_{GSC}.

Furthermore, Figure 6.19 compares the DC link with the SSRDC implemented at point A_{GSC} and D_{GSC}. This figure shows that implementation of the SSRDC at point D_{GSC} causes much less overshoot and settling time in DC link voltage compared to when the SSRDC is

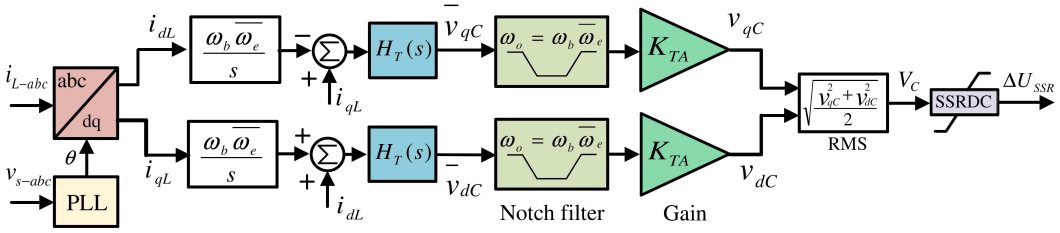

Figure 6.20: Derivation of voltage across the series capacitor using qd-axis line currents (Method A).

implemented at point A_{GSC}. This shows that implementation of the SSRDC at D_{GSC}, E_{GSC}, and F_{GSC} is a better option compared to A_{GSC}, B_{GSC}, and C_{GSC}.

6.4 Discussion of Feasibility of Series Capacitor Voltage as ICS

According to the discussion given in this work, the optimum ICS to the SSRDC is the voltage across the series capacitor, V_C. However, in practical applications of the wind farms, the voltage across the series compensation may not be accessible at the wind turbine for local controls. The question is "can we derive the voltage across the series capacitor using local measurements?" Fortunately, the answer to this question is *Yes*. Here two methods are discussed to derive the V_C from a local measured signal.

Derivation from Line Current in $q-d$ (Method A)

The relation between the line current and series capacitor voltage in $q-d$ frame in Figure 2.1 is as follows [69]:

$$i_{qL} = \frac{1}{\omega_b X_C}\frac{d}{dt}v_{qC} + \frac{\bar{\omega}_e}{X_C}v_{dC} \tag{6.3}$$

$$i_{dL} = -\frac{\bar{\omega}_e}{X_C}v_{qC} + \frac{1}{\omega_b X_C}\frac{d}{dt}v_{dC} \tag{6.4}$$

Or in a matrix and Laplace form:

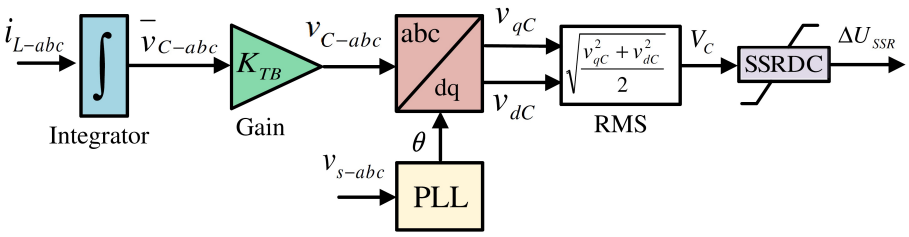

Figure 6.21: Derivation of voltage across the series capacitor using instantaneous line current (Method B).

$$\begin{bmatrix} i_{qL} \\ \\ i_{dL} \end{bmatrix} = \begin{bmatrix} \frac{1}{\omega_b X_C}s & \frac{\bar{\omega}_e}{X_C} \\ -\frac{\bar{\omega}_e}{X_C} & \frac{1}{\omega_b X_C}s \end{bmatrix} \begin{bmatrix} v_{qC} \\ \\ v_{dC} \end{bmatrix} \tag{6.5}$$

Using Eq. 6.5, the series capacitor voltage in $q-d$ frame can be obtained as:

$$\begin{bmatrix} v_{qC} \\ \\ v_{dC} \end{bmatrix} = K_{TA} H_T(s) \begin{bmatrix} 1 & \frac{-\omega_b \bar{\omega}_e}{s} \\ \frac{\omega_b \bar{\omega}_e}{s} & 1 \end{bmatrix} \begin{bmatrix} i_{qL} \\ \\ i_{dL} \end{bmatrix} \tag{6.6}$$

where

$$H_T(s) = \frac{s}{s^2 + (\omega_b \bar{\omega}_e)^2} \tag{6.7}$$

Figure 6.20 shows the block diagram used for the derivation of voltage across the series capacitor V_C from the line current I_L. The notch filter in this figure is used to eliminate the undamped natural frequency in the $H_T(s)$ transfer function located at $\omega_{tn} = \omega_b \bar{\omega}_e$. Moreover, in Figure 6.20, $K_{TA} = \omega_b X_C$. In case the exact value of the X_C is not known, this gain can be used to tune the SSRDC in order to obtain the required SSR damping ratio.

Derivation from Instantaneous Line Current (Method B)

The relationship between the instantaneous line current and capacitor voltage is give as follows:

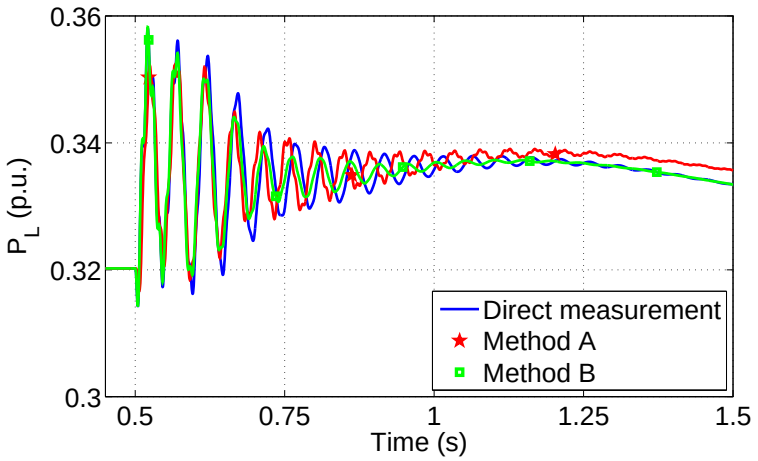

Figure 6.22: Transmission line real power P_L obtained with: direct measurement of V_C, method A, and method B.

$$C\frac{dv_{C-abc}}{dt} = i_{L-abc} \tag{6.8}$$

Eq. 6.8 shows that the capacitor voltage can be estimated through the local current. Figure 6.21 shows the block diagram used to estimate the voltage across the capacitor. The value of K_{TB} in Figure 6.21 is equal to $\frac{1}{C}$. Even in case the exact value of the series capacitor is not known, the SSRDC can be tuned using K_T to obtain the required SSR damping ratio.

Simulation Results

In order to examine the effectiveness of method A and method B in estimating voltage across the series capacitor, Figure 6.22 compares the transmission line power with the V_C as ICS for the SSRDC. In this figure, V_C is obtained using direct measurement, method A, and method B. As seen in this figure, both method A and B can successfully estimate the voltage across the series capacitor.

6.5 SUMMARY

In this chapter, SSR mitigation in DFIG-based wind farm using rotor-side converter (RSC) and grid-side converter (GSC) controllers is studied. To mitigate the SSR, a SSRDC is designed using residue-based analysis and root-locus method, and the designed SSRDC is implemented at different points of the RSC and GSC controllers (see Figure 6.1 and Figure 6.2) in order to identify the optimum points within these controllers for the SSRDC implementation. The residue-based analysis is used to identify an optimum input control signal (ICS) to the SSRDC amongst three tested signals namely generator rotor speed ω_r, line real power P_L, and voltage across the series capacitor V_C, and root-locus method is used to compute the required SSRDC gain to stabilize the SSR mode, while verifying the residue-based analysis.

The optimum ICS and optimum point in RSC and GSC controllers should enable the SSRDC to stabilize the SSR mode, without destabilizing or decreasing the stability of other system modes. In summary, the following results can be drawn regarding the optimum converter and ICS:

1. Using the SSRDC design method presented in this work, ω_r and P_L can cause the SupSR mode or the electro-mechanical mode (or even both of them together) to go unstable, when used to stabilize the SSR mode, regardless of the insertion point chosen for the SSRDC implementation. It may be possible to successfully use these signals for SSR stabilization, but a more complex compensation would be required, losing the simplicity of the proposed proportional controller. The investigation of more complex compensation options is left as future work.

2. Neither of RSC controllers can be used to implement the SSRDC, regardless of what the ICS is.

3. All points of the GSC controllers can be used to implement the SSRDC, when the ICS is V_C.

4. With V_C as ICS, implementation of the SSRDC at points D_{GSC} through F_{GSC} requires a smaller SSR feedback gain compared to A_{GSC} through C_{GSC}.

5. Time-domain simulation in PSCAD/EMTDC verifies the SSRDC design process.

Table 6.1: Residue of the SSR and SupSR, electro-mechanical, and shaft modes at $V_\omega = 7\ m/s$ and $K = 55\%$: ω_r as ICS.

$V_\omega = 7m/s - K = 55\%$	ω_r as ICS			
	SSR Mode	SupSR Mode	Elec. Mech. Mode	Shaft Mode
A_{RSC}	$5.7922e^{-11}\angle 55.4^o$	$4.2400e^{-13}\angle -107.2^o$	$9.7227e^{-11}\angle -152.6^o$	$2.9204e^{-10}\angle -156.5^o$
B_{RSC}	$5.7152e^{-7}\angle 64.3^o$	$4.2389e^{-9}\angle -105.4^o$	$9.7406e^{-7}\angle -141.2^o$	$8.9096e^{-7}\angle -74.6^o$
C_{RSC}	$3.0766\angle -57.4^o$	$0.0387\angle 102.5^o$	$4.5807\angle 107.6^o$	$0.2223\angle -154.6^o$
D_{RSC}	$1.0653e^{-7}\angle -57.9^o$	$4.1038e^{-10}\angle 134.7^o$	$1.8556e^{-7}\angle 93.4^o$	$6.0627e^{-6}\angle -176.1^o$
E_{RSC}	$0.0010\angle -40.6^o$	$4.0975e^{-6}\angle 138.4^o$	$0.0017\angle 115.8^o$	$.0093\angle -85.4^o$
F_{RSC}	$3.1042\angle 30.9^o$	$0.0381\angle 174.4^o$	$4.5029\angle -162.2^o$	$1.4504\angle 13.1^o$
A_{GSC}	$4.6968e^{-5}\angle -57.7^o$	$0.0001\angle 111.8^o$	$4.6674e^{-5}\angle -95.8^o$	$6.8484e^{-6}\angle -67.1^o$
B_{GSC}	$0.0007\angle -57.5^o$	$0.0012\angle 113.4^o$	$0.0001\angle -95.5^o$	$6.9265e^{-5}\angle -62.4^o$
C_{GSC}	$0.0006\angle -19.8^o$	$0.0012\angle 121.1^o$	$0.0001\angle -47.6^o$	$4.2303e^{-6}\angle 33.4^o$
D_{GSC}	$0.0059\angle -83.8^o$	$0.0010\angle 73.7o$	$0.0007\angle 116.6^o$	$0.0008\angle 115.4^o$
E_{GSC}	$0.0593\angle -83.6^o$	$0.0104\angle 73.8^o$	$0.0077\angle 116.9^o$	$0.0075\angle 120.1^o$
F_{GSC}	$0.0466\angle -45.9^o$	$0.0105\angle 82.9^o$	$0.0058\angle 164.8^o$	$0.0004\angle -143.8^o$

Table 6.2: Residue of the SSR and SupSR, electro-mechanical, and shaft modes at $V_\omega = 7\ m/s$ and $K = 55\%$: P_L as ICS.

$V_\omega = 7m/s - K = 55\%$	P_L as ICS			
	SSR Mode	SupSR Mode	Elec. Mech. Mode	Shaft Mode
A_{RSC}	$9.8321e^{-9}\angle -33.5^o$	$3.4496e^{-10}\angle 158.3^o$	$1.2827e^{-8}\angle 125.7^o$	$4.5664e^{-10}\angle -148.8^o$
B_{RSC}	$9.7013e^{-5}\angle -24.6^o$	$3.4484e^{-6}\angle 160.1^o$	$0.0001\angle 137.1^o$	$1.3930e^{-6}\angle -66.9^o$
C_{RSC}	$522.2481\angle 32.6^o$	$31.5041\angle -171.8^o$	$604.3783\angle -154.6^o$	$0.3480\angle 32.9^o$
D_{RSC}	$1.7985e^{-5}\angle 32.1^o$	$3.3388e^{-7}\angle -139.6^o$	$2.4572e^{-5}\angle -168.7^o$	$9.4786e^{-6}\angle 11.1^o$
E_{RSC}	$0.1712\angle 49.3^o$	$0.0033\angle -135.9^o$	$0.2373\angle -146.3^o$	$0.0146\angle 101.8^o$
F_{RSC}	$524.7688\angle 121.1^o$	$31.0048\angle -99.9^o$	$594.4558\angle -64.5^o$	$2.2687\angle -159.5^o$
A_{GSC}	$0.0131\angle 33.2^o$	$0.0974\angle -162.5^o$	$0.0027\angle 2.5^o$	$1.2946e^{-5}\angle 120.4^o$
B_{GSC}	$0.1315\angle 33.4^o$	$0.9746\angle -162.4^o$	$0.0261\angle 2.8^o$	$0.0001\angle 125.1^o$
C_{GSC}	$0.1033\angle 71.1^o$	$0.9634\angle -153.2o$	$0.0196\angle 50.7^o$	$8.01651e^{-6}\angle -138.8^o$
D_{GSC}	$1.0082\angle 7.1^o$	$0.8667\angle 159.3^o$	$0.1019\angle -144.9^o$	$0.0011\angle -56.8^o$
E_{GSC}	$10.0817\angle 7.3^o$	$8.6672\angle 159.4o$	$1.0198\angle -144.6^o$	$0.0118\angle -52.1^o$
F_{GSC}	$7.9216\angle 45.0^o$	$8.5681\angle 168.5^o$	$0.7664\angle -96.7^o$	$0.0007\angle 43.8^o$

Table 6.3: Residue of the SSR and SupSR, electro-mechanical, and shaft modes at $V_\omega = 7\ m/s$ and $K = 55\%$: V_C as ICS

$V_\omega = 7m/s - K = 55\%$	V_C as ICS			
	SSR Mode	SupSR Mode	Elec. Mech. Mode	Shaft Mode
A_{RSC}	$5.8808e^{-9}\angle -38.7^o$	$2.1628e^{-10}\angle -22.1^o$	$6.9276e^{-9}\angle 125.8^o$	$1.3344e^{-10}\angle -140.2^o$
B_{RSC}	$5.7765e^{-5}\angle -29.8^o$	$2.1623e^{-6}\angle -20.3^o$	$6.9392e^{-5}\angle 137.1^o$	$4.0756e^{-7}\angle -58.3^o$
C_{RSC}	$312.0201\angle 27.3^o$	$19.7537\angle 7.6^o$	$327.2719\angle -154.5^o$	$0.1016\angle 41.5^o$
D_{RSC}	$1.0752e^{-5}\angle 26.9^o$	$2.0934e^{-7}\angle 39.8^o$	$1.3257e^{-5}\angle -168.7^o$	$2.7709e^{-6}\angle 20.1^o$
E_{RSC}	$0.1023\angle 44.1^o$	$0.0020\angle 43.5^o$	$0.1281\angle -146.3^o$	$0.0042\angle 110.7^o$
F_{RSC}	$313.2\angle -64.9^o$	$19.4\angle -100.4^o$	$321.7\angle 114.7^o$	$0.6629\angle 28.9^o$
A_{GSC}	$0.0078\angle 27.2^o$	$0.0611\angle 16.9^o$	$0.0014\angle 1.8^o$	$3.8819e^{-6}\angle 128.9^o$
B_{GSC}	$0.0783\angle 27.4^o$	$0.6110\angle 17.0^o$	$0.0141\angle 2.1^o$	$133.6e^{-5}\angle 140.2^o$
C_{GSC}	$0.0615\angle 65.1^o$	$0.6041\angle 26.2^o$	$0.01061\angle 50.0^o$	$2.3978e^{-6}\angle -122.9^o$
D_{GSC}	$0.6003\angle 12.5^o$	$0.6238\angle 2.4^o$	$0.2137\angle 30.5^o$	$0.0014\angle -10.1^o$
E_{GSC}	$4.5777\angle 12.8^o$	$6.2381\angle 2.4^o$	$2.1396\angle 30.8^o$	$0.0144\angle -18.4^o$
F_{GSC}	$3.1982\angle 52.6^o$	$6.1732\angle 11.2^o$	$1.6500\angle 84.8^o$	$0.0008\angle -27.6^o$

CHAPTER 7

GAIN - SCHEDULING ADAPTIVE SSRDC DESIGN

The dynamics of the DFIG-based series compensated wind farm vary as the operating point conditions change. Two main sources of changes in the dynamics of the system come from the wind speed V_{ω} and the series compensation level K. In this section, a gain-scheduling adaptive SSRDC (GSA-SSRDC) is designed so that the SSRDC is less affected by change of the system dynamics.

7.1 GAIN - SCHEDULING ADAPTIVE SSRDC DESIGN

Gain - Scheduling Adaptive Control

In many situations, it is known how changes in the operating conditions of a process affect the dynamics of the process itself. Therefore, it is possible to adjust the parameters of the controller as a function of the operating point conditions of the entire system in order to maintain good control performance. This method is called gain-scheduling adaptive (GSA) control. The generic block diagram of a system, where the effects of parameter variations are compensated by AGS is shown in Figure 7.1 [102]. The GSA control enables the control of a non-linear system by varying the parameters of a linear controllers, so that a desired response is obtained for the different operating points of the non-linear system [102], [103]. GSA has the advantages, with respect to conventional adaptive control, that the controller parameters can be changed rapidly, as the operating point changes. There are several examples of application of GSA in literature [104], [105] in system controls. For example, in [104], GSA control is used for sensor less control of induction machines.

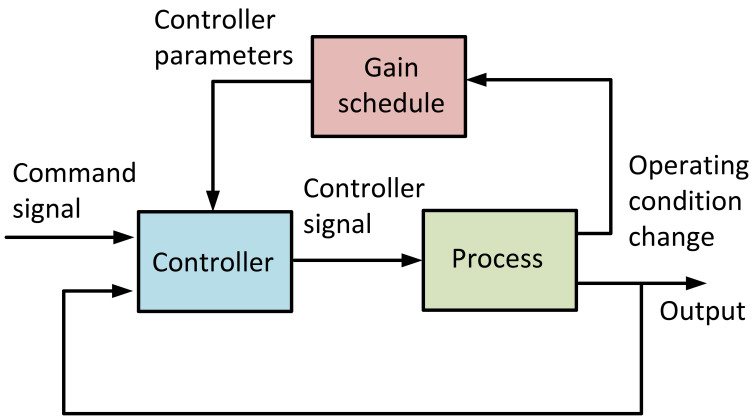

Figure 7.1: Generic block diagram of a gain-scheduled adaptive control.

Table 7.1: SSR modes of the system at different wind speeds V_ω and compensation levels K.

V_ω (m/s)-K (%)	SSR Mode
7 - 50	-1.8784 $\pm$ j140.7799
7 - 55	**+1.2126** $\pm$ j128.5545
7 - 60	**+5.9289** $\pm$ j118.8507
7 - 65	**+9.6991** $\pm$ j112.3237
8 - 55	-3.7739 $\pm$ j128.5441
8 - 60	-2.3818 $\pm$ j116.5455
8 - 65	-0.4696 $\pm$ j104.8237
9 - 55	-6.8362 $\pm$ j122.7589
9 - 60	-5.5889 $\pm$ 115.9793
9 - 65	-3.7165 $\pm$ j105.3277

Moreover, in [105], this method is used for control of grid-connected inverters.

Variation of DFIG Operating Point

Table 7.1 shows the SSR mode of the system for different wind speeds and series compensation levels. As seen in This table, changing the operating points of the wind farm can change the SSR mode's frequency and damping. On the one hand, increasing the compensation level decreases the stability of the SSR mode. On the other hand, as seen in Table 7.1, by increasing the wind speed, the stability of the SSR mode increases. This can be explained as follows:

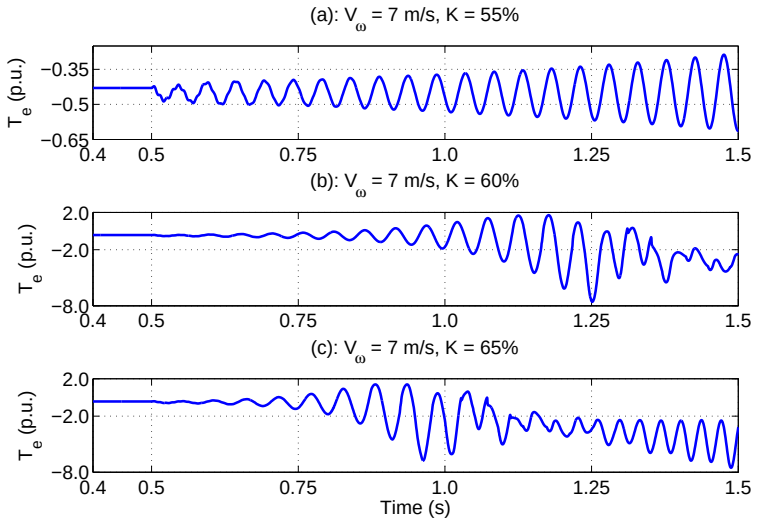

Figure 7.2: Electric torque at $V_\omega = 7\ m/s$ and: (a) $K = 55\%$ (b) $K = 60\%$ (a) $K = 65\%$.

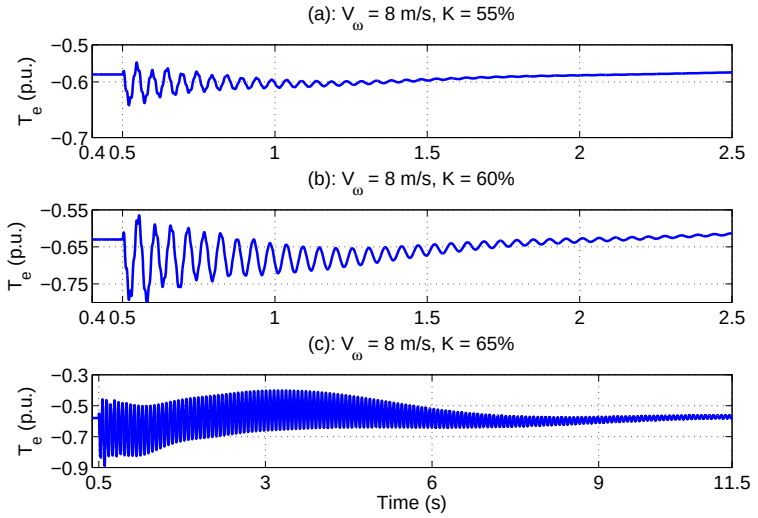

Figure 7.3: Electric torque at $V_\omega = 8\ m/s$ and: (a) $K = 55\%$ (b) $K = 60\%$ (a) $K = 65\%$.

Figure 7.2 through Figure 7.4 show time-domain simulation of the system for different series compensation levels and wind speeds. Theses figures show that both wind speed and compensation level influence the stability of the system, verifying the eigenvalue analysis given in Table 7.1.

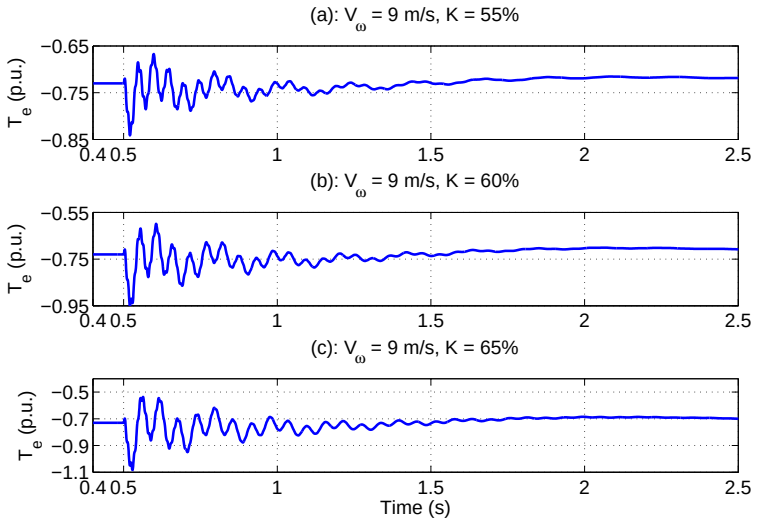

Figure 7.4: Electric torque at $V_\omega = 9\ m/s$ and: (a) $K = 55\%$ (b) $K = 60\%$ (a) $K = 65\%$. K is series compensation level.

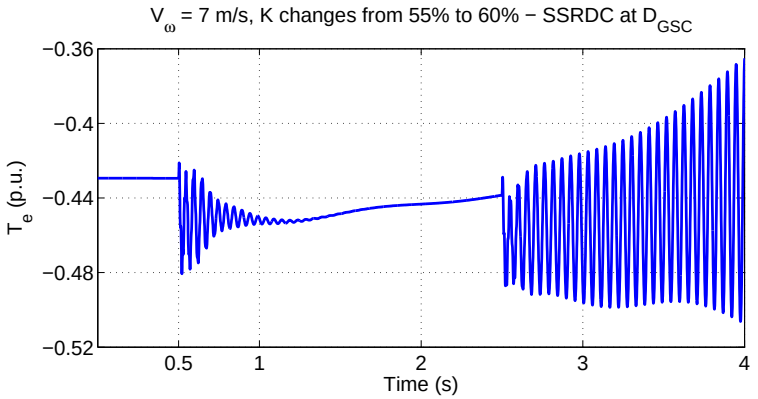

Figure 7.5: Dynamic response of the system to series compensation change from 50% to 60% at constant wind speed, 7 m/s, when SSRDC is implemented at D_{GSC}.

Adaptive SSRDC Design

Considering the series compensated DFIG-based wind farm as a non-linear system, the AGS method is a good way to compensate for variation in the dynamics of the wind farm. Using this method, it is possible to monitor the operating condition of the wind farm and to adjust the parameters of the SSRDC.

Since in the DFIG series compensated wind farm both the wind speed and series compensation level change, the SSRDC designed for only one operating point, e.g. when V_ω

Table 7.2: Values of the SSRDC gain, K_{SSR}, for different wind speeds and series compensation levels.

	$K = 55\%$	$K = 60\%$	$K = 65\%$
$V_\omega = 7\ m/s$	12.43	23.65	61.04
$V_\omega = 8\ m/s$	6.47	7.23	8.41
$V_\omega = 9\ m/s$	0.53	0.69	0.73

$= 7$ m/s and $K = 55\%$, may not be adequate to enhance the stability of the wind farm for other operating points. For example, Figure 7.5. shows the electric torque of the system, when the series compensation level increases first from 50% to 55% at $t = 0.5\ s$, and then from 55% to 60% at $t = 2.5\ s$, while the SSRDC is designed for $V_\omega = 7$ m/s and $K = 55\%$. As seen in this figure, the designed SSRDC for $V_\omega = 7$ m/s and $K = 55\%$ is unable to stabilize the wind farm when the series compensation level increases at $t = 2.5\ s$ from 55% to 60%. This shows that the values of the SSRDC gain, i.e. K_{SSR}, should be adjusted as a function of the the wind farm operating points.

In this work, the following steps are defined to design a gain-scheduling adaptive SSRDC (AGS-SSRDC) to the system.

1. Obtain the non-linear model of the series compensated DFIG-based wind farm.

2. Linearize the non-linear system in (1) using "linmod" command as explained in Chapter 2.

3. Obtain the SSRDC gains, K_{SSR} for different operating points of the wind farm, i.e. different wind speed and compensation level, using the root-locus method explained in previous chapters in order to create a table for gain K_{SSR} as a function of operating point.

Table 7.2 gives the computed K_{SSR} for some selected wind speed V_ω and series compensation levels K. During wind farm operation, depending on the wind farm operating point, the SSRDC is adapted using the computed gain K_{SSR}.

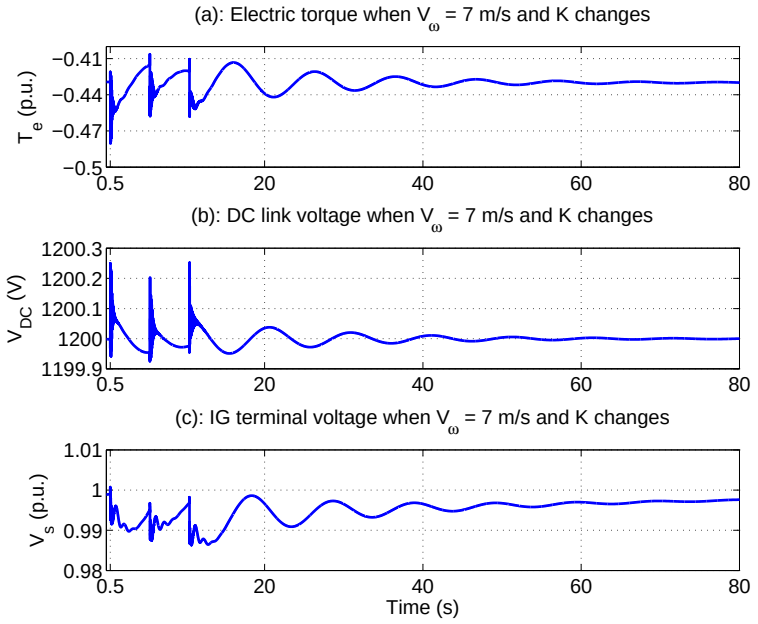

Figure 7.6: Dynamic response of the system with adaptive gain-scheduling SSRDC for $V_\omega = 7\ m/s$ and different compensation levels.

Time-Domain Simulation of DFIG with AGS-SSRDC

The system shown in Figure 2.1 was simulated in PSACD/EMTDC with AGS-SSRDC designed as explained in Section 7.1. In order to examine the robustness of the AGS-SSRDC, the system was simulated while the operating point of the wind farm is varied including step changes in series compensation level K or wind speed $V\omega$. Figure 7.6 and Figure 7.7 represent the dynamic response of the system including electric torque T_e, DC link voltage V_{DC}, and terminal voltage V_s when the wind speed is kept constant and the compensation level is changed. These figures clearly show that adapting the gain of the SSRDC has successfully sustained the stability of the wind farm even when the operating point of the wind farm is changed. The designed AGS-SSRDC was also tested when either only wind speed, or even both wind speed and compensation level are changed, simultaneously. The obtained results show that the designed AGS-SSRDC is robust against both wind speed and compensation level variations.

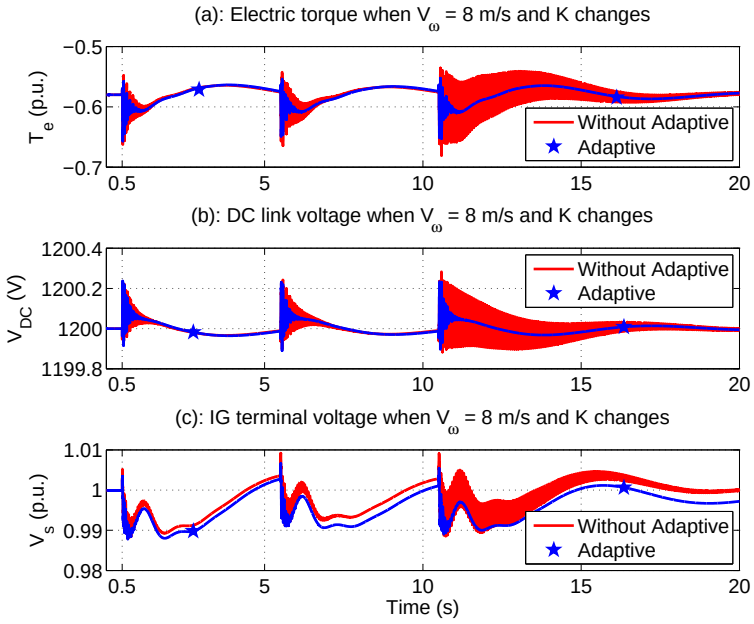

Figure 7.7: B. Dynamic response of the system with adaptive-gain-scheduling SSRDC for $V_\omega = 8\ m/s$ and different compensation levels.

7.2 SUMMARY

The main sources of variation of the operating point in the DFIG are wind speed variation and series compensation level change. The gain-scheduling adaptive method is a very useful technique for reducing the effects of operating point condition variations. In this chapter, the performance of the designed SSRDC in Chapter 6 is optimized using the adaptive gain-scheduling method in order to handle the operating point condition variations of the wind farm. The results show that using gain-scheduling adaptive method, the SSRDC is less affected by variations of the operating point of the wind farm.

CHAPTER 8

CONCLUSION AND FUTURE WORK

8.1 PROBLEM

Worldwide rapid penetration of wind power into electric power grids makes it necessary for the power utilities to transmit the generated wind power without congestion. In addition, the global trend towards a deregulated power market requires that any solution to increase the power transfer capability of an existing transmission line be financially competitive. In many cases, cost effective series compensation increases the transmissible power of an existing transmission line at a fraction of the cost and required time to build a new transmission line.

8.2 CHALLENGES

However, a factor hindering the extensive use of series capacitive compensation is the potential risk of sub-synchronous resonance (SSR), which may cause severe damage in the wind farm, if not prevented. For example, in 2009 a SSR event happened in Electric Reliability Council of Texas (ERCOT) electric grid, leading to damage to both the series capacitor and the wind turbines.

8.3 SOLUTION

In order to take advantage of series compensation benefits, without causing the SSR problem in power systems, properly designed power electronics controllers and FACTS devices could be used. FACTS devices are required in order to support massive integration of re-

newable energy resources into the power networks. Although FACTS devices are flexible and effective, they are an expensive solution. Therefore, some cost-effective and alternative solutions may also be considered in order to assure the effective use of series compensation in transmission lines without being concerned about SSR occurrence. For example, the grid side converter (GSC) of a DFIG has a topology similar to that of a static synchronous compensator (STATCOM), yet exchanges both active and reactive power at fast speeds. Therefore, the control capability of DFIG-based wind farms in mitigating SSR through an auxiliary damping controller at the GSC could be explored.

8.4 CONTRIBUTION

This work has:

1. Developed a comprehensive approach on small-signal stability analysis of a doubly-fed induction generator (DFIG)-based series compensated wind farm using Matlab/Simulink. The developed approach could be easily implemented for the small signal stability analysis of power systems with any complexity. The developed model could be used to obtain eigenvalues of the system and to help to design controllers using eigenvalue analysis method.

2. Proposed application and control of the gate-controlled series capacitor (GCSC) as new series FACTS device for series compensation and sub-synchronous resonance (SSR) damping in wind farms.

3. Designed a novel SSR damping controller (SSRDC) for the GCSC using residue-based analysis and root locus diagrams. Using residue-based analysis, the optimal input control signal (ICS) to the SSRDC is identified to damp the SSR mode without destabilizing other modes, and using root-locus analysis the required gain for the SSRDC is determined

4. Investigated the capability of the thyristor-controlled series capacitor in SSR damping in DFIG-based wind farms.

5. Utilized the rotor-side converter (RSC) and grid-side converter (GSC) controllers of the DFIG for SSR damping, without the need for inserting a FACTS device in the line. The objective was to design a simple proportional SSR damping controller (SSRDC) by properly choosing an optimum input control signal (ICS) to the SSRDC block so that the SSR mode becomes stable without decreasing or destabilizing the other system modes. In the design process, I also identified and introduced the optimum point within the RSC and GSC controllers to insert the SSRDC.

6. Proposed two new methods in order to estimate the optimum input signal to the SSRDC without measuring it directly. These two proposed methods make the proposed methods in my dissertation more effective and applicable in real world applications.

7. Optimized the performance of the proposed controllers using adaptive controller.

8. Validated the designed controllers using detailed time-domain simulations in both Matlab/ SimPowerSystems and PSCAD/EMTDC.

8.5 Future Work

Research is an evolving and endless process, and in this process, the following future works are suggested:

1. Building a scaled-down prototype of the GCSC.

2. Investigating the effect of other series and shunt FACTS devices such as STATCOM, SSSC, UPFC, ect. on SSR damping in wind farms, and comparing the cost and performance of those devices with the proposed methods.

3. Designing a SSRDC for the presented devices using other methods, such as pole-placement method.

4. Studying the application of the presented FACTS devices in low-voltage ride-through (LVRT) enhancement in wind farms.

Moreover, developing more advanced power electronic technologies for the wind farms is desired. The state-of-the-art configurations and roles of power electronics in the wind turbine system show that the behavior and performance of wind turbines can be significantly improved by introducing more advanced power electronic technologies. By proper controls and grid regulations, it is possible for the wind farms to act like conventional power plants and actively contribute to the frequency and voltage control in the grid system, thus making the wind energy more suitable for the integration into the power grid. Therefore, developing more advanced power electronic technologies for the wind farms in order to enhance the grid integration and compatibility of the wind farms in power systems is desired, so that lower energy cost, higher reliability, and better grid integration are obtained for the wind farms.

Finally, studying the connection of offshore wind farms to the grid using high-voltage dc (HVDC) transmission lines could be another future work. Due to environmental and social aspects, the offshore wind farms are larger in size and located further away from the shore. If the distance is too long or the grid to which the offshore wind farm is connected is weak, the HVDC transmission system might be a more suitable and feasible solution than the conventional high-voltage ac (HVAC) transmission. Moreover, various studies have shown that above a certain critical distance, the HVDC option becomes the most appropriate option since it reduces the cable losses, decreases reactive power requirements, and improves power system stability. Therefore, extending the current research toward the HVDC technology, for connection of offshore wind farms to the transmission systems, is suggested.

BIBLIOGRAPHY

[1] S. Chuangpishit, A. Tabesh, Z. Moradi-Sharbabk, M. Saeedifard, "Topology design for collector systems of offshore wind farms with pure DC power systems," *IEEE Trans. Industrial Electronics*, vol. 61, no. 1, pp. 320-328, Jan. 2014.

[2] H. A. Mohammadpour, E. Santi, "An optimal auxiliary gain - scheduling adaptive SSR damping controller design for rotor - side and grid - side converter controllers of series compensated DFIG - based wind farm," *IET Renewable Power Generation*, Provisionally Accepted.

[3] T. Ackermann, *Wind power in power systems*, England, John Wiley & Sons, 2005.

[4] F. Besnard, K. Fischer, L. B. Tjernberg, "A Model for the optimization of the maintenance support organization for offshore wind farms," *IEEE Trans. Sustainable Energy*, vol. 4, no. 2, pp. 443-450, Apr. 2013.

[5] H. A. Mohammadpour, A. Ghaderi, E. Santi, "Analysis of sub-synchronous resonance in doubly-fed induction generator-based wind farms interfaced with gate âĂŞ controlled series capacitor ," *IET Generation, Transmission & Distribution*, DOI: 10.1049/iet-gtd.2013.0643, Available on-line: 16 June 2014.

[6] R. Cardenas, R. Pena, S. Alepuz, G. Asher, "Overview of control systems for the operation of DFIGs in wind energy applications," *IEEE Trans. Ind. Electron.*, vol. 60, no. 7, pp. 2776-2798, July 2013.

[7] Ghaderi, A.; Esmaeilian, A.; Kalantar, M., "A novel islanding detection method for constant current inverter based distributed generations," Environment and Electrical Engineering (EEEIC), 2011 10th International Conference on , vol., no., pp.1,4, 8-11 May 2011

[8] G. Hua Geng, L. Cong Liu, Y. Geng Yang, "LVRT capability of DFIG-based WECS under asymmetrical grid fault condition," *IEEE Trans. Industrial Electronics*, vol.60, no.6, pp.2495-2509, June 2013.

[9] Wenyong Guo, Liye Xiao, Shaotao Dai, Yuanhe Li, Xi Xu, Weiwei Zhou, Luo Li,

"LVRT capability enhancement of DFIG with switch type fault current limiter," *IEEE Trans. Industrial Electronics*, DOI: 10.1109/TIE.2014.2326997, Early Access, 2014.

[10] T. Ackermann, "Transmission systems for offshore wind farms," *Power Engineering Review, IEEE*, vol.22, no.12, pp.23-27, December 2002.

[11] A. GarcÃl's, A. M. Molinas,"A study of efficiency in a reduced matrix converter for offshore wind farms," *IEEE Trans. Industrial Electronics*, vol.59, no.1, pp.184-193, Jan. 2012.

[12] M. Islam, H. A. Mohammadpour, A. Ghaderi, Y. J. Shin, "Time-frequency based instantaneous power components for transient disturbances according to IEEE standard 1459 ," *IEEE Transactions on Power Delivery*, Accepted for Publication.

[13] G. D. Marques, Matteo F. Iacchetti, "Stator frequency regulation in a field-oriented controlled DFIG connected to a DC link," *IEEE Trans. Industrial Electronics*, vol.61, no.11, pp.5930-5939, November 2014.

[14] M. Islam, H. A. Mohammadpour, P. Stone, Y. J. Shin, "Time-frequency based power quality analysis of variable speed wind turbine generators," *IEEE 39th Annual Conference of the Industrial Electronics Society, (IECON) 2013*, pp. 6426 - 6431, 10 - 13 Nov., Vienna, Austria.

[15] M. Amundarain, M. Alberdi, A. J. Garrido, I. Garrido, "A new Interconnecting method for wind turbine/generators in a wind farm and basic performances of the integrated system," *IEEE Trans. Industrial Electronics*, vol.57, no.2, pp.468-475, Feb. 2010.

[16] P. Mitra, Lidong Zhang, L. Harnefors, "Offshore wind integration to a weak grid by VSC-HVDC links using power-synchronization control: a case Study," *IEEE Transactions on Power Delivery*, vol.29, no.1, pp.453,461, Feb. 2014

[17] N. Holtsmark, H. J. Bahirat, M. Molinas, B. A. Mork, H. K. HÃÿidalen, "An all-DC offshore wind farm with series-connected turbines: an alternative to the classical parallel AC model?," *IEEE Trans. Industrial Electronics*, vol.60, no.6, pp.1877-1886, June 2013.

[18] N. Denniston, A. M. Massoud, S. Ahmed, P. N. Enjeti,"Multiple-module high-gain high-voltage DCâĂŞDC transformers for offshore wind energy systems," *IEEE Trans. Industrial Electronics*, vol.58, no.5, pp.1877-1886, May 2011.

[19] R. Teixeira Pinto, P. Bauer, S. F. Rodrigues, E. J. Wiggelinkhuizen, J. Pierik, B. Ferreira, “A novel distributed direct-voltage control strategy for grid integration of offshore wind energy systems through MTDC network,” *IEEE Trans. Industrial Electronics*, vol.60, no.6, pp.2429-2441, June 2013.

[20] Soledad Bernal-Perez, Salvador AÃśÃş-Villalba, Ramon Blasco-Gimenez, “Efficiency and fault ride-through performance of a diode-rectifier- and VSC-inverter-based HVDC link for offshore wind farms,” *IEEE Trans. Industrial Electronics*, vol.60, no.6, pp.2401-2409, June 2013.

[21] R. Blasco, N. Aparicio, S. AÃśÃş-Villalba, S. Bernal-Perez, “LCC-HVDC connection of offshore wind farms with reduced filter banks,” *IEEE Trans. Industrial Electronics*, vol.60, no.6, pp.2372-2380, June 2013.

[22] C. J. Chou, Y. K. Wu, Member, G. Y. Han, C. Y. Lee, “Comparative evaluation of the HVDC and HVAC links integrated in a large offshore wind farm âĂŤ an actual case study in Taiwan,” *IEEE Transactions on Industry Applications*, vol.48, no.5, pp.1639-1648, September 2012.

[23] “Series compensation: boosting transmission capacity,” http://www.abb.com/FACTS.

[24] N. G. Hingorani and L. Gyugi, *Understanding FACTS*. Piscataway, NJ, 656 USA: IEEE Press, 2000.

[25] Esmaeilian, A.; Ghaderi, A.; Tasdighi, M.; Rouhani, A., "Evaluation and performance comparison of power swing detection algorithms in presence of series compensation on transmission lines," Environment and Electrical Engineering (EEEIC), 2011 10th International Conference on , vol., no., pp.1,4, 8-11 May 2011.

[26] H. A. Mohammadpour, M. R. Pahlavani, A. Shoulaie, “On control of gate controlled series capacitor for SSR and power oscillation damping,” *Compatibility and Power Electronics, 2009. CPE’09. IEEE*, pp.196-203, May 2009.

[27] H. A. Mohammadpour, M. R. Pahlavani, A. Shoulaie, “On harmonic analysis of multi-module gate-controlled series capacitor (MGCSC) considering SSR phenomenon,” *International Review of Electrical Engineering*, vol.4, no.4, pp.627-634, Aug. 2009.

[28] M. Pahlavani, H. A. Mohammadpour, “Damping of sub-synchronous resonance and low-frequency power oscillation in a series-compensated transmission line using gate-controlled series capacitor,” *Electric Power Systems Research*, vol. 81, no. 2, pp. 308-317, Feb. 2011.

[29] H. A. Mohammadpour, Y. J. Shin, E. Santi, "SSR analysis of a DFIG-based wind farm interfaced with a gate-controlled series capacitor," *Applied Power Electronics Conference and Exposition (APEC), 2014 Twenty-Ninth Annual IEEE*, pp.3110-3117, March 2014.

[30] H.A. Mohammadpour, S.M.H. Mirhoseini, A. Shoulaie, "Comparative study of proportional and TS fuzzy controlled GCSC for SSR mitigation," *Power Engineering, Energy and Electrical Drives, 2009. POWERENG '09. International Conference on*, pp.564-569, March 2009.

[31] IEEE SSR Working Group, "Terms, definitions and symbols for subsynchronous oscillations," *IEEE Trans. Power Appl. Syst.* vol. PAS-104, no. 6, pp. 1326-1334, June 1985.

[32] H. A. Mohammadpour, E. Santi, "Modeling and control of gate - controlled series capacitor interfaced with a DFIG-based wind farm," *IEEE Transactions on Industrial Electronics*, DOI:10.1109 / TIE.2014.2347007, Available on-line: 12 August 2014.

[33] S. O. Faried, I. Unal, D. Rai, J. Mahseredjian, "Utilizing DFIG-based wind farms for damping subsynchronous resonance in nearby turbine-generators," *IEEE Trans. Power Systems*, vol.28, no.1, pp.452-459, Feb. 2013.

[34] K. R. Padiar, *Analysis of Sub-synchronous Resonance in Power Systems*. Kluwer Academic Publishers (KAP), Boston, 1999.

[35] H. A. Mohammadpour, Y. J. Shin, E. Santi,"SSR analysis of a DFIG-based wind farm interfaced with a gate-controlled series capacitor," *IEEE Twenty-Ninth Annual Applied Power Electronics Conference and Exposition (APEC) 2014*, pp. 3110 - 3117, 16 - 20 March, Fort Worth, TX, USA.

[36] H. A. Mohammadpour, Md. Islam, D. Coats Y. J. Shin, E. Santi, "Sub-synchronous resonance mitigation in wind farms using gate-controlled series capacitor," *Power Electronics for Distributed Generation Systems (PEDG), 2013 4th IEEE International Symposium on*, pp.1-6, July 2013.

[37] M. Sahni, D. Muthumuni, B. Badrzadeh, A. Gole, A. Kulkarni, "Advanced screening techniques for sub- synchronous interaction in wind farms," *Transmission and Distribution Conference and Exposition (T&D)*, pp.1-9, May 2012.

[38] H. A. Mohammadpour, E. Santi, "Sub-synchronous resonance analysis in DFIG-based wind farms: definitions and problem identification - Part I," *IEEE Energy Con-*

version Congress and Exposition (ECCE) 2014, pp. 1 - 8, 14 - 18 September, Pittsburgh, PA , USA.

[39] H. A. Mohammadpour, E. Santi, "Sub-synchronous resonance analysis in DFIG-based wind farms: mitigation methods - TCSC, GCSC, and DFIG controllers - Part II," *IEEE Energy Conversion Congress and Exposition (ECCE)*, pp. 1 - 8, 14 - 18 September, Pittsburgh, PA , USA.

[40] M Sahni, B Badrzadeh, D Muthumuni, Y.Cheng, H.Yin, S-H. Huang, Y. Zhou, "Sub-synchronous interaction in wind power plants- part II: an ERCOT case study," *Power and Energy Society General Meeting, 2012 IEEE*, pp.1-9, July 2012.

[41] Garth D. Irwin, Amit K. Jindal, Andrew L. Isaacs, "Sub-synchronous control interactions between type 3 wind turbines and series compensated AC transmission systems," *Power and Energy Society General Meeting, 2011 IEEE*, pp.1-6, July 2011

[42] Yunzhi Cheng, Mandhir Sahni, Dharshana Muthumuni, Babak Badrzadeh, "Reactance scan crossover-based approach for investigating SSCI concerns for DFIG-based wind turbines," *IEEE Transactions on Power Delivery*, vol. 28, no. 3, pp. 742-752, April 2013.

[43] Liang Wang, Xiaorong Xie, Qirong Jiang, H.R. Pota, "Mitigation of multi-modal sub-synchronous resonance via controlled injection of super-synchronous and sub-synchronous currents," *Power Systems, IEEE Transactions on* , vol.29, no.3, pp.1335,1344, May 2014.

[44] Tang Yi,Yu Rui-qian, "Impacts of large-scale wind power integration on subsynchronous resonance," *Power and Energy Engineering Conference (APPEEC), 2011 Asia-Pacific*, pp. 1-4, March 2011.

[45] R. K. Varma, Y. Semsedini, S. Auddy, "Mitigation of subsynchronous oscillations in a series compensated wind farm with Thyristor Controlled Series Capacitor (TCSC)," *Power Systems Conference: Advanced Metering, Protection, Control, Communication, and Distributed Resources, 2007*, pp.331,337, 13-16 March 2007.

[46] R. K. Varma, S. Auddy, Y. Semsedini, "Mitigation of Subsynchronous Resonance in a Series-Compensated Wind Farm Using FACTS Controllers," *Power Delivery, IEEE Transactions on* , vol.23, no.3, pp.1645,1654, July 2008.

[47] M. S. El Moursi, V. Khadkikar, "Novel control strategies for SSR mitigation and damping power system oscillations in a series compensated wind park," *IECON 2012 - 38th Annual Conference on IEEE Industrial Electronics Society*, 25-28 Oct. 2012.

[48] A. Moharana, R. K. Varma, R. Seethapathy, "SSR alleviation by STATCOM in induction-generator-based wind farm connected to series compensated line," *Sustainable Energy, IEEE Transactions on*, vol. 5, no.3, pp.947-957, July 2014.

[49] S. Golshannavaz, M. Mokhtari, D. Nazarpour, "SSR suppression via STATCOM in series compensated wind farm integrations," *Electrical Engineering (ICEE), 2011 19th Iranian Conference on*, May 2011.

[50] M. S. El-Moursi, B. Bak-Jensen, M. H. Abdel-Rahman, "Novel STATCOM controller for mitigating SSR and damping power system oscillations in a series compensated wind park," *Power Electronics, IEEE Transactions on* , vol.25, no.2, pp.429,441, Feb. 2010.

[51] A. Moharana, R. K. Varma, R. Seethapathy, "SSR mitigation in wind farm connected to series compensated transmission line using STATCOM," *Power Electronics and Machines in Wind Applications (PEMWA), 2012 IEEE*, 16-18 July 2012.

[52] A. F. Abdou, A. Abu-Siada, H. R. Pota, "Damping of subsynchronous oscillations and improve transient stability for wind farms," *Innovative Smart Grid Technologies Asia (ISGT), 2011 IEEE PES*, 13-16 Nov. 2011.

[53] R. K. Varma, S. Auddy, "Mitigation of subsynchronous oscillations in a series compensated wind farm with static var compensator," *Power Engineering Society General Meeting, 2006. IEEE*, 2006.

[54] V. P. Boopathi, R. Muzamil Ahamed, R. P. Kumudini Devi, R. Ramanujam, "Analysis and mitigation of subsynchronous oscillations in a radially-connected wind farm *Power and Energy Systems Conference: Towards Sustainable Energy, 2014*, March 2014.

[55] M. Anju, R. Rajasekaran, "Co-ordination of SMES with STATCOM for mitigating SSR and damping power system oscillations in a series compensated wind power system," *Computer Communication and Informatics (ICCCI), 2013 International Conference on*, Jan. 2013.

[56] U. Karaagac, S. O. O. Faried, J. Mahseredjian, A. Edris, "Coordinated control of wind energy conversion systems for mitigating subsynchronous interaction in DFIG-based wind farms," *IEEE Trans. Smart Grid.*, vol.5, no.5, pp.2440-2449, September 2014.

[57] A. E. Leon, J. A. Solsona,"Sub-synchronous interaction damping control for DFIG wind turbines," *IEEE Trans. Power Systems*, vol.pp, no.99, pp.1-10, June 2014.

[58] S. Golshannavaz, F. Aminifar, D. Nazarpour, "Application of UPFC to enhancing oscillatory response of series-compensated wind farm integrations," *IEEE Trans. Smart Grid.*, vol.5, no.4, pp.1961-1968, July 2014.

[59] A. E. Leon, J. M. Mauricio, J. A. Solsona, "Subsynchronous resonance mitigation using variable speed wind energy conversion systems," *IET Generation, Transmission & Distribution*, vol.7, no.5, pp.511-525, October 2012.

[60] L. F. W. D. Souza, E. H. Watanabe, J. E. R. Alves, and L. A. S.Pilotto, "Thyristor and gate controlled series capacitors: comparison of components rating," *IEEE Power Engineering Society General Meeting*, July 2003.

[61] M. R. Pahlavani, R. Ghandehari, A. Naghashpour, and H. A. Mohammadpour, " Power quality Enhancement Using Gate-Controlled Series Capacitor," *International Review on Modeling and Simulations*, vol. 3, no. 4, pp. 568-574, August 2010.

[62] http://www.abb.com/search.aspx?q=TCSC

[63] K. R. Padiyar, *FACTS Controllers in Power Transmission and Distribution.*, New Age International (P) Ltd., 2007.

[64] IEEE SSR Task Force, "First benchmark model for computer simulation of subsynchronous resonance," *IEEE Trans. Power App. Syst.*, vol. PAS-96, pp. 1562-1572, Sep./Oct. 1997.

[65] L. Fan, Z. Miao, "Mitigating SSR using DFIG-based wind generation," *IEEE Trans. Sustainable Energy*, vol. 3, no. 3, pp. 349-358, July 2012.

[66] M. Jafar, M. Molinas, T. Isobe, R. Shimada, "Transformer-less series reactive/harmonic compensation of line-commutated HVDC for offshore wind power integration," *Power Delivery, IEEE Transactions on*, vol.29, no.1, pp.353,361, Feb. 2014

[67] M. J. Hossain, T. K. Saha, N. Mithulananthan, H. R. Pota, "Control strategies for augmenting LVRT capability of DFIGs in interconnected power systems," *IEEE Trans. Industrial Electronics*, vol.60, no.6, pp.2510-2522, June 2013.

[68] P. Kundur, *Power System Sability and Control.*, New York: McGraw Hill, 1994.

[69] P. C. Krause, O. Wasynczuk, S. D. Sudhoff, *Analysis of Electric Machinery,*, IEEE Press, Piscataway, NJ, 1995.

[70] L. Wang, M. Sa-Nguyen Thi, “Stability analysis of four PMSG-based offshore wind farms fed to an SG-based power system through an LCC-HVDC link,” *IEEE Trans. Industrial Electronics*, vol.60, no.6, pp.2392-2400, June 2013.

[71] H. Akagi and H. Sato, “Control and performance of a doubly-fed induction machine intended for a flywheel energy storage system,” *IEEE Trans. Power Electron.*, vol. 17, no. 1, pp. 109âĂŞ116, Jan. 2002.

[72] R. Pena, J. C. Clare, G. M. Asher, “A doubly fed induction generator using back-to-back PWM converters supplying an isolated load from a variable speed wind turbine,” *IEE Proc. Electr. Power Appl.*, vol. 143, no. 5, pp. 380âĂŞ387, 1996.

[73] M. Rahimi and M. Parniani, “Efficient control scheme of wind turbines with doubly fed induction generators for low voltage ride-through capability enhancement,” *IET Renewable Power Gener.*, vol. 4, no. 3, pp. 242âĂŞ252, May 2010.

[74] P. Ledesma, J. Usaloa, “Effect of neglecting stator transients in doubly fed induction generators models,” *IEEE Trans. Energy Convers.*, vol. 19, no. 2, pp. 459âĂŞ461, June 2004.

[75] J. Arbi, M. J.-B. Ghorbal, I. Slama-Belkhodja, L. Charaabi, “Direct virtual torque control for doubly fed induction generator grid connection,” *IEEE Trans. Ind. Electron.*, vol. 56, no. 10, pp. 4163âĂŞ4173, Oct. 2009.

[76] E. Tremblay, S. Atayde, A. Chandra, “Comparative study of control strategies for the doubly fed induction generator in wind energy conversion systems: A DSP-based implementation approach,” *IEEE Trans. Sustain. Energy*, vol. 2, no. 3, pp. 288âĂŞ299, July 2011.

[77] G. Abad, M. A. Rodriguez, J. Poza, “Two-level VSC based predictive direct torque control of the doubly fed induction machine with reduced torque and flux ripples at low constant switching frequency,” *IEEE Trans. Power Electron.*, vol. 23, no. 3, pp. 1050âĂŞ1060, May 2008.

[78] G. Abad, M. A. Rodriguez, G. Iwanski, J. Poza, “Direct power control of doubly-fed-induction-generator-based wind turbines under unbalanced grid voltage,” *IEEE Trans. Power Electron.*, vol. 25, no. 2, pp. 442âĂŞ452, Feb. 2010.

[79] D. Santos-Martin, J. L. Rodriguez-Amenedo, S. Arnalte, “Direct power control applied to doubly fed induction generator under unbalanced grid voltage conditions,” *IEEE Trans. Power Electron.*, vol. 23, no. 5, pp. 2328âĂŞ2336, Sep. 2008.

[80] L. Xu, P. Cartwright, “Direct active and reactive power control of DFIG for wind energy generation,” *IEEE Trans. Energy Convers.*, vol. 21, no. 3, pp. 750âĂŞ758, Sep. 2006.

[81] M. Tazil, V. Kumar, R. C. Bansal, S. Kong, Z. Y. Dong, W. Freitas, “Three-phase doubly fed induction generators: An overview,” *IET Elect. Power Appl.*, vol. 4, no. 2, pp. 75âĂŞ89, Feb. 2010.

[82] R. Datta, V. T. Ranganathan, “Direct power control of grid-connected wound rotor induction machine without rotor position sensors,” *IEEE Trans. Power Electron.*, vol. 16, no. 3, pp. 390âĂŞ399, May 2001.

[83] S. Tohidi, H. Oraee, M. R. Zolghadri, S. Shao, and P. Tavner, “Analysis and enhancement of low-voltage ride-through capability of brushless doubly fed induction generator,” *IEEE Trans. Ind. Electron.*, vol. 60, no. 3, pp. 1146âĂŞ1155, Mar. 2013.

[84] F. Mei, B. C. Pal, “ Modeling of doubly-fed induction generator for power system stability study,” *in Proc. IEEE Power & Energy General Meeting 2008*, Pittsburgh, PA, Jul. 2008.

[85] F. Mei, B. C. Pal, “Modeling adequacy of the doubly fed induction generator for small-signal stability studies in power systems,” *IET Renewable Power Generation*, vol. 2, no. 3, pp. 181âĂŞ190, Sep. 2008.

[86] O. A. Lara, N. Jenkins, J. Ekanayake, P. Cartwright, M. Hughes, *Wind Energy Generation Modeling and Control*, England, John Wiley & Sons, 2009.

[87] Y. Lei, A. Mullane, G. Lightbody, R. Yacamini, “Modeling of the wind turbine with a doubly fed induction generator for grid integration studies,” *IEEE Trans. Energy Conversion*, vol. 21, no. 1, pp. 257-264, March 2006.

[88] H. Klee, R. Allen, *Simulation of Dynamic Systems with MATLAB and SIMULINK*, *Tylor & Francis Group.*, second edition, Boca Raton, FL, 2011.

[89] P. M. Anderson, B. L. Agrawal, J. E. Van Less, *Sub-synchronous Resonance in Power Systems.* IEEE Press, New York, 1990.

[90] Z. Lubonsy, *Wind Turbine Operation in Electric Power Systems.* Springer, New York, 2010.

[91] Ulf HÃd’ger, Christian Rehtanz, *Monitoring, Control and Protection of Interconnected Power Systems.* Springer, 2014.

[92] “competitive renewable energy zones (CREZ) transmission optimization study,” http://www.ercot.com/news/presentations/2008.

[93] “CREZ reactive power compensation study,” http://new.abb.com/products/power-consulting/reference-crez.

[94] K. Narendra, D. Fedirchuk, R. Midence, N. Zhang, A. Mulawarman, P. Mysore, V. Sood, “New microprocessor based relay to monitor and protect power systems against sub-harmonics,” *in Proc. IEEE Elect. Power and Energy Conf. (EPECâĂŹ11)*, 2011, pp. 438âĂŞ443.

[95] “Dakotas wind transmission study summary, Task 1 through Task 4” http://www.wapa.gov/ugp/PlanProject/.

[96] “Technical requirements for interconnection to the BPA transmission grid STD-N-000001” http://www.bpa.gov/transmission/Pages/default.aspx.

[97] “Southern Alberta Transmission Reinforcement,” http://www.aeso.ca/transmission/16869.html.

[98] J.M. Carrasco, L.G. Franquelo, J.T. Bialasiewicz, E. Galvan, R.C.P. Guisado, Ma.A.M. Prats, J. I. Leon, N. Moreno-Alfonso, “Power-electronic systems for the grid integration of renewable energy sources: a survey,” *IEEE Trans. Industrial Electronics*, vol.53, no.4, pp.11002-1016, June 2006.

[99] L. F. W. de Souza, E. H. Watanabe, M. Andres “GTO controlled ceries capacitors: multi-module and multi-pulse arrangements,” *Power Delivery, IEEE Transactions on*, vol.15, no.2, pp.725-731, April 2000.

[100] L. F. W. de Souza, “GTO controlled series capacitor,” *M.Sc. (in Portuguese)*, COPPE/UFRJ, Rio de Janeiro, Mar. 1998.

[101] K. Ogata, *Modern control engineering*, Prentice-Hall, Inc., Upper Saddle River, NJ, 2002.

[102] K. j. Astrom, B. Wittenmark, *Adaptive Control*, Second Edition, Dover Publications, INC, New York, 2008.

[103] J.-T. Su C.-W. Liu, “Gain scheduling control scheme for improved transient response of DC/DC converters,” *IET Power Electronics*, vol.5, no.6, pp.678-692, July 2012.

[104] J. Talaq, F. Al-Basri, “Adaptive fuzzy gain scheduling for load frequency control,” *Power Systems, IEEE Transactions on*, vol.14, no.1, pp.145âĂŞ150, Feb. 1999.

[105] Z. Qu, M. Hinkkanen, L. Harnefors, “Gain scheduling of a full-order observer for sensorless induction motor drives,” *Sensorless Control for Electrical Drives and Predictive Control of Electrical Drives and Power Electronics (SLED/PRECEDE), 2013 IEEE International Symposium on*, Oct. 2013.

APPENDIX A

THE UNDER STUDY POWER SYSTEM PARAMETERS

Table A.1: Parameters of the single 2 MW and 100 MW aggregated DFIG. Values are in $(p.u.)$, unless it is mentioned.

Base Power	2 MW	100 MW
Based voltage (V_{LL})	690 V	690 V
X_{ls}	0.09231	0.09231
X_{lr}	0.09955	0.09955
X_M	3.95279	3.95279
R_s	0.00488	0.00488
R_r	0.00549	0.00549
X_{tg}	0.3 (0.189 mH)	0.3 (0.189/50 mH)
DC-link base voltage	1200 V	1200 V
DC-link capacitor	14000 μF	50*14000 μF

Table A.2: Parameters of the network and shaft system. Values are in $(p.u.)$.

R_L	0.02	X_L	0.50	X_T	0.14	X_{sys}	0.06
H_t	4.29 s	H_g	0.9 s	D_{tg}	1.5	K_{tg}	0.15